Author:
[No Value], Melody Anne Drewry

Title:
Use of nonlinear ultrasonics for non-destructive evaluation of adhesive joints

USE OF NONLINEAR ULTRASONICS FOR NON-DESTRUCTIVE EVALUATION OF ADHESIVE JOINTS

by

Melody Anne Drewry

A dissertation submitted to the University of Bristol in accordance with the requirements for award of degree of Doctor of Engineering in the Department of Mechanical Engineering, Faculty of Engineering.

September 2012

Abstract

Ultrasonic testing remains the most common Non-Destructive Evaluation (NDE) technique for inspecting adhesive joints at the bond line as it can be targeted at small volume elements of interest. Whilst it can detect finite thickness disbonds, there is still no known NDE technique to detect kissing bonds (KB) and therefore assess the integrity of the bond. The literature describes the potential of nonlinear ultrasonic techniques, but previous work has failed to fully quantify nonlinearities generated by the experimental system. In this thesis, a new prediction tool that provides realistic simulations of nonlinear ultrasonic wave propagation is introduced to assess the detectability of KB in multi-layered structures. A series of experiments that quantify nonlinearities generated by the different sources are described, and a finite-element (FE) model in which the experimental data is incorporated is developed. This new prediction tool is expected to enable NDE engineers to know whether KB are at all detectable in a given adhesive joint, and if so, what experimental set-up, driving frequency and post-processing method to use in order to optimise KB detection capability.

Acknowledgements

I would like to start by expressing my gratitude to Dr George Georgiou for introducing me to Dr Robert Smith, to whom I will always be grateful for thinking of me for this EngD opportunity.

It is an honour to thank Professor Chris Scruby for believing in me.

I am heartily thankful to my supervisors, Dr Alan Fenwick for introducing me to chaos theory, Dr Albert Phang for his encouragement, and Dr Paul Wilcox, whose supervision and support from the preliminary to the concluding level enabled me to develop an understanding of the subject.

My thanks extend to all the members of the NDT groups at the University of Bristol, at Imperial College and at QinetiQ for their help, especially around the labs.

I would like to thank my family for pretending to understand my work, nodding and smiling at all times. In particular, I am indebted to my husband Thomas who gave me the moral support I required and my sons Percy and Arthur who give me so much joy every day.

Lastly, I would like to thank QinetiQ and the RCNDE for their funding without which this EngD would not have been possible.

Author's Declaration

I declare that the work in this dissertation was carried out in accordance with the requirements of the University's Regulations and Code of Practice for Research Degree Programmes and that it has not been submitted for any other academic award. Except where indicated by specific reference in the text, the work is the candidate's own work. Work done in collaboration with, or with the assistance of, others, is indicated as such. Any views expressed in the dissertation are those of the author.

SIGNED:  DATE: 25.09.2012

Table of Contents

List of Figures

List of Tables

Chapter 1

Introduction

In this chapter, the context in which this work was carried out and its motivations are explained. Background information on adhesive joints including their applications and modes of failure is given to better understand the need industry is facing. Finally, the objectives and outline of this thesis are presented.

1.1 General background

The work described in this thesis was carried out as part of an Engineering Doctorate (EngD) programme in Non-Destructive Evaluation (NDE) which takes place within the UK Research Centre in NDE (RCNDE). This programme is a collaboration between academia and industry to coordinate research into NDE technologies, and to ensure research topics are relevant to the medium to longer-term needs of industry. It was sponsored by the Engineering and Physical Sciences Research Council (EPSRC) and QinetiQ, the industrial partner.

QinetiQ, UK's largest research and technology organisation, has been working with aerospace customers as a fundamental part of their business for decades. Their aerostructures business offers support on the design aspects of aerospace structures by providing new tools for structural analysis that link with disciplines such as NDE. NDE activities range from fundamental studies of physical phenomena underlying the inspection process to the design and construction of prototype instrumentation and development of accompanying software.

As the adhesive bonding technique is increasingly being used in the aerospace industry — it provides weight and strength advantages while reducing manufacturing costs — there is a real need to identify the boundary imperfections that lead to adhesion failure.

1.2 Adhesive joints

Adhesive bonding is defined as the process of joining parts using a non-metallic substance (adhesive) which undergoes a physical or chemical hardening reaction causing the parts (adherends) to join together through surface adherence (adhesion) and internal strength (cohesion). The adhesively bonded assembly is known as an adhesive joint.

Although this assembly method is used for applications as diverse as medical and dental, building products, packaging, footwear and apparel, furniture, book binding, electrical and tape industries, its load-bearing applications are extensively found in the transport sectors, such as automotive, naval, rail and aerospace. In this work, the focus is on applications in automotive and aerospace industries.

In the automotive industry, adhesives are used for sealing and anti-acoustic or anti-vibration barriers but also for structural joints which influence the strength and stiffness of the car body and thus its safety and overall comfort.

In the aerospace industry, adhesive bonding is used mainly to attach stringers to fuselage and wing skins, stiffening the structures against buckling. It is also used to manufacture stiff lightweight structures of metal honeycomb cores inside metal skins for the flight control component structures (elevators, ailerons, spoilers, etc).

The desire to move to structural components being bonded makes the importance of adhesive bonds global. And with the increasing use of composites — in modern aircrafts for example, components are made of aluminium alloy, titanium, steel, polymer and polymer composites —, adhesive bonding has the major advantage of enabling different materials to be joined.

Another main advantage of adhesive bonding over other joining techniques is that the load is distributed more evenly at right angles to the loading direction and across a larger area as seen in Figure 1.1 providing higher fatigue strength. Other common joining techniques include welding where the two parts are heated to be joined, and mechanical fastening where the two parts are drilled then coupled with bolts or rivets.

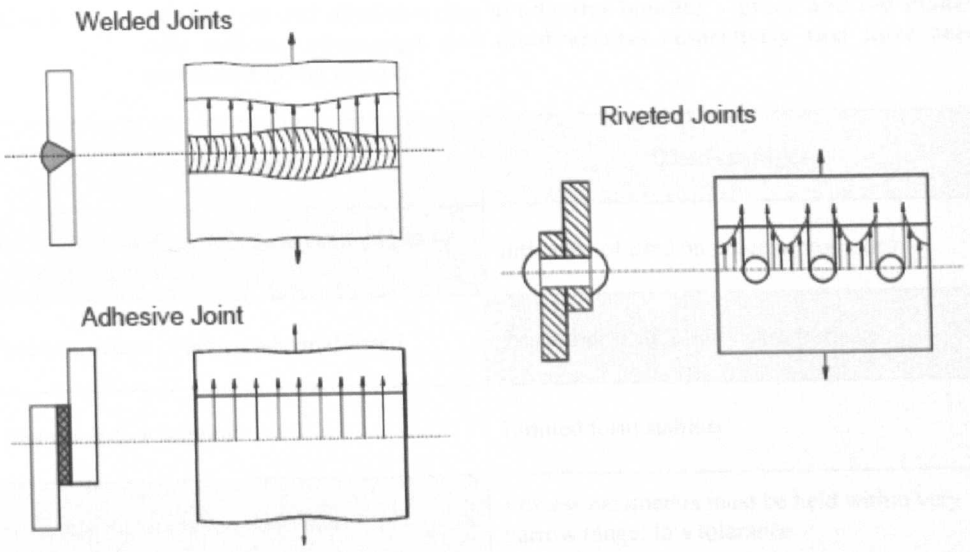

Figure 1.1. Load distribution at joints where the longer arrows indicate stress occurring along the bond line when the joint is subjected to normal stress for welded joints and shear stress for riveted and adhesive joints (short arrows) [1]

Another advantage of adhesive bonding is weight saving. When adhesive is used to affix stiffening stringers and doublers to wing and fuselage panels for example, the resulting panel is both stronger and lighter than a riveted structure. This joining method is therefore attractive to aerospace manufacturers, enabling them to produce lightweight, durable and strong bonds. Other advantages as well as disadvantages of adhesive bonding are listed in Table 1.1.

Table 1.1. Advantages and disadvantages of adhesive bonding – green and red shaded cells indicate advantages and disadvantages respectively that have been mentioned in the text [1]

Advantages	Disadvantages
Load distributed uniformly at right angles to loading direction	Influence of time on process properties
Microstructure of adherends unaffected	Pretreatment of joining parts surface
Distortion-free joining	Limited form stability
Different materials can be joined	Process parameters must be held within very narrow range: low tolerance
Very thin parts can be joined	Change of properties of joint with time (ageing of adhesive layer etc.)
Weight saving, light constructions	Complicated control of process
Heat-sensitive materials can be joined	Low peeling strength, creep sensitive
Metals with different electrochemical properties can be joined (insulating effect of adhesive)	Low adhesive layer strength must be compensated by large joining area
High strength in combination with riveting, spot-welding screw fastenings (eliminates crack corrosion)	Repair possibilities limited
High fatigue strength, good vibration damping	Complicated strength calculation

Adhesive joints are fabricated in many steps which involve surface pre-treatments, adhesive choice and curing processes. Incorrect procedures may lead to cohesion failure of the adhesive (poor cohesive strength, formation of voids), mixed adhesion and cohesion failure (chemical reaction between the adhesive and the adherend, environmental degradation of the adherend-adhesive interlayer such as porosity), or adhesion failure (disbond, poor adhesion).

When in the case of adhesion failure, an adhesive joint fails at the interface between the adhesive and the adherend as seen in Figure 1.2, it is usually the result of a poor surface treatment or due to the presence of a contaminant such as grease on an adherend during manufacture [2].

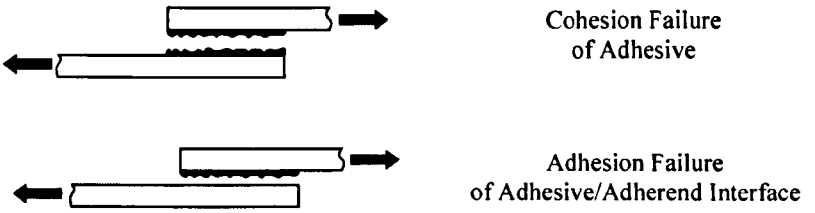

Figure 1.2. Failure mechanisms [2]

At that adherend-adhesive interface, there are two main classes of defect which occur as seen in Figure 1.3: complete disbonds (either finite thickness or zero-volume disbond) and poor adhesion (i.e. weak interface between the adhesive and one or both adherends).

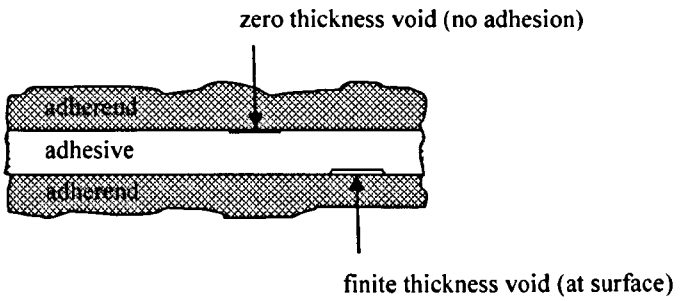

Figure 1.3. Types of disbonds at the adherend-adhesive interface

Deficient bonds which fail from adhesion failure contain what is called a zero-volume disbond (or kissing bond as defined by Nagy [3][4]) where the surfaces are in close proximity or even touching, but otherwise unbonded (no adhesive strength between the adherend and the adhesive). Because there is no separation at that interface, kissing bonds are extremely difficult to be detected by conventional NDE techniques.

It has been shown that such imperfect interfaces introduce a higher degree of nonlinearity as a result of contact acoustic nonlinearity (CAN) [5][6]. In other words, they have stiffnesses which vary with load and this makes them nonlinear in terms of their stress-strain behaviour. When an ultrasonic wave interacts with such a defect, it is distorted, and this distortion can be used to detect the presence of a kissing bond [6]-[10]. It should however be noted that these CAN cases refer to models and experiments that are not real in service use i.e. that kissing bonds were simulated, not real.

The use of nonlinear ultrasonic behaviour in NDE is an approach shown to be sensitive to very small defects such as distributed micro-cracking and small delaminations in composites [11]-[15], weakening of adhesive bonds [16]-[34], thermal and chemical damage [35], etc. There is existing literature on this nonlinear approach [14] as well as on the ultrasonic interaction with adhesively bonded interfaces [36]-[48]. However, very little has been done to determine the detectability of nonlinear effects due to such defects in a given structural specimen.

1.3 Problem statement

With advantages such as weight saving and higher fatigue strength, adhesive bonding is increasingly being used in the automotive and aerospace industries. There is therefore a real need to identify the boundary imperfections that lead to adhesion failure [49]. But while the detection of finite thickness disbonds generally presents few problems [50], there is currently no satisfactory NDE method for the detection of kissing bonds nor of weak interfaces between the adhesive and the adherend(s). As this remains one of the major challenges in NDE, the aim of this work is to address this gap. Also, as steel and aluminium are still widely used in the automotive and aerospace industry respectively, the focus here will be on metal-to-metal adhesive joints.

1.4 Objectives

The first objective of the work described here was to improve the understanding of kissing bond behaviour. The primary way of achieving this was by developing a generalised one-dimensional (1-D) finite-element (FE) type model to simulate nonlinear ultrasonic wave propagation in adhesive joints.

The second objective was to use the model to find the best experimental settings to detect nonlinear effects due to defects in a given structural specimen, if detectable at all.

1.5 Outline of the thesis

In Chapter 2, a literature review of the NDE techniques used for inspecting adhesive joints at the bond line is presented. These include radiography, nuclear magnetic resonance imaging (NMRI), thermography, holography, shearography, acoustic and ultrasonic methods. Ultrasonic methods are the most common methods used for adhesive joints. They can be divided into linear conventional, linear advanced and nonlinear ultrasonic methods for which other applications are also mentioned.

In Chapter 3, work carried out for Sandia National Laboratories involving the use of ultrasonic inspection techniques for contaminated lap-joint bond specimens is presented. The limitations of linear ultrasonic techniques including double through-transmission (DTT), pulse-echo (PE), ultrasonic spectroscopy, shear wave resonance and oblique incidence are given.

In Chapter 4, a theoretical outline of nonlinear ultrasonics is given. The stress-strain relationship is derived to obtain the nonlinear wave equation. From its solution, the most common nonlinear parameters are defined. A nonlinear ultrasonic technique is then carried out on the contaminated lap-joint bond specimens from Chapter 3.

As nonlinear wave propagation needs better understanding, a 1-D FE model is developed in Chapter 5 where the ultrasonic wave is visualised as oscillating masses connected by elastic springs.

In Chapter 6, the 1-D FE model developed in Chapter 5 is validated for linear wave propagation against an input impedance model and for nonlinear wave propagation by extracting the correct nonlinear parameter value for material inherent nonlinearity. Challenges and subtleties in modelling nonlinear wave propagation are described.

In Chapter 7, modelling rules are set by generalised equations with dimensionless factors. Recommendations on the choice of factors are given for optimised accuracy.

In Chapter 8, carefully controlled experiments are carried out to properly identify and quantify nonlinearities generated by external sources which are then incorporated into the model.

In Chapter 9, the model is used as a prediction tool and run on two different aluminium sandwich specimens. The analysis of the results gives the information needed to optimise experimental measurements. The FE model's performance is also assessed by comparing its output with experimental data.

In Chapter 10, a review of the thesis is given with a summary of findings. Possible areas for future research are also mentioned.

Chapter 2

Literature review

2.1 Introduction

In the previous chapter, the increasing use of adhesive bonding was explained and the current need of industry was identified: it is necessary to find Non-Destructive Evaluation (NDE) techniques for the detection of kissing bonds or of weak interfaces between the adhesive and the adherend. A literature review of NDE techniques for the inspection of adhesive joints at the bond line is therefore presented in this chapter.

2.2 NDE inspection for adhesive joints at the bond line

Unlike mechanical tests, bond strength cannot be directly measured with non-destructive techniques but a correlation between bond strength and some mechanical, physical or chemical parameter that can be measured without causing damage may be obtained [51][52]. Moreover, various types of flaws can be detected at the interface of an adhesive joint — the bond line. The focus here is on metal-to-metal adhesive joints as steel and aluminium are still widely used in the automotive and aerospace industry respectively. Techniques found successful on composites are however also mentioned if they could be applied to metals.

2.2.1 Radiographic methods

Radiographic methods can be divided into three groups following the radioactive source used: x-rays, gamma-rays (γ-rays) or n-rays (neutrons).

X-rays used in Film Radiography, Computed Radiography (CR) and Computed Tomography (CT) have found limited use in metal-to-metal bonded joints due to the large difference in density between metal and adhesive. For example, steel is

about seven times denser than epoxy which means that for a typical 70 kV photon energy, its linear absorption coefficient is twenty-two times higher. The difference in contrast levels between epoxy and air is therefore not visible on the x-radiograph. And even if the adhesive joint is manufactured using a radio-opaque adhesive in which a powder filler comprising a high atomic number metal is incorporated for the adhesive to be more radio-opaque than the surrounding metal, only volumetric defects such as voids in the adhesive can be detected by x-ray inspection as less dense material is traversed [53].

Due to their shorter wavelengths, gamma-rays are generally used to inspect specimens from 25 mm up to 230 mm thickness i.e. specimens that are much thicker than most adhesive joints in the automotive and aerospace industries. Moreover, at the lower thickness end of the range, the radiographs obtained with gamma-rays do not provide as good a resolution and contrast as those obtained with x-rays.

Attenuation of x-rays increases with increasing atomic number (density of electrons) which means that materials having a similar atomic number have a similar mass absorption coefficient. The attenuation of neutrons, on the other hand, is a function of the nucleus. A metal such as steel is more easily penetrated by neutrons than a hydrogen bearing adhesive. When neutron radiography is performed on metal-to-metal adhesive joints, the metal adherends are readily penetrated and the adhesive clearly imaged. Voids in the adhesive layer are visible and measurable on a high resolution transmission image where defective areas are indicated through a difference in image contrast with the adhesive appearing black and imperfections white. The major limitation of neutron radiography however is that it requires powerful neutron sources which are only available at research fission reactors or spallation neutron sources.

X-radiography is therefore the most suitable radiography method but can only detect missing adhesive.

2.2.2 Magnetic methods: nuclear magnetic resonance imaging

Nuclear magnetic resonance imaging (NMRI) has the capability to measure imperfections in adhesive joints. Voids and flaws can be detected during the

curing process, and the adhesive layer analysed [37]. However, only materials with water molecules can be imaged which means that a void will only show if infiltrated by a fluid.

2.2.3 Thermal methods: thermography

Thermography is a full-field, non-contact, very rapid non-destructive inspection technique. Two possible basic approaches are pulsed and modulated (lock-in) thermography [54]. More advanced techniques include thermosonics.

In pulsed thermography (PT), the specimen is exposed to a heat source (e.g. flash lamps) and the surface temperature is viewed with an infrared (IR) camera interfaced to a personal computer (PC) as the specimen cools. In areas above a subsurface defect, the transient flow of heat from the surface into the specimen is partially obstructed by the defect, thus causing a transient, local temperature increase at the surface. Here, disbonds at the interface would act as insulators and the heat would be trapped above these air gaps. The time-dependent response of the sample surface temperature to the thermal impulse is treated as a collection of independent pixel time histories.

In modulated thermography (MT), the thermal wave source (e.g. halogen lamps) is operated so as to obtain a sinusoidal temperature modulation. The system collects a series of IR images and compares their temperature levels computing the amplitude and phase angle of the sinusoidal wave pattern at each point.

Finite-thickness disbonds may be detected with PT or MT provided their depth does not exceed their lateral dimensions. The thermal wave imaging EchoTherm™ PT system is typically used on adhesive joints in the aerospace and automotive industries. Also, interfacial disbonds were detected clearly with high contrast using scanning thermography by adjustable mirrors, a promising automated NDE method for large-scale adhesive joints [55]. In the case of small material thickness, valuable information such as irregular distribution or lack of adhesive can also be obtained with MT [56]. Thermography is most commonly used for composites [57] as thermal diffusivity of metals may be as much as ten times that in the adhesive [58] making the contrast arising from a small defect spread over an area of thirty times the diameter that would be observed in a

homogeneous material, with correspondingly much reduced magnitude. For metals, vibrothermography or thermosonics using mechanical [59] and ultrasonic excitation respectively is therefore more suitable.

In thermosonics, an ultrasonic excitation horn is used to apply a short pulse of low frequency ultrasound at one point on the test structure. The sound wave causes the closely joined surfaces of defects to heat up by friction or clapping, thus making them visible to the thermal imaging camera. The method is particularly well suited to the detection of closed cracks and disbonds [60]. The assumption is that an imperfect interface such as a kissing bond might introduce frictional heating due to intermittent contact (clapping) or frictional forces.

While conventional thermography such as PT and MT can only detect finite-volume disbonds, an advanced method such as thermosonics has the potential of detecting zero-volume disbonds. However, in both cases, disbonds that can be imaged are mainly those near the surface in composite materials.

2.2.4 Optical methods: holography, shearography

In holography, the interference between the light reflected and scattered by the specimen and a reference beam is created and recorded. Holograms of the test specimen before and after it has been stressed are compared. The thermal or vibration stressing technique [61] is used to find disbonds in honeycomb panels made of composite facesheet and ultralight film adhesive [62]-[64] as well as those made of aluminium facesheet and thick film adhesive. For panels made of aluminum facesheet and light or ultralight film adhesive, the dual vacuum stressing technique would be used [65].

Shearography [66] using vacuum stressing or steady-state vibration is a useful technique for revealing disbonds in composite structures without the need of a reference beam like in holography.

2.2.5 Acoustic methods (1 to 30 kHz)

Acoustic methods [41] such as tap testing, the mechanical impedance technique and the membrane resonance method [67] involve the measurement of the

mechanical vibrations. The defect causes a local change in stiffness and a change in vibrational properties of the structure. These methods are used for the detection of delaminations in composite materials, disbonds in adhesive joints and defective honeycomb structures and laminates [68]. However, the sensitivity of all the methods is reduced as the defect depth is increased and some of them are unreliable close to the edges of a structure or on flexible structures.

2.2.6 Ultrasonic methods

Linear and nonlinear ultrasonic (UT) methods are described in the following two sections.

2.3 Linear ultrasonics for adhesive joints

Nine linear ultrasonic methods are discussed: three conventional (pulse-echo (PE), through-transmission (TT) and double through-transmission (DTT)) and six advanced (wideband ultrasonic spectroscopy, oblique incidence ultrasound, shear wave resonance [69], ultrasonic resonance impedance method, ultrasonic microscopy and surface acoustic waves).

2.3.1 Conventional ultrasonic methods

With conventional ultrasonic methods, compression waves at frequencies of 1-20 MHz are sent into the specimen usually by a piezoelectric transducer coupled to the specimen by coupling gel or in water immersion.

In PE mode, reflections from the weak bond are received by the same transducer whereas in TT mode, the signal is received at the other side of the specimen by another transducer. In both cases, the received signal amplitude and time of flight are measured. As in PE, the DTT method involves using the same transducer to transmit and receive the ultrasonic signal, but to measure the amplitude in a time gate that selects the reflection from a flat, uniform reflector placed just beyond the specimen, normal to the transducer beam. This determines the ultrasonic attenuation caused by passing twice through the specimen and can be plotted as a colour at each point in a two-dimensional raster scan to form a C-scan

presentation. Using these conventional ultrasonic techniques for testing the bond line, voids can be detected as long as the reflection coefficient is non-zero and consequently the transmission coefficient is less than one [70].

Pilarski [71] attempted to explain the existence of a relation between the reflection coefficient from the interface of an adhesive bond and its mechanical strength. It was however not possible to know what defects were present at the bond line.

2.3.2 Ultrasonic spectroscopy (UltraSpec™)

UltraSpec™ was developed at the Southern Research Institute (Birmingham, AL., USA) and uses a digitised 'chirp' signal to drive a standard dual element probe [72] in PE. The signal can cover a wide range of frequencies whilst maintaining a high signal-to-noise ratio (SNR) at each frequency compared with a broad-band pulse method. This results in a robust SNR in the frequency domain. Additionally, the input wave frequency range and amplitude can be user-defined. After amplification, the received signal is digitised and processed using the Fast Fourier Transform (FFT) to identify resonances and resonance spacing. UltraSpec™ is implemented with two Peripheral Component Interconnect (PCI) cards on a personal desktop computer (PC) and its software runs on a Microsoft Windows platform.

Application of this technique to bonded joints was reported by Smith et al. [69], wherein the difference between two frequency peaks – in both amplitude and frequency spacing – were observed to vary between a "good" bond and a "weak" one. The frequency difference between the two peaks, and their relative amplitudes, have been shown to be dependent on the thickness and ultrasonic properties of the adhesive layer [72]-[74]. Hence, if the adhesive layer has known uniform thickness across a joint, the ratio of the amplitudes of the two peaks can be used to detect and measure changes in ultrasonic properties across the joint, with the potential to assess the relative strength of the bond [36].

UltraSpec™ is limited by the bulky nature of a PC implementation and the requirement for alternating current (AC) power. Also, a known well-bonded area is required to enable the comparison of output frequency spectra. Finally, even if

UltraSpec™ measurements could be correlated with bond strength, it would not be possible to differentiate loss in cohesive strength from loss in adhesive strength.

2.3.3 Ultrasonic resonance impedance method

In this method, the piezoelectric transducer is operated at its resonance frequency and placed on the sample using couplant. The measured electrical impedance of the transducer is affected by the acoustic impedance of the sample which is altered by any lack of bonding.

Materials such as graphite or fiberglass, with low impedance, require lower frequency probes than metal-skin layers. Frequencies in the range of 35 to 500 kHz have been useful for most bond testing, with the higher frequencies used for thinner or metallic layers.

Bond testers such as the Fokker Bondtester are widely used in the aerospace industry for NDE of adhesive bonded laminates and honeycomb structures including those with external metallic sheets. The minimum size of voids detectable is closely related to operating frequencies and top sheet thickness. This method is particularly effective at detecting disbonds or delaminations in thin-skinned composites [75].

2.3.4 Shear wave resonance

Price and Martin pioneered this technique for the inspection of bonded joints between aluminium adherends [76]. A longitudinal focused beam directed normally to the plate surface contains non-normal incidence wave-fronts. At each reflection of non-normal incidence compression waves, shear waves are produced by mode conversion and resonate at frequencies which depend on their velocity. Based on the condition that in the metallic material the longitudinal wave velocity is approximately twice the shear wave velocity, the shear and longitudinal wave resonances coincide so that successive mode conversions combine constructively and produce a series of thickness-shear-wave resonance

with particle motions relatively parallel to the surface that enable the adhesive bond interface to be observed.

Figure 2.1 shows the response of a single 3 mm aluminium sheet (red) compared with that of an adhesive joint constructed from 3 mm aluminium adherends and 0.1 mm adhesive (blue), when using a 5 MHz transducer in pulse-echo mode.

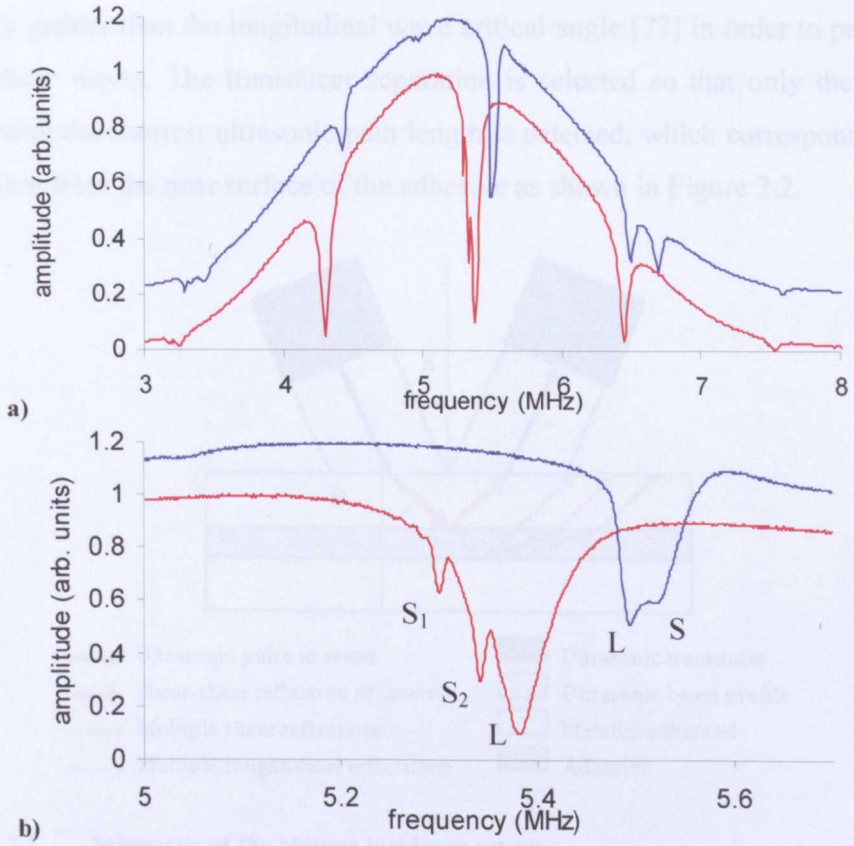

Figure 2.1. **a) Resonances observed using a 5 MHz transducer in pulse-echo on: the 'centre' of an adhesive joint constructed from 3 mm aluminium and 0.1 mm adhesive (blue/upper curves); and a 3 mm aluminium sheet (red/lower curves), over frequency range (top) 3-8 MHz and (bottom) 5-5.7 MHz. Each spectrum has an arbitrary offset to separate them - b) Zoom in, L = longitudinal resonance; S = shear resonance**

For the single aluminium sheet (in red on Figure 2.1), the shear and longitudinal resonances coincide close to 5 MHz. The presence of the adhesive causes a damping and a modulation of the shear wave resonance. The importance of the damping and shift in frequency is believed to be determinant for the characterisation of the adhesive bond modulus. Considered promising in metallic bonded structures, it is however not possible with this technique to know whether kissing bonds are present.

2.3.5 Oblique incidence

Oblique-incidence methods are more difficult to implement than the normal-incidence method, but they have the advantage that they can apply a shear stress component to the interface and hence are potentially more sensitive to interfacial properties. The angle of incidence of the ultrasound beam should be chosen to be slightly greater than the longitudinal wave critical angle [77] in order to produce only shear waves. The transducer separation is selected so that only the shear wave with the shortest ultrasonic path length is detected, which corresponds to a reflection from the near surface of the adhesive as shown in Figure 2.2.

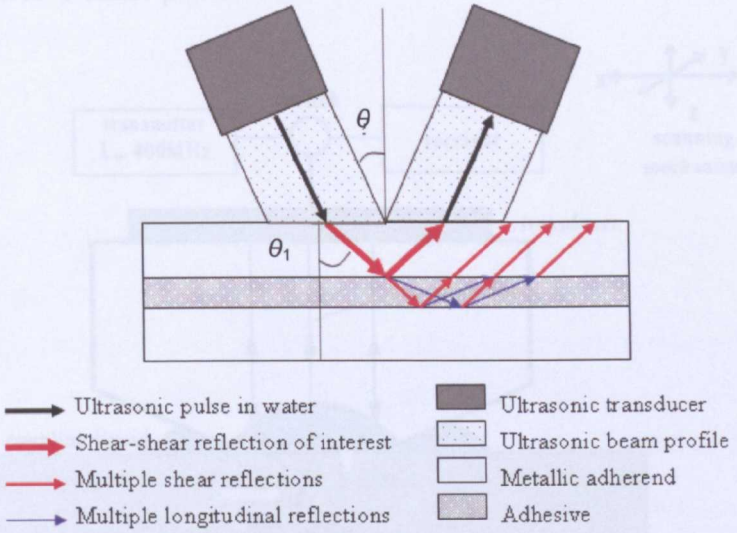

Figure 2.2. Schematic of the oblique incidence set-up

The oblique incidence immersion technique was used to determine the reflectivity characteristics of good versus weak bonds on various aluminium-epoxy-aluminium specimens [78]. Obliquely incident shear waves showed higher sensitivity to the weaker bonds than the conventional normally incident longitudinal waves as poor adhesion corresponded to a loss in shear stress at the interface. In effect, the oblique incidence technique is measuring changes in shear attenuation and shear interfacial stiffness, and therefore only works for sliding interfaces. As this is not necessarily always the case, this technique would require to be complemented by those using longitudinal waves in order to fully assess the integrity of the bond.

2.3.6 Ultrasonic (or acoustic) microscopy

Ultrasonic (or acoustic) microscopy is a high resolution technique for NDE. The basic idea of scanning acoustic microscopy (SAM) is to use a lens to focus the ultrasonic pulse on the sample [79]. A coupling fluid, which is usually water, is used to transmit the pulse to and from the sample as seen in Figure 2.3. The reflected echoes are collected by the lens and converted to an electronic signal. Any echo can be chosen for monitoring and, in this way, information from different depths can be obtained. A complete two-dimensional image called an acoustic micrograph is built up point-by-point by mechanically translating the sample in an X-Y raster pattern.

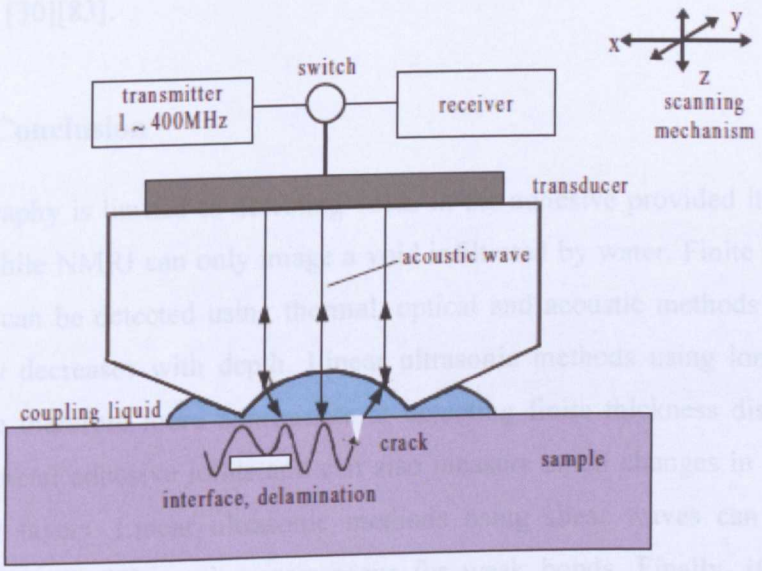

Figure 2.3. Working principle of SAM [80]

The different grey values on the micrograph correspond to the amplitude and time of flight of the reflected wave [80]. SAM has been used to detect flaws in epoxy bonded aluminium plates [79]. When areas of the bond give a strong reflection, they appear bright and correspond to disbonded regions. The acoustic microscope can therefore distinguish a perfect bond from full delaminations or disbonding as well as regions of interfacial degradation but only when it has resulted in a small void or delamination [81]. At a frequency of 45 MHz, defects could be determined through 6 mm of aluminium with a resolution of approximately 30 μm but would only include finite thickness disbonds. Moreover, the practical use of this technique is limited.

2.3.7 Interface waves (or Stoneley waves)

Surface Acoustic Waves (SAW) propagate along the surface of a material. At the boundary between two solid media, they are mode converted into interface waves (or Stoneley waves). Measurement of interface wave attenuation indicated that the technique is sensitive to changes in interfacial conditions. These results could therefore be extended to a more detailed study of interfacial phenomena in order to assess the applicability of this experimental method to bond strength determination [82]. Measuring the interface wave velocity to calculate the effective shear modulus is also a convenient quantitative characteristic for predicting the reduction in strength of a given specimen relative to a reference specimen [30][83].

2.3.8 Conclusion

X-radiography is limited to detecting voids in the adhesive provided it is radio-opaque while NMRI can only image a void infiltrated by water. Finite thickness disbonds can be detected using thermal, optical and acoustic methods but their sensitivity decreases with depth. Linear ultrasonic methods using longitudinal waves are therefore more appropriate at detecting finite thickness disbonds in metal-to-metal adhesive joints and can also measure small changes in very thin interfacial layers. Linear ultrasonic methods using shear waves can measure losses in shear stiffness that may occur for weak bonds. Finally, if there is frictional heating at the interface, thermosonics can detect delaminations in composites or in adhesive joints but only with very thin metal sheets. Kissing bonds remain therefore extremely elusive [84], which is the reason why other techniques based on nonlinear ultrasonics have been investigated.

2.4 Applications of nonlinear ultrasonics

Nonlinear ultrasonics has already been used for different applications reviewed here. It is first mentioned how it was used for material microstructure identification in physics and Earth studies to then be used in NDE as a tool for material characterisation (metal fatigue, thermal and chemical damage). The

technique is then reviewed for different types of damage (tight cracks, corrosion, distributed micro-cracking and small delaminations in composites, disbonds).

Nonlinear ultrasonics is mainly used for material characterisation in fields such as condensed matter physics [85]-[88], acousto-optics [89], low-temperature research [15], Earth studies [90], chemical physics [91], biophysics [92], biomedical engineering [93][94], acoustic microscopy [95][96] and NDE [97].

In NDE, a tool for material characterisation is of primary importance to detect changes often associated with fatigue damage that occur at a microscopic level when the structure is subject to loads (stretching, cyclic loads) or temperature variations. But often, when looking at the linear ultrasonic response, no noticeable change in attenuation or sound velocity with change of degradation can be found. The nonlinear response on the other hand seems to be more sensitive to the presence of damage than the linear response.

It should first be noted that materials have some degree of inherent nonlinearity that can be seen with the generation of harmonics in the frequency spectrum and measured by the nonlinear parameter that will be introduced later [98]. An efficient measurement procedure was developed by Shui [99] using Rayleigh surface waves in aluminium plates and by Price [100] using guided waves in rolled aluminium sheets. In heterogeneous media such as rock, soil, cement and concrete, nonlinear hysteretic effects were found in their elastic behaviour [101] and nonlinear ultrasonic wave propagation modelled [102]-[104]. Nonlinear ultrasonic measurements were in effect shown to be very sensitive to the presence of damage and to its characteristics (length, location and intensity) in hysteretic elastic materials [105]. When testing concrete in damaged and undamaged states, Shah [106] reported conclusive results which make nonlinear ultrasonics a promising technique for effective evaluation of in-situ concrete structures. Van den Abeele developed nonlinear elastic wave spectroscopy (NEWS) methods to detect damage in brittle materials such as brick, slate, concrete, rock, sand and soil [107][108].

These nonlinear hysteretic effects found in grained materials and rocks were also found in damaged elastic materials [109]. Hurley identified the sensitivity of the nonlinear ultrasonic parameter to microstructure variations and more precisely to

the presence of dislocations which in steel can vary with carbon content [110] but also with aging [111]. The plastic deformation occurring in damaged elastic materials is characterised by an increase in dislocation density [112]. Since dislocation dipole substructures formed during metal fatigue produce a substantial distortion of ultrasonic waves [85], nonlinear ultrasonics has been used to monitor degradation and fatigue in materials such as steel, aluminium and titanium alloys. A strong correlation between a nonlinear parameter and fatigue damage was also found when investigating aging degradation in high temperature materials used in turbine rotors in power plants [113] and in polycrystalline copper [114]. A similar correlation was found by Deng [115] using Lamb waves in aeronautic aluminium sheets, by Matikas [116] using surface waves in titanium alloy also used in aerospace structures, and by Straka [117] using nonlinear elastic wave modulation spectroscopy (NEWMS) on aluminium alloy. During fatigue, micro-cracks can also develop in metals and be detected with nonlinear ultrasonics [5] [118].

Some of these micro-cracks might even be contact type defects. Contact type defects include tight cracks or corrosion in homogeneous materials but also disbond type defects in multilayer structures (composites or with bonded elements). Interest in nonlinear ultrasonics was shown for such defects as partial contact at the interface can cause contact nonlinearity or clapping. The clapping of fatigue tight cracked faces for example has enabled Kawashima to classify the extent of the opening [119] while Sutin [120] used the nonlinear properties of the cracks to locate them. An acoustic vibro-modulation technique based on the nonlinear interaction of ultrasound and vibrations in the presence of contact-type defects was successful in detecting disbonds and cracks in composite materials, stress corrosion cracks, corrosion-induced delamination of structural elements, and fatigue cracks in materials such as aluminium, steel and titanium [121]. A similar technique sending two SAWs used as a measure of material nonlinearity the change in phase velocity of the high frequency wave (generated using a pulsed laser) compared to the stress experienced as it propagated [122]. A small increase in the mean nonlinear response was found in the fatigued sample compared with the unfatigued one but the scans showed spatial variation of nonlinearity and more experimental evidence is required to determine whether

this measure of nonlinearity is a viable metric for fatigue life. A low-frequency vibration modulation technique was also carried out using guided waves where linear defects were simulated by masses bonded onto an aluminium plate and nonlinear scatterers were simulated by loading a similar mass against the plate [123]. As this technique was able to discriminate between bonded and loaded masses, it could provide potentially additional defect characterisation information for structural health monitoring applications.

Another nonlinear ultrasonic technique, nonlinear wave modulation spectroscopy (NWMS), was successful at discerning an undamaged automobile engine component and one with a small crack [107]. This technique is one of the NEWS techniques ([11]-[13][35][98][107][108][120][124][125]) Van den Abeele has developed for damage detection that focus on the internal microstructural properties of materials. They also include nonlinear resonant ultrasonic spectroscopy (NRUS) [13], slow dynamics diagnostic (SDD) [124], time reversal acoustics (NL TRA) [98] and single-mode nonlinear resonance acoustic spectroscopy (SIMONRAS) [108].

Multilayer structures (composite or with bonded elements) may also have contact type defects such as micro-crack fields, cracks and delaminations in the case of composites. NEWS was used for quality assessment of composite laminates with such defects [11], for characterising microdamage in composite aeronautical components [12], detecting the presence of impact damage in foam sandwich panel aircraft structures [125], delamination damage due to low velocity impact on composite plates [13] and for finding damage initiation in composites used in aerospace structural parts as it enables good harmonic imaging of matrix cracks and micro-delamination [12]. By using a conventional C-scan system and extracting the second harmonic signals, Kawashima [26] developed a nonlinear ultrasonic imaging system to visualise fiber/matrix delaminations or matrix crackings in composite plates. Nonlinear harmonic generation was also found on other types of composites such as rubber-steel composites used in storage tanks and pipelines. The results obtained by Shkerdin [126] using Lamb waves can serve as a parametric guide for experimentalists considering their use as a tool for NDE of bilayers.

From a purely theoretical point of view, Gustafson [127] studied the ultrasonic transmission through a nonlinear layer in a linear medium. He found that the ultrasonic transmission coefficient derived for the second harmonic frequency exhibited greater sensitivity to changes in ultrasonic parameters (driving frequency, wave amplitude) and nonlinear layer parameters (acoustic velocity and impedance, thickness, elastic constants), than transmission at the fundamental frequency. This was back in 1977 and already suggested that nonlinear ultrasonics could be a promising technique for NDE of multilayer structures.

2.5 Nonlinear ultrasonics for adhesive joints

Structures with bonded elements such as adhesive joints have been found to be good candidates for nonlinear ultrasonics. In effect, nonlinear binding forces cause a nonlinear modulation of transmitted or reflected ultrasonic waves [21] and the generated higher harmonics of an incident monochromatic wave can give information about the quality of the adhesive bond. Hirsekorn [19] developed an ultrasonic measurement procedure that exploits the nonlinear transfer of ultrasound to distinguish between strong and weak bonds.

By postulating that failure of an adhesive bond is preceded by nonlinear behaviour in the thin boundary layer at the interface between adhesive and adherend, Achenbach and Parikh [22] carried out a theoretical investigation to obtain information on the adhesive bond strength from ultrasonic test results. Second order nonlinear measurements were found to be more sensitive to detect weak boundary layers than linear measurements [16][88]. Arnold [23] also looked at higher order harmonics and found a correlation between their amplitudes and the quality of the bond when using contaminant such as oil to simulate weak bonds.

Delsanto [21] investigated transmitted harmonic amplitudes for aluminium-epoxy-aluminium adhesive joints with water infiltrating from the edges. Comparison with data simulated by a simple model based on the local interaction simulation approach (LISA) was encouraging but not sufficient to warrant a practical application. Rokhlin [30] demonstrated that similar environmental

degradation of adhesive joints could be detected by a nonlinear frequency-modulated ultrasonic method.

The degradation due to cyclic fatigue of similar adhesive joints was detected by the reduction of the linear portion of the stress-strain curve of the bond. Based on the postulate that a deteriorated bond has nonlinear stress-strain behaviour, a theoretical explanation of these ultrasonic measurements was given by Tang [32].

ElectRelease™ is an electrically debonding epoxy adhesive developed by EIC Laboratories Inc. (Norwood, MA., USA). When a low power current is applied across the bond line between metallic adherends previously bonded with this high strength adhesive, a chemical reaction causes the bond to be released at the adherend-adhesive interface. When testing an adhesive joint made with ElectRelease™ adhesive which enables the production of kissing bonds, Weise [128] observed a small increase in harmonic amplitude in the disbonded state compared to the bonded state. A model written by Richardson [129] explains this level of nonlinearity due to intermittent opening and closing of the gap. The high strain at the contact tips of the kissing bond can in effect result in the generation of a second harmonic as studied by Barnard [130]. Solodov [131] also presented experimental results of acoustic nonlinear phenomena at contact boundaries. Biwa's [6] theoretical analysis for the nonlinear behaviour of elastic waves propagating through contact interface is commonly referred to. Yan [7][8] carried out similar experimental work on aluminium blocks [9]. His results look promising but other authors have published non-conclusive results that underline the challenges when carrying out such nonlinear measurements.

When Rothenfusser [132] studied material contributions to the second harmonic amplitude, he found that without the presence of a kissing bond, pure adhesion phenomena were hardly seen in an experiment. Bockenheimer [17] tested aluminium-epoxy-aluminium adhesive joints subjected to mechanical loading and hydrothermal ageing but did not find any changes in harmonic amplitudes for the weakened joints. When looking at a single layer with nonlinear interface, O'Neill [27] detected nonlinear distortion of the time-domain signal but a simple FFT of this data did not give such easily comprehensible results, with the harmonics sitting barely above noise level for both input and output signals. With

a model that predicts the evolution of interface damage by looking at the ultrasonic wave nonlinear distortion it introduces, O'Neill [28] also found that the acoustic power required to generate nonlinear effects was a significant fraction of the remaining strength of the material, and may result in the rapid failure of bonds with even a little damage. That is, there is only a narrow amplitude window where significant harmonics are produced without introducing significant new damage. This likely explains the difficulty the nonlinear ultrasonics community has had in making such a scheme operational — either the harmonic generation is small, or the measurement itself causes the part to fail.

2.6 Conclusion

In this chapter, a number of NDE techniques were reviewed and their potential for testing adhesive joints at the bond line was assessed (Table 2.1).

Table 2.1. Review of NDE techniques for testing adhesive joints at the bond line where green shaded cells indicate the techniques used for the experimental measurements in the next chapter

Technique	Defect type	Limitations and/or advantages for adhesive joints
x-radiography	voids in the adhesive	only when using radio-opaque adhesive
γ-radiography	voids in the adhesive	less resolution and contrast than x-ray for thin specimens
n-radiography	voids in the adhesive	high resolution but powerful neutron sources only available at research centres
nuclear magnetic resonance imaging (NMRI)	voids infiltrated by a fluid	can only image materials with water molecules
thermography	finite thickness disbonds	if the defect depth does not exceed its lateral dimensions, for composites mainly
vibrothermography	closed cracks	vertical cracks, friction restricted to certain places only, complex physical processes
thermosonics	fatigue cracks in metals, delaminations in composites	vertical cracks, friction restricted to certain places only, complex physical processes

holography	finite thickness disbonds	sub-surface defects, for composites mainly or aluminium facesheet
shearography	finite thickness disbonds	sub-surface defects, for composites mainly or aluminium facesheet, no need for a reference beam
tap testing	finite thickness disbonds	sensitivity decreases with depth, for composites mainly
mechanical impedance technique	finite thickness disbonds	sensitivity decreases with depth, for composites mainly
membrane resonance method	finite thickness disbonds	sensitivity decreases with depth, for composites mainly
linear conventional UT (PE, TT, DTT)	disbonds, changes in very thin interfacial layer	longitudinal waves, signal post-processing in time domain
UT spectroscopy	weak bonds	longitudinal waves, signal post-processing in frequency domain
UT resonance impedance method	disbonds, voids	composites mainly or external metallic sheets
shear wave resonance	bond strength	measurement of shear modulus
oblique incidence	weak bonds	measurement of shear attenuation and stiffness
UT microscopy	finite thickness disbonds	high spatial resolution
interface waves	bond strength	measurement of shear modulus

Most of the techniques listed in Table 2.1 are limited to the detection of voids in the adhesive layer or finite thickness disbonds and it was found that ultrasonic techniques remain the most appropriate NDE techniques for inspecting metal-to-metal adhesive joints at the bond line.

In the next chapter, results of linear ultrasonic measurements that were carried out on contaminated adhesive joints using different one-sided ultrasonic techniques are presented. Conventional ultrasonics and ultrasonic spectroscopy were chosen to have longitudinal waves sent into the specimens and the output signal processed in the time and frequency domains respectively. Oblique incidence and shear wave resonance were chosen to have shear waves looked at in the time and frequency domains respectively.

Chapter 3

Ultrasonic inspection of contaminated adhesive joints

3.1 Introduction

As mentioned in Chapter 1, the evolution of adhesives has enabled engineers to replace traditional fastened joints with bonded joints. Thus, although it is not always possible to confirm the presence of kissing bonds, the ability to quantify non-destructively the strength of bonded joints would find fabrication quality assurance and in-service inspection applications in automotive, aerospace, and civil industries. In the previous chapter, it was found that ultrasonic testing remains the most appropriate Non-Destructive Evaluation (NDE) technique for inspecting adhesive joints at the bond line.

During the Engineering Doctorate (EngD) programme, the opportunity arose to carry out tests on contaminated lap joint bond specimens. The purpose of this study was to determine, if applications of ultrasonic Non-Destructive Evaluation (NDE) techniques, coupled with signal analysis, were able to characterise compromised bonds, whether any measured ultrasonic parameters could be correlated with bond strength.

These ultrasonic parameters were measured using linear conventional techniques such as double through-transmission (DTT) and pulse-echo (PE), linear advanced techniques including ultrasonic spectroscopy, shear wave resonance and oblique incidence. These linear techniques enable longitudinal or shear waves to be analysed in the time or frequency domain.

3.2 Detail of measurements

3.2.1 Specimen history and dimensions

The Airworthiness Assurance Non-Destructive Inspection (NDI) Validation Centre (AANC) at Sandia National Laboratories (USA) provided two sets of specimens with similar adhesive bonds to those found in the automotive industry. The United States Council for Automotive Research (USCAR) has in effect been long-time partners with Sandia National Laboratories who have ongoing partnerships with key transportation industry groups. Each set comprised ten lap-joint bond specimens that had been prepared using specific methods proven to produce various levels of weak bonds. Both sets A and B are nominally the same. The bond area between the two galvanised steel adherends was 25.4 x 25.4 mm (1" x 1") as shown in Figure 3.1. The thickness of the steel plate was 1.5 mm (0.060") and the thickness of the bond line was 0.40 mm (0.016").

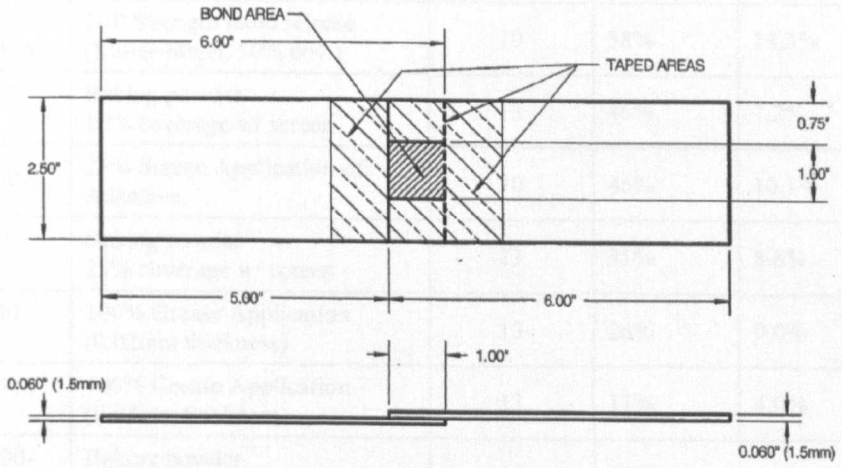

Figure 3.1. Drawing of steel lap-joint bond specimen

Inspections were performed from side 1 hence had the weak bond surface on the near side as seen in Figure 3.2.

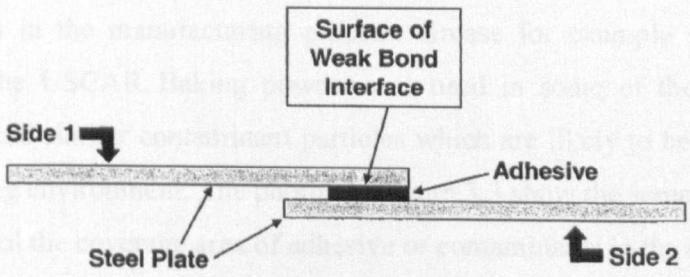

Figure 3.2. Schematic showing position of weak bond surface relative to inspection sides 1 and 2

Full-strength specimens (pristine) were used as an inspection baseline. The compromised specimens were manufactured either with specific contaminants, or reduced bond areas, to produce weaker bonds. The contaminant types and associated bond strengths - as determined by multiple strength tests on similar specimens - are listed in Table 3.1 and illustrated in Figure 3.3 and Figure 3.4.

Table 3.1. Summary of test specimens – Methods to produce weak bonds and the estimated bond strength for each type of specimen

USCAR Weak Bond Coupon Specimen Test Matrix				
Specimen No.	**Description**	**No. of Strength Tests Completed**	**% of Bond Strength**	**Standard Deviation**
T-PRI-7F-X	Pristine	10	100%	2.8%
T-MO-RE-MS-25-zzF-X	Full Strength mold release (Miller-Steph. 25% cov.)	10	88%	3.9%
T-GRE-100-01-zzF-X	100% Grease Application (0.01mm thickness)	13	62%	11.2%
T-MO-RE-MS-50-zzF-X	Full Strength mold release (Miller-Steph. 50% cov.)	10	58%	14.3%
T-PWD-10-zzF-X	Baking powder 10% coverage w/ screen	13	46%	7.2%
T-SC-25-7F-X	25% Screen Application of Adhesive	10	46%	10.1%
T-PWD-25-zzF-X	Baking powder 25% coverage w/ screen	13	31%	8.6%
T-GRE-100-02-zzF-X	100% Grease Application (0.02mm thickness)	13	26%	9.0%
T-GRE-100-05-zzF-X	100% Grease Application (0.05mm thickness)	13	11%	4.0%
T-PWD-100-zzF-X	Baking powder 100% coverage	11	10%	4.0%

"zz" = unique specimen number for that particular configuration
"X" = represents the particular specimen Set which will be either A or B

The contaminants were chosen to represent the types of bond weakening that may be seen in the manufacturing process. Grease for example is a primary concern to the USCAR. Baking powder was used in some of the samples to mimic dust and similar contaminant particles which are likely to be present in a manufacturing environment. The photos in Figure 3.3 show the screening process used to control the coverage area of adhesive or contaminants in the specimens.

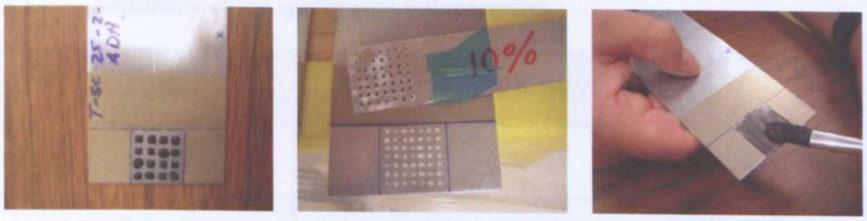

25% Adhesive | 10% Powder Coverage | Grease Application

Figure 3.3. Coverage of contaminants

The relationships between bond strength and the amount of adhesive or contaminants are shown in Figure 3.4.

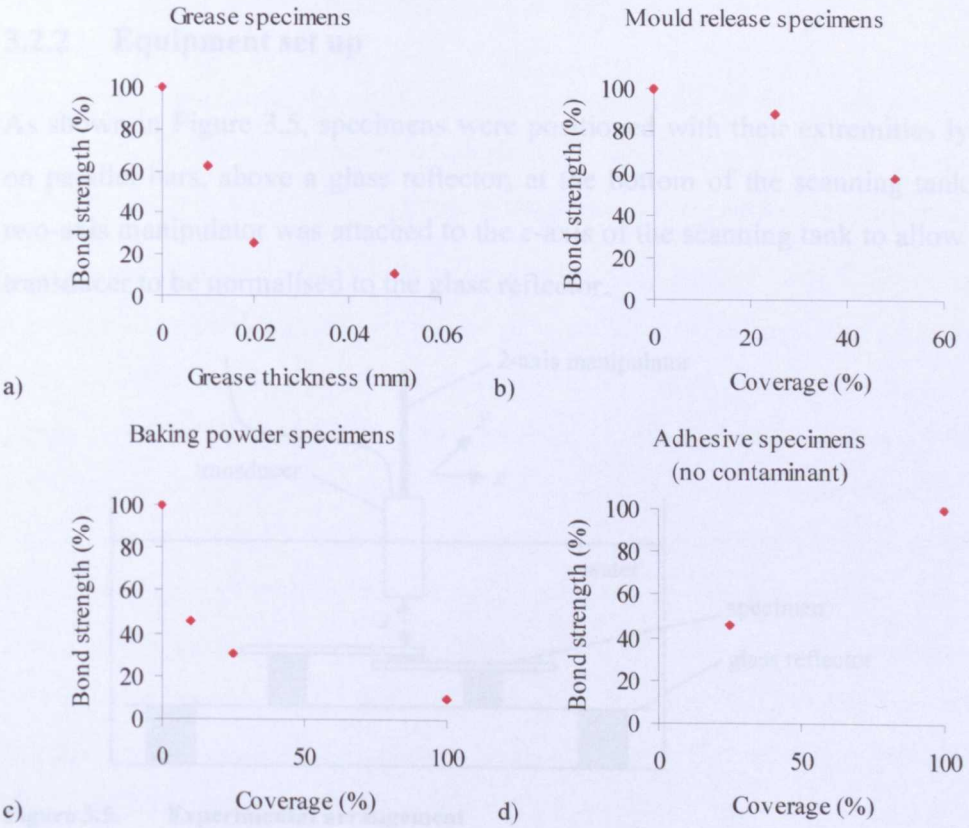

Figure 3.4. Amount of contaminant or adhesive in relation to bond strength

Sandia National Laboratories had provided information about the reaction of some contaminants with the adhesive and the failure mechanisms for each type of contaminant as summarised in Table 3.2. All types of specimens failed at the bond line described as the weak bond interface in Figure 3.2. The grease and mould release specimens had primarily adhesive failure. The screen-application adhesive specimens showed cohesive failure and the baking powder specimens a mix of adhesive and cohesive failure.

Table 3.2. Summary of the specimens' failure modes

Type of specimen	Failure mode
Mould release	adhesive
Grease	adhesive
Baking powder	adhesive / cohesive
Screen application of adhesive	cohesive

3.2.2 Equipment set up

As shown in Figure 3.5, specimens were positioned with their extremities lying on parallel bars, above a glass reflector, at the bottom of the scanning tank. A two-axis manipulator was attached to the *z*-axis of the scanning tank to allow the transducer to be normalised to the glass reflector.

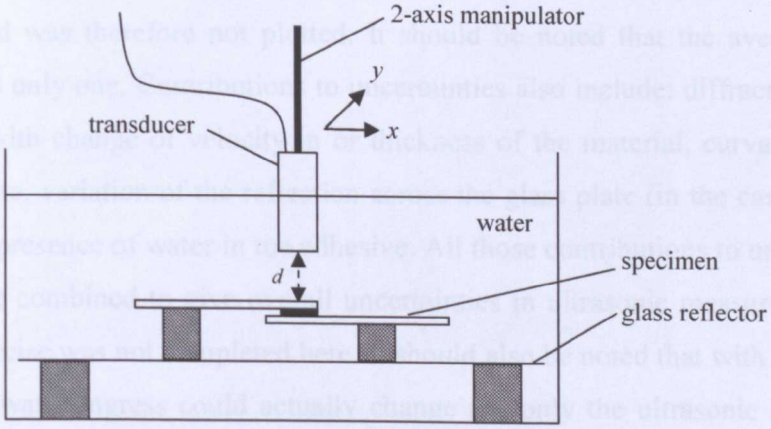

Figure 3.5. Experimental arrangement

The equipment used for the scans are listed in Table 3.3 and Table 3.4.

Table 3.3. Probes used for ultrasonic measurements

Frequency (MHz)	Probe: Serial number	Diameter	Focus	Measurement type
10	Alpha C01401	0.375"	3"	DTT and PE
10	Alpha C08422	0.5"	1.5"	Shear wave resonance
25	Alpha 524778, Alpha 00J0K9	0.25"	planar	Oblique incidence
1	Pz26, 2mm thick	16 mm		Nonlinear measurements
5	Panametrics	0.25"		

Table 3.4. Electronic equipment and associated power settings

Equipment Item	Description	Serial number	Damping Ω	Power pF	Measurement type
Krautkramer Branson USD 15	Pulser-receiver	34229-1607	50	1000	DTT
		33888-857	33	220	PE
KFJ HIS1902 & 1908	Pulser-receiver	8708071 9410985	1		Oblique incidence
Handyscope-HS3	Pulser-receiver				Nonlinear measurements

3.3 Linear ultrasonics: conventional methods

The average amplitudes of the A-scan waveforms acquired from each technique were plotted against estimated bond strength featuring x error bars using the associated standard deviation in bond strength measurements listed in Table 3.1.

Concerning the signal amplitudes collected with DTT and PE over the bond area, the calculated standard error on the mean was found to be negligible (0.1 dB or less) and was therefore not plotted. It should be noted that the average of an image is only one. Contributions to uncertainties also include: diffraction effects linked with change of velocity in or thickness of the material, curvature of the steel plate, variation of the reflection across the glass plate (in the case of DTT) and the presence of water in the adhesive. All those contributions to uncertainties could be combined to give overall uncertainties in ultrasonic measurements but this exercise was not completed here. It should also be noted that with immersion testing, water ingress could actually change not only the ultrasonic parameters measured but also the bond strength.

3.3.1 Double through-transmission scans

DTT scans were performed in order to determine the performance of conventional ultrasonic methods, which if they are adequate and sufficient, would remove the need to develop more advanced methods. Two scans, one with high gain and the other with low gain, were performed on each of the specimens, which were supported 25 mm above a glass reflector plate immersed in the scanning tank. Initially the transducer was normalised to the glass reflector plate

and positioned at the focal distance from the glass plate by maximising the front wall echo. The 10 MHz transducer was scanned over the bond areas of the specimens at 0.5 mm steps. The transducers and electronic equipment used are as listed in Table 3.3 and Table 3.4.

The results of those DTT scans are C-scans which were generated from the A-scan amplitudes, representing the amount of ultrasound reflected from the glass plate that comes back to the transducer. Full waveform data was not captured.

A selection of two scan results, comprising a pristine and a contaminated sample, is shown in Figure 3.6. They show the amplitude of the ultrasonic signal reflected from the glass reflector plate that lies 25 mm under the specimens.

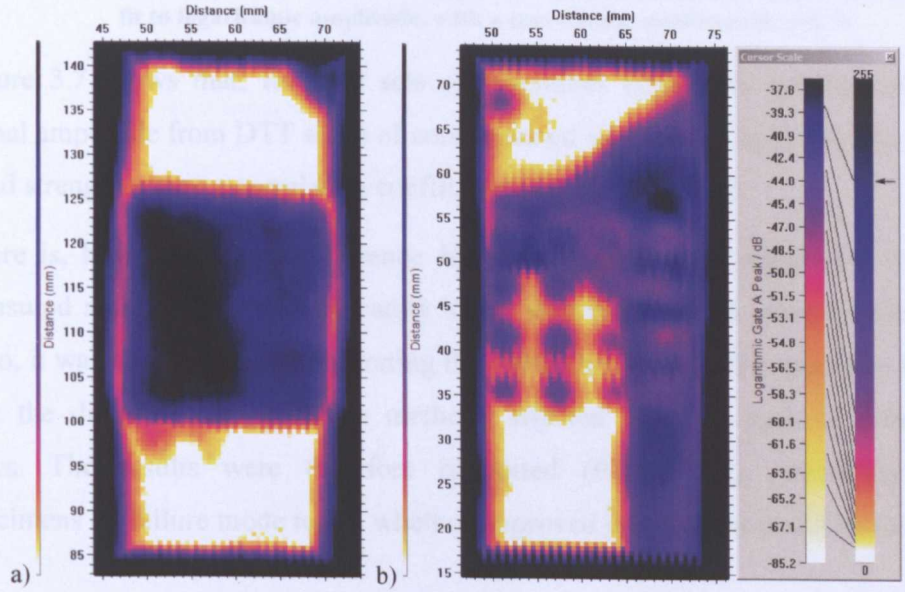

Figure 3.6. Example of DTT C-scans of lap joint bond specimens from Set A – a) pristine specimen (100% bond strength) and b) 25% screen-application adhesive (46% bond strength).

Darker areas represent higher amplitude signals hence good bond adhesion. Degradation of the adhesive joint is therefore visible as lighter (yellow-white) colours in the scan. The amplitudes measured over the bond area were averaged and plotted in Figure 3.7. The figure also includes a linear trend-line for comparison using a correlation coefficient. Both datasets A and B were combined to double the number of data points, thus improving both the fit and the correlation coefficient.

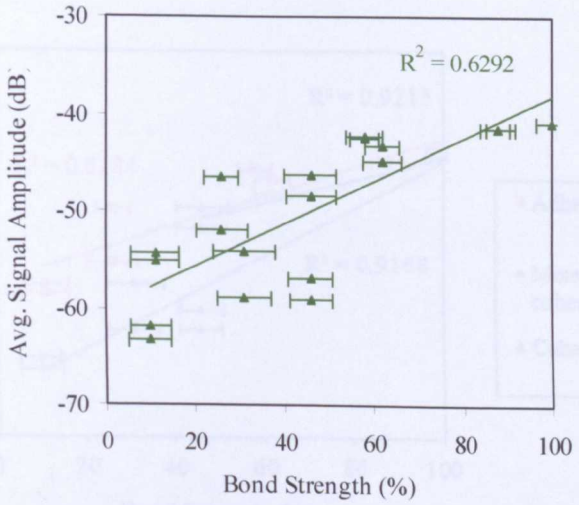

Figure 3.7. Summary of 10 MHz DTT amplitude measurements and linear line of best fit to logarithmic amplitude, with a correlation coefficient R of 0.79

Figure 3.7 shows that, for both sets of specimens combined, the logarithmic signal amplitude from DTT scans of contaminated specimens varies linearly with bond strength where a correlation coefficient of 0.79 was found.

There is, however, a step difference for the baking-powder specimens whose measured amplitudes are significantly lower than those of the other specimens. Also, it was noted, when incorporating the failure modes for each specimen type, that the different contamination methods affected bond strength in different ways. The results were therefore re-plotted (Figure 3.8), separating the specimens by failure mode to see whether improved correlations could be found.

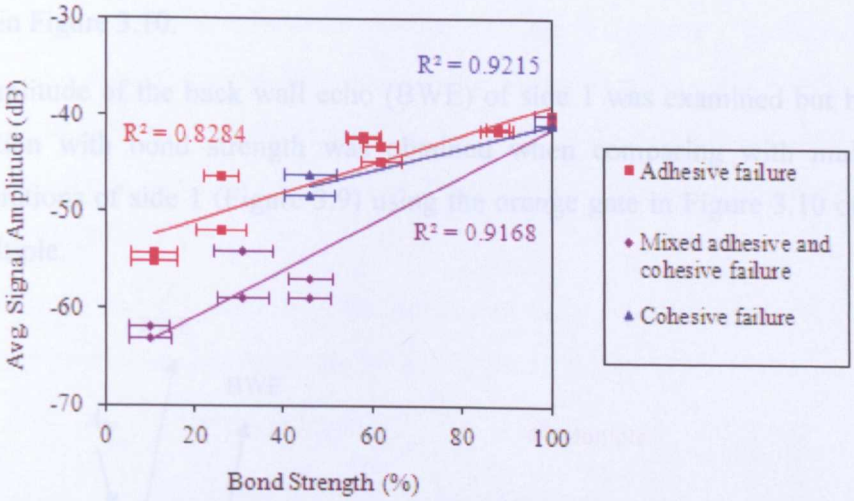

Figure 3.8. **Summary of 10 MHz DTT amplitude measurements and linear line of best fit to logarithmic amplitude for specimens divided by failure modes with a correlation coefficient R of 0.91 for adhesive failure, of 0.96 for mixed adhesive and cohesive failure, and of 0.97 for cohesive failure**

From the higher correlation coefficients found in Figure 3.8, it is confirmed that the averaged logarithmic signal amplitudes have a stronger linear trend with respect to bond strength when separated into failure modes. It should however be noted that the specimens with adhesive failure where kissing bonds might be present have the lowest correlation coefficient.

In terms of predicting bond strength from measurements of DTT amplitude, it is essential that the contaminant type and thence the failure mode are determined first, so that the correct prediction can be made. Other ultrasonic methods are therefore necessary for differentiating between different types of contaminated weak bonds.

3.3.2 Pulse-echo scans

Further scans on the samples were performed using the full-waveform capture PE technique and measurements of the signal amplitude were made. A 10 MHz transducer with 3-inch focal length in water (Table 3.3) was used. The drive electronics are listed in Table 3.4. All scans were performed with a 0.5 mm scan pitch. As before, the scans were acquired with the contaminated bond surface on the near side (side 1). Therefore the two first signals obtained on the A-scans were the front-wall echo (FWE) from the top plate and the reflection from the

interface with the contaminant side of the adhesive (weak bond interface) as shown in Figure 3.10.

The amplitude of the back wall echo (BWE) of side 1 was examined but better correlation with bond strength was obtained when comparing with multiple reverberations of side 1 (Figure 3.9) using the orange gate in Figure 3.10 on the 4th multiple.

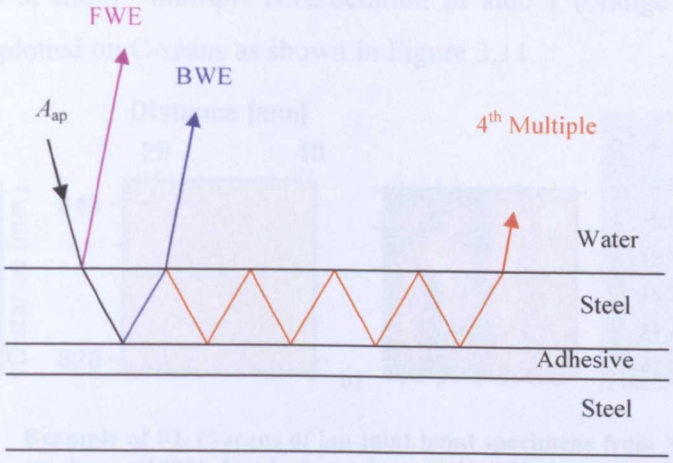

Figure 3.9. Sketch of the signal reflected from the top adherend layer

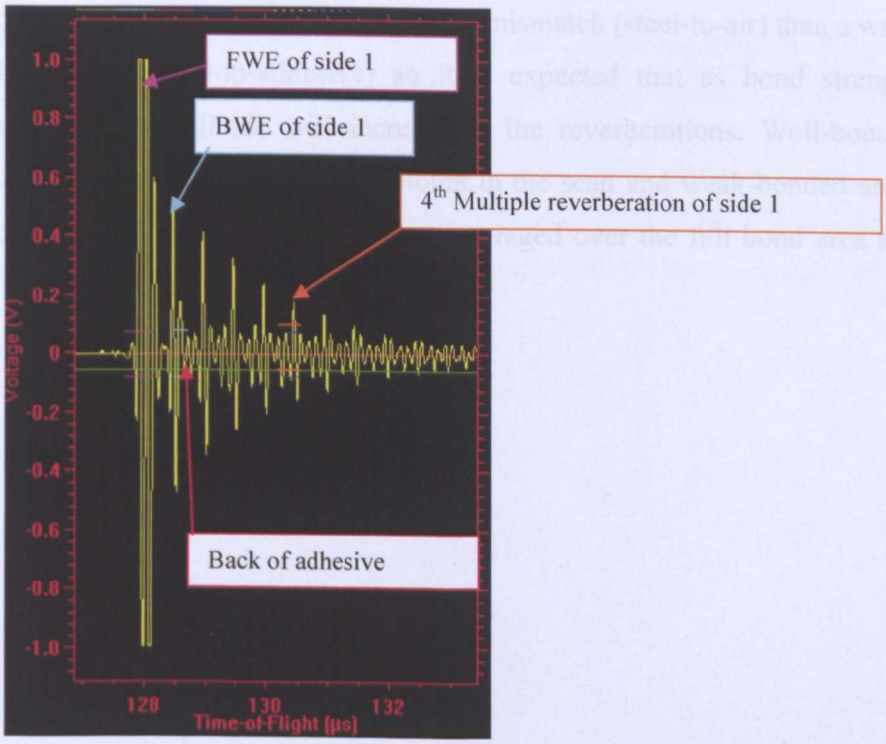

Figure 3.10. Example time-domain signal for PE at 10 MHz. Note that the front-wall echo has saturated the digitiser at +/- 1 V.

In effect, a reverberation multiple increases the sensitivity and the 4th multiple enhances any interfacial effects by raising it to the 5th power. The higher the multiple, the higher the power however the signal-to-noise ratio (SNR) will reduce, along with the introduction of interferences from multiple reverberations in the adhesive. Collectively these raise the challenge to quantitatively measure the signal amplitudes.

Amplitudes of the 4th multiple reverberation of side 1 (orange gate in Figure 3.10) were plotted on C-scans as shown in Figure 3.11.

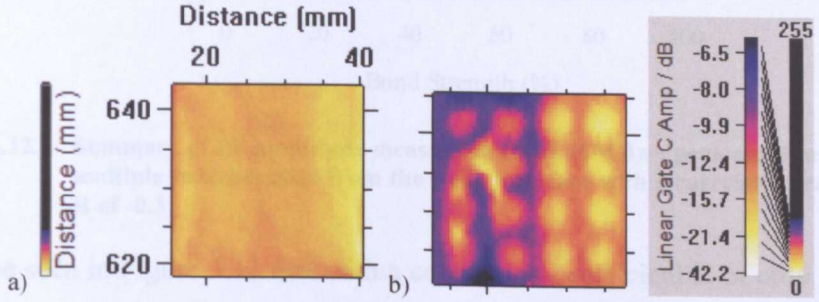

Figure 3.11. Example of PE C-scans of lap joint bond specimens from Set A – a) pristine specimen (100% bond strength) and b) 25% screen-application adhesive (46% bond strength)

A disbonded interface has a larger impedance mismatch (steel-to-air) than a well-bonded interface (steel-to-adhesive) so it is expected that as bond strength decreases, signal amplitude will increase in the reverberations. Well-bonded areas are therefore visible as lighter colours in the scan and weak-bonded areas as darker colours. These amplitudes were averaged over the full bond area and plotted in Figure 3.12.

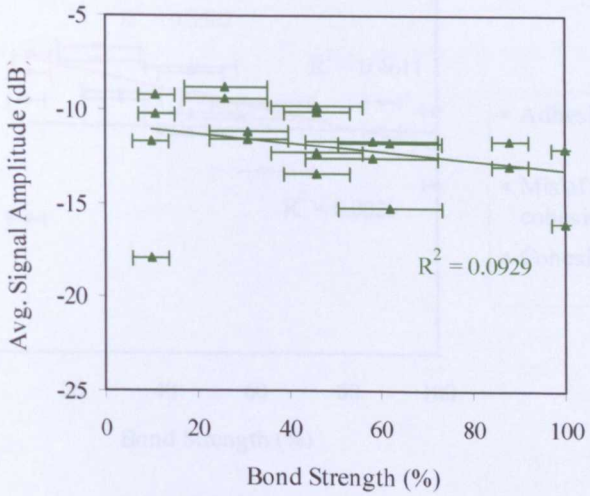

Figure 3.12. Summary of PE amplitude measurements at 10MHz – peak amplitude of 4th multiple reverberation from the weak interface with a correlation coefficient R of -0.3

It can be seen in Figure 3.12 that with a correlation coefficient R of only -0.3, no statistically significant linear correlation can be found between the logarithmic PE amplitude of the 4th multiple reverberation and the bond strength. The correlation coefficient R is negative because as the bond line gets weaker, the amplitude of the 4th reverberation increases. Note that the trend is inversed compared with DTT measurements where the amplitudes measured refer to the amount of ultrasound passing through the specimen.

The specimens have once again been categorised according to their failure mode when analysing the results in Figure 3.13 to see whether improved correlations could be found.

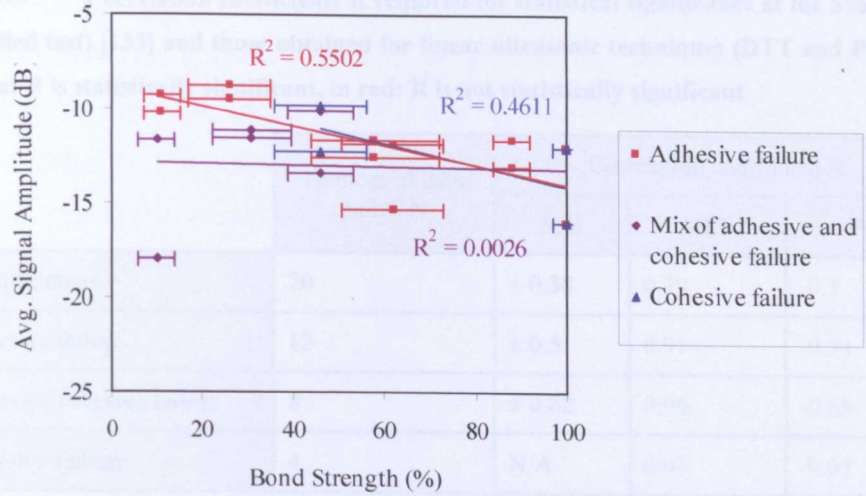

Figure 3.13. Summary of PE normalised 4th multiple reverberation amplitude measurements at 10 MHz with the specimens separated into type of failure

As seen in Figure 3.13, this categorisation is useful for adhesive or cohesive failure specimens with improved correlation coefficients of -0.74 and -0.68 respectively but there is no significant correlation for baking powder specimens that correspond to a mix of adhesive and cohesive failure. PE measurements are therefore sensitive to the type of contaminant used and give less significant, if any, correlations between signal amplitude and bond strength compared with DTT measurements.

3.3.3 Summary

Correlation coefficients R obtained with both conventional techniques (DTT and PE) are summarised in Table 3.5.

Table 3.5. Correlation coefficients R required for statistical significance at the 5% level (one-tailed test) [133] and those obtained for linear ultrasonic techniques (DTT and PE) — in green: R is statistically significant, in red: R is not statistically significant

	Number of data points N	Correlation coefficient R		
		Min	DTT	PE
All specimens	20	± 0.38	0.79	-0.3
Adhesive failure	12	± 0.5	0.91	-0.74
Adhesive/cohesive failure	8	± 0.62	0.96	-0.68
Cohesive failure	4	N/A	0.97	-0.05

As seen in Table 3.5, all correlation coefficients obtained with DTT are statistically significant. However, PE measurements with ultrasonic compression waves analysed in the time domain were not suitable for assessing bond strength if the type of contamination used for the specimens was unknown. It was therefore necessary to investigate other ultrasonic methods for differentiating between different types of contaminated weak bonds. More advanced ultrasonic methods such as shear waves or frequency-domain data processing will be considered in the next section.

3.4 Linear ultrasonics: advanced methods

3.4.1 Ultrasonic spectroscopy (UltraSpec™)

A 5 MHz dual-crystal (pitch-catch) plane wave transducer with a 5 MHz bandwidth was used for single-sided contact point measurements. One measurement was taken for each specimen over the bonded area, from which the frequency spectrum was calculated by UltraSpec™. Spectra obtained for Set A specimens are plotted in Figure 3.14a. Also shown in Figure 3.14b is the modelled transmission response of a lap-joint with two 1.5 mm steel adherends and a 0.4 mm adhesive layer containing various volume-fractions of porosity. The model is a simple normal-incidence compression-wave analytical model for multiple isotropic layers and is described in Appendix A. The model calculates the complex transmission and reflection coefficients for each successive layer of

material. This yields the impulse response of the entire layered structure which is then convolved with a transducer pulse to produce the final simulated ultrasonic response. To simulate different bond strengths, porosity was added to the adhesive layer using an equivalent-medium mixture rule for spherical inclusions based on the work of Hashin [138].

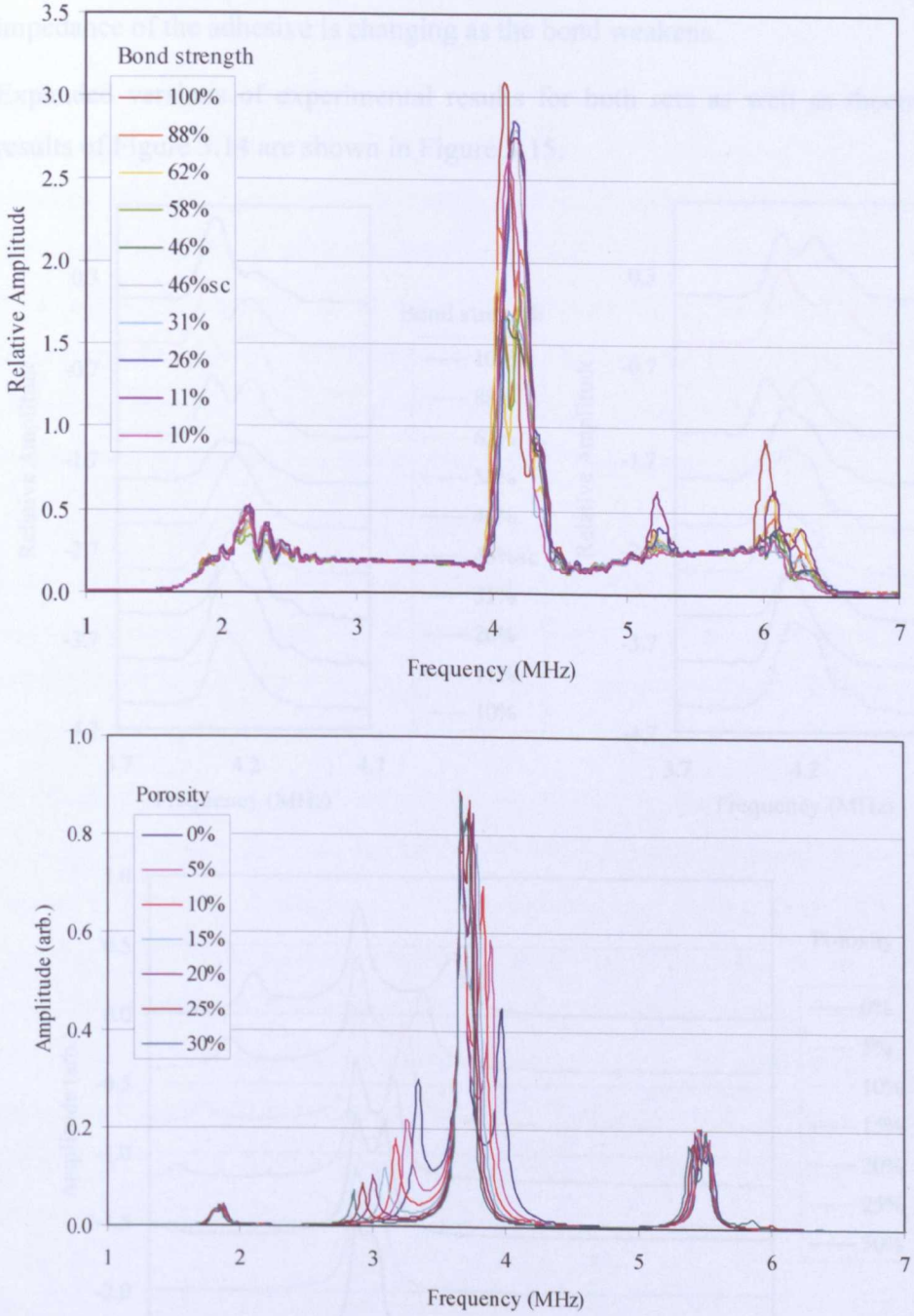

Figure 3.14. UltraSpec™ frequency spectra of the output signal for each steel bonded specimen of Set A (top), and the modelled response of such a structure, representing bond weakening by introducing porosity into the adhesive layer (bottom)

The modelled resonant frequency appeared to differ from experiment, which may be attributed to the actual adhesive having different density and stiffness to those assumed in the model. The modelled responses are shown merely to demonstrate

that the experimental results are close to what would be expected if the impedance of the adhesive is changing as the bond weakens.

Expanded versions of experimental results for both sets as well as theoretical results of Figure 3.14 are shown in Figure 3.15.

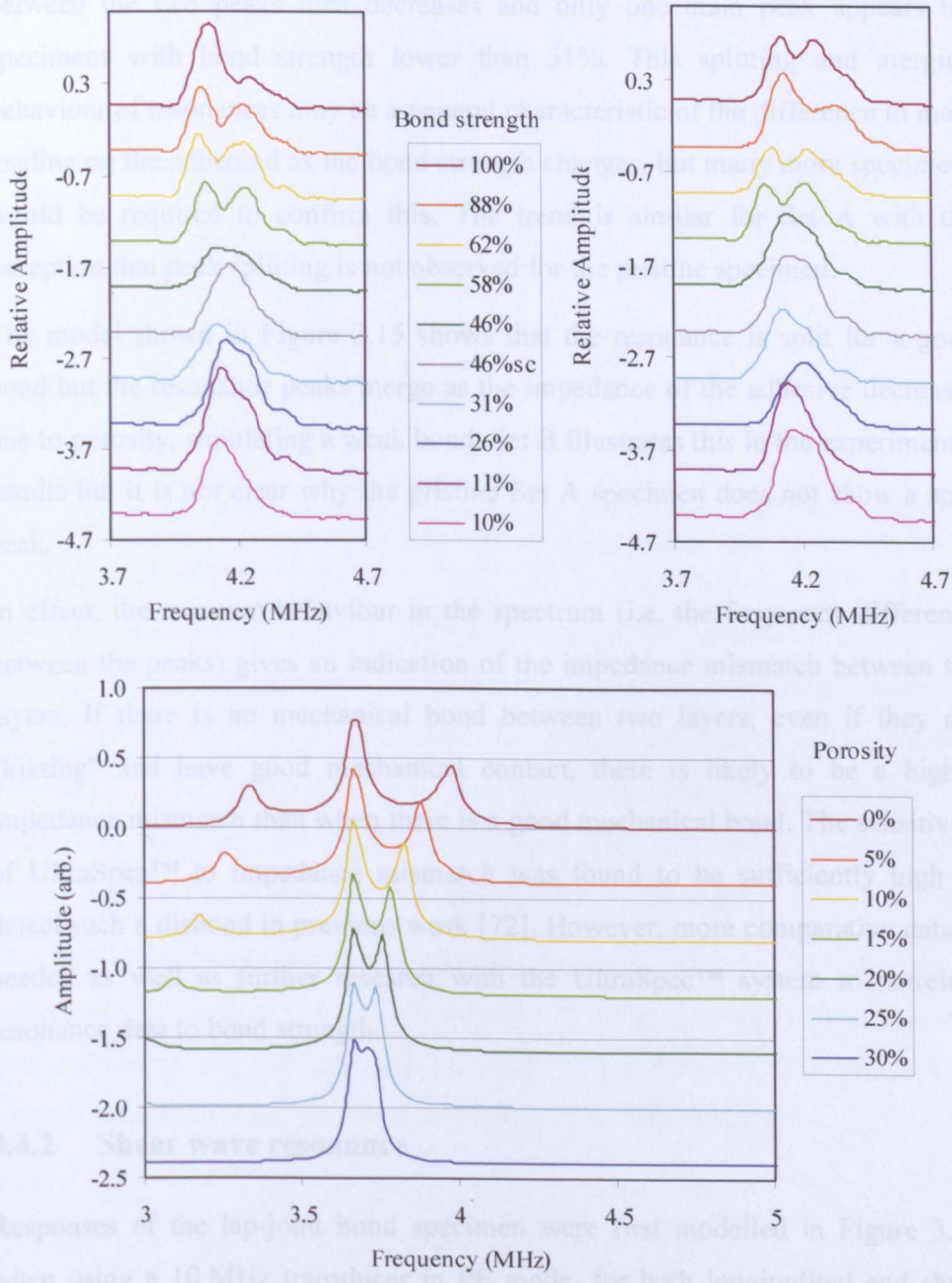

Figure 3.15. Close-up of the output frequency spectrum for Set A (top-left) and B (top-right). Also shown (bottom) is the expanded version of the modelled response as the level of porosity in the adhesive layer is changed. For better clarity, curves have been offset downwards in order of decreasing bond strength (or increasing porosity).

It should be noted that in Figure 3.15, the Set A results show different amplitudes to those of Set B due to a higher transmission voltage drive for the latter.

For Set B, there is a double peak for the pristine specimen (100% bond strength) which also appears for specimens from 88% down to 58% bond strength. The dip between the two peaks then decreases and only one main peak appears for specimens with bond strength lower than 31%. This splitting and merging behaviour of resonances may be a general characteristic of the difference in mass loading on the adherend as the bond strength changes, but many more specimens would be required to confirm this. The trend is similar for Set A with the exception that peak splitting is not observed for the pristine specimen.

The model shown in Figure 3.15 shows that the resonance is split for a good bond but the resonance peaks merge as the impedance of the adhesive decreases due to porosity, simulating a weak bond. Set B illustrates this in the experimental results but it is not clear why the pristine Set A specimen does not show a split peak.

In effect, the resonant behaviour in the spectrum (i.e. the frequency difference between the peaks) gives an indication of the impedance mismatch between the layers. If there is no mechanical bond between two layers, even if they are "kissing" and have good mechanical contact, there is likely to be a higher impedance mismatch than when there is a good mechanical bond. The sensitivity of UltraSpec™ to impedance mismatch was found to be sufficiently high to detect such a disbond in previous work [72]. However, more comparative data is needed as well as further research with the UltraSpec™ system to correlate resonance data to bond strength.

3.4.2 Shear wave resonance

Responses of the lap-joint bond specimen were first modelled in Figure 3.16 when using a 10 MHz transducer in PE mode, for both longitudinal and shear wave modes (mode conversion not included), considering the beam of a focused transducer also contains non-normal incidence wave-fronts.

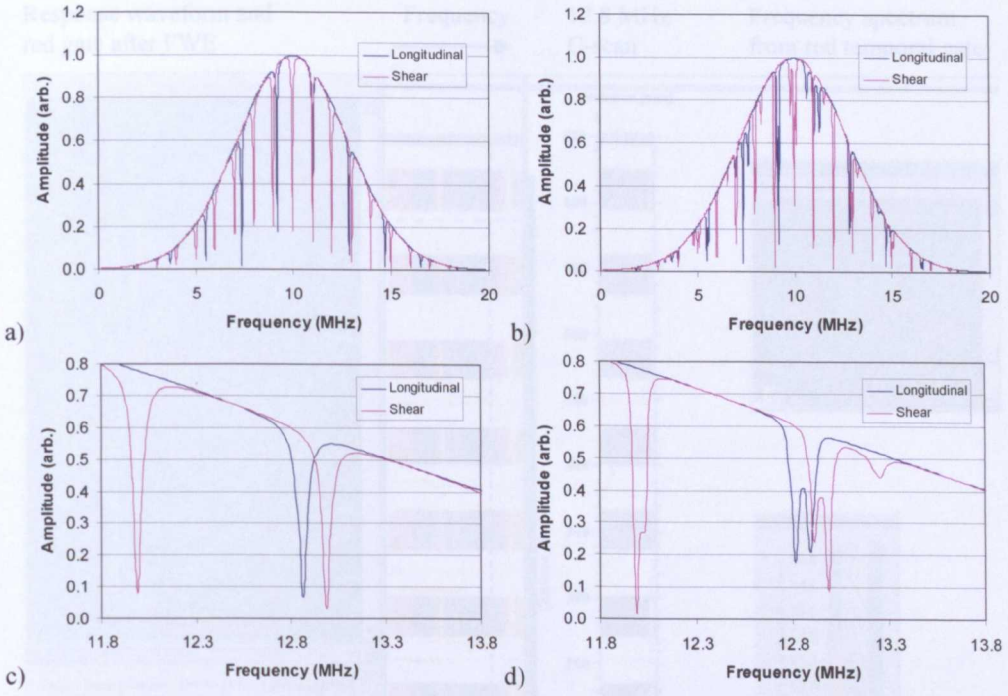

Figure 3.16. Modelled pulse-echo spectra from a 10 MHz centre-frequency Q = 1.5 transducer propagating through water and then a) and c) 1.5 mm thick steel plate – b) and d) 0.4 mm adhesive layer between two 1.5 mm thick steel adherends

The same layer model as used in the previous section determined the normal-incidence frequency response of the component using a transfer-matrix approach and convolved this with a typical transducer response. The modelling showed that at 12.8 MHz longitudinal and shear resonance frequencies coincide. The subsequent damping and shift in shear-wave resonant frequency could thus potentially be used to determine the modulus of the adhesive layer.

The specimens were scanned in pulse-echo mode with a 10 MHz focused transducer directed normally to the surfaces. A frequency-layered analysis was then carried out using ANDSCAN® (Figure 3.17) to determine in each layer the spectral amplitude at the frequency of interest over the scanned area.

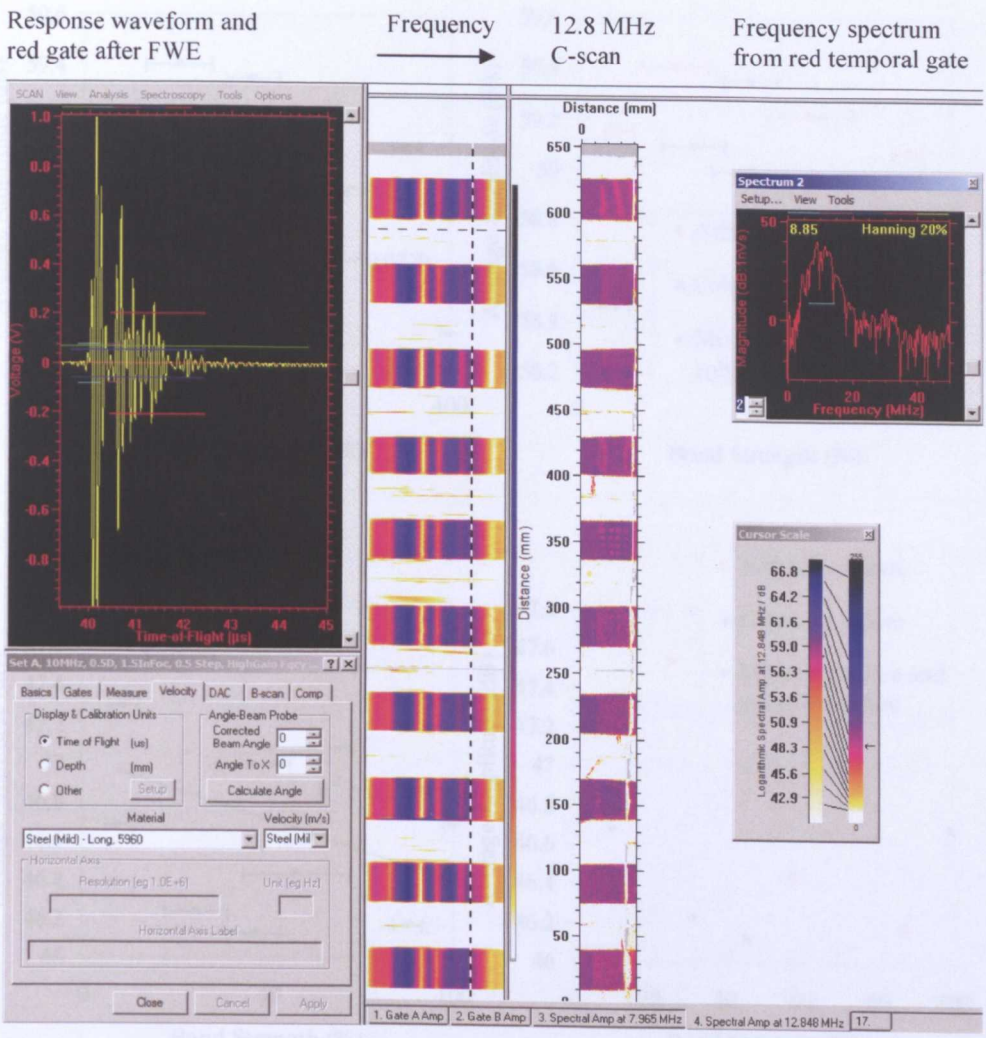

Figure 3.17. **Amplitude of the frequency spectrum (top-right) at 12.8 MHz shown as C-scans of the bonded area for a set of specimens from 10 to 100% bond strength (centre, from top to bottom) with, to the left of it, a cross-sectional slice through the frequency layers with 12.8 MHz highlighted with a dashed line**

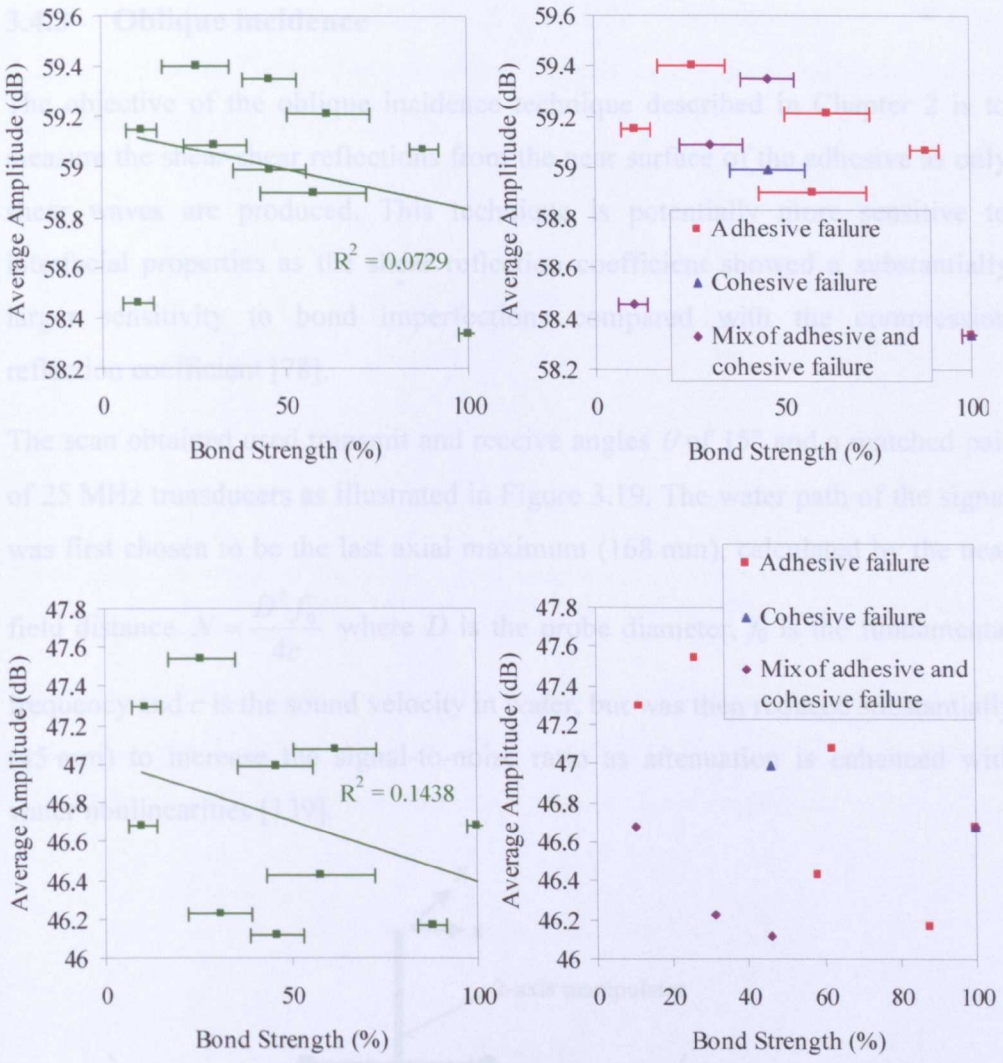

Figure 3.18. Average (over bond area) amplitude at 12.8 MHz for Set A with correlation coefficient R of -0.27 (top left) and at 14.8 MHz for Set B with R of -0.38 (bottom left). On the right the same data points are plotted with a colour code corresponding to failure mode.

Figure 3.18 shows the averaged amplitude at a particular resonant frequency as a function of bond strength, for Sets A and B. The amplitudes were obtained at 12.8 MHz for Set A; in the case of Set B, a stronger resonance was observed at 14.8 MHz. As a result, there is an observed reduction of approximately 12 dB in the frequency amplitudes for Set B, leading to a reduced signal-to-noise ratio. Linear lines of best fit are shown and the correlation coefficients do not reach the criterion for statistical significance at 5% level which is -0.55 for ten data points. There is also no obvious correlation when categorising the specimens by failure modes.

3.4.3 Oblique incidence

The objective of the oblique incidence technique described in Chapter 2 is to measure the shear-shear reflections from the near surface of the adhesive as only shear waves are produced. This technique is potentially more sensitive to interfacial properties as the shear reflection coefficient showed a substantially larger sensitivity to bond imperfections compared with the compression reflection coefficient [78].

The scan obtained used transmit and receive angles θ of 15° and a matched pair of 25 MHz transducers as illustrated in Figure 3.19. The water path of the signal was first chosen to be the last axial maximum (168 mm), calculated by the near field distance $N = \frac{D^2 f_0}{4c}$ where D is the probe diameter, f_0 is the fundamental frequency and c is the sound velocity in water, but was then reduced substantially (45 mm) to increase the signal-to-noise ratio as attenuation is enhanced with water nonlinearities [139].

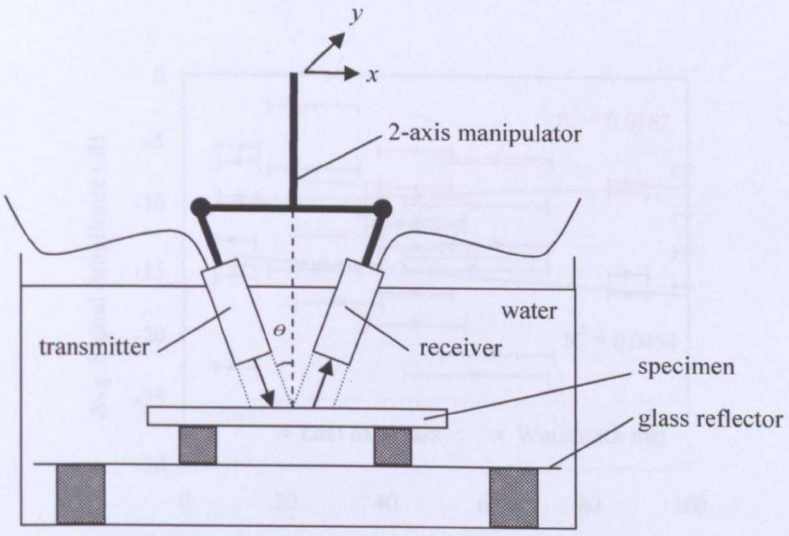

Figure 3.19. Setup for the oblique incidence measurements

Images of the bonded area are obtained by monitoring the amplitude changes of the shear-shear signal reflected from the rear of the top adherend i.e. at the interface between the steel plate (side 1) and the adhesive.

An example of two scans is shown in Figure 3.20. Degradation of the adhesive joint is visible as lighter (yellow-white) colours in the scan, and well-bonded areas represented by darker colours.

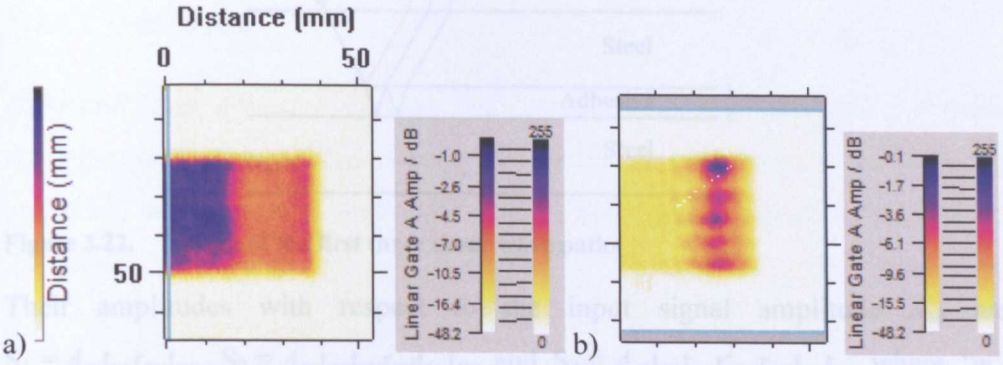

Figure 3.20. Example of the oblique incidence scan for two specimens – a) pristine specimen (100% bond strength) and b) 25% screen-application adhesive (46% bond strength)

When plotting the signal amplitude averaged over the bonded area for the last axial maximum and for the minimised water path in Figure 3.21, no significant correlation was found between bond strength and signal amplitude.

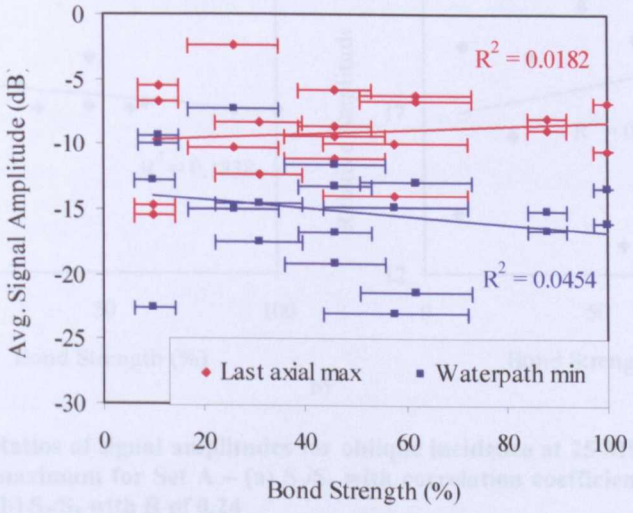

Figure 3.21. Summary of oblique incidence amplitude measurements at 25 MHz at the last axial maximum and the water path minimised with correlation coefficients, R of -0.13 and -0.21 respectively

Other amplitudes were therefore plotted to see whether any correlation with bond strength could be found. The three reflections S_1, S_2 and S_3 seen in the received signal sketched in Figure 3.22 were looked at.

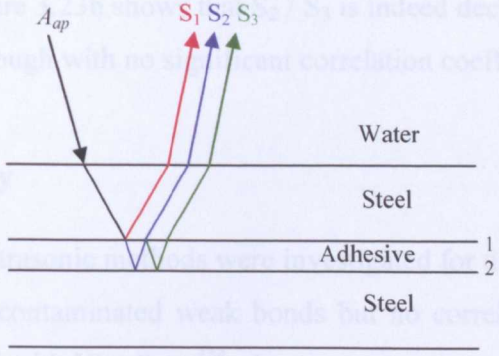

Figure 3.22. Sketch of the first three shear wave paths

Their amplitudes with respect to the input signal amplitude A_{ap} are $S_1 = A_{ap}t_{ws}r_{sa1}t_{sw}$, $S_2 = A_{ap}t_{ws}t_{sa1}r_{as2}t_{as1}t_{sw}$ and $S_3 = A_{ap}t_{ws}t_{sa1}r^2_{as2}r_{as1}t_{as1}t_{sw}$ where 'w', 's' and 'a' stand for water, steel and adhesive respectively, $t_{12} = 2Z_2 / (Z_1 + Z_2)$ and $r_{12} = (Z_2 - Z_1) / (Z_2 + Z_1)$ are the transmission and reflection coefficients from material 1 to material 2, and Z is the acoustic impedance. They were divided with one another in the following way: $S_2 / S_1 = t_{sa1}t_{as1}\, r_{as2} / r_{sa1}$ and $S_2 / S_3 = 1 / r_{as1}r_{as2}$, and plotted in Figure 3.23.

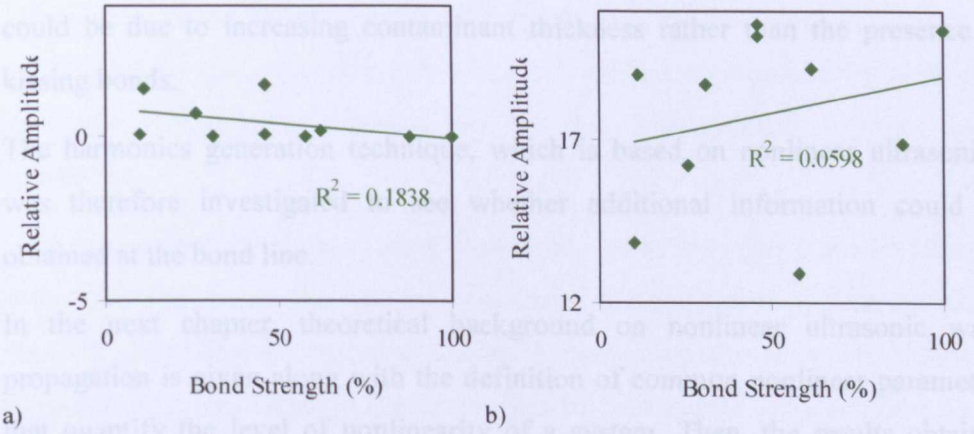

Figure 3.23. Ratios of signal amplitudes for oblique incidence at 25 MHz at the last axial maximum for Set A – (a) S_2/S_1 with correlation coefficients, R of -0.43, and (b) S_2/S_3 with R of 0.24

With the assumption that the weakened bond is characterised by a lower bulk modulus of the adhesive near the steel-adhesive interface "1" and therefore a lower acoustic impedance, the transmission coefficients t_{sa1} and t_{as1} are expected to be reduced, whereas the reflections coefficients r_{sa1} and r_{as1} should increase while the reflection coefficient from interface "2", r_{as2}, remains unaffected. It is therefore expected that both ratios S_2 / S_1 and S_2 / S_3 will decrease with weaker

bond strength. Figure 3.23b shows that S_2 / S_3 is indeed decreasing with reducing bond strength, although with no significant correlation coefficient.

3.4.4 Summary

Advanced linear ultrasonic methods were investigated for differentiating between different types of contaminated weak bonds but no correlation could either be quantified or found with UltraSpec™, shear wave resonance or oblique incidence techniques.

3.5 Conclusion

In this chapter, ultrasonic measurements were carried out on adhesive bond specimens. The only linear technique amongst DTT, PE, ultrasonic spectroscopy, shear wave resonance and oblique incidence that showed significant correlation between measured output signal amplitudes and bond strength was DTT. It was however noted that for adhesive failure specimens, the decrease in amplitude could be due to increasing contaminant thickness rather than the presence of kissing bonds.

The harmonics generation technique, which is based on nonlinear ultrasonics, was therefore investigated to see whether additional information could be obtained at the bond line.

In the next chapter, theoretical background on nonlinear ultrasonic wave propagation is given along with the definition of common nonlinear parameters that quantify the level of nonlinearity of a system. Then, the results obtained when carrying out nonlinear ultrasonic testing in through-transmission on the same sets of contaminated adhesive joints are given.

Chapter 4

Nonlinear ultrasonic theory

4.1 Introduction

In the previous chapter, linear ultrasonic techniques including double through-transmission (DTT), pulse-echo (PE), ultrasonic spectroscopy, shear wave resonance and oblique incidence were carried out on contaminated lap-joint bond specimens. A correlation between measured signal amplitude and bond strength could only be found when using DTT. However, this technique showed to be sensitive to the type of contaminant used and for adhesive failure specimens, the decrease in signal amplitude could have been due to increasing contaminant thickness rather than the presence of kissing bonds. It was therefore appropriate to investigate a nonlinear ultrasonic technique to see whether additional information could be obtained at the bond line. In this chapter, theoretical background on nonlinear ultrasonic wave propagation is given and the harmonics generation technique is carried out on the contaminated lap-joint bond specimens.

Ultrasonic testing involves sending high frequency sound energy in a structure to detect flaws. For systems that are considered linear, scattering from defects is detected and changes in speed of sound or attenuation are measured. Nonlinear ultrasonic involves different measurements such as harmonic generation where nonlinearities present in bulk materials or in the defect area for example, distort the single-frequency input signal resulting in the generation of harmonics. These non-zero amplitudes at integer multiples of the fundamental frequency can be calculated by solving the nonlinear ultrasonic wave equation.

4.2 Nonlinear ultrasonic wave equation

The derivation of the nonlinear ultrasonic wave equation can be found in numerous works ([17][87][134][135]), and here the standard approach described by Meurer in [102] is followed.

The relationship between stress σ and strain ε can be given for a unit volume by the Taylor series expansion of the constitutive law:

$$\sigma_{ij} = \frac{dU}{d\varepsilon_{ij}} \tag{4-1}$$

$$U = U_0 + a_{ij}\varepsilon_{ij} + \frac{1}{2}C_{ijkl}\varepsilon_{ij}\varepsilon_{kl} + \frac{1}{6}C_{ijklmn}\varepsilon_{ij}\varepsilon_{kl}\varepsilon_{mn} + \ldots \tag{4-2}$$

where U is the elastic strain energy, C's are the elastic coefficients and each of the indices taking on values from 1 to 3 corresponding to the x, y and z-axis.

The first two terms on the right of equation (4-2) can be set to zero, U_0 because it is an arbitrary reference energy and a_{ij} because the expansion is carried out about a state of zero stress i.e. zero strain must give zero stress. Hence, when deriving equation (4-2), equation (4-1) becomes, in the linear case, Hooke's law:

$$\sigma_{ij} = C_{ijkl}\varepsilon_{kl} \tag{4-3}$$

and when keeping one term of higher order:

$$\sigma_{ij} = C_{ijkl}\varepsilon_{kl} + \frac{1}{2}C_{ijklmn}\varepsilon_{kl}\varepsilon_{mn} \tag{4-4}$$

where C_{ijkl} and C_{ijklmn} are the second- and third-order elastic coefficients. They are so called second- and third-order because they are the second and third derivatives of U with respect to the ε_{ij}'s; however they represent a first- and second-order effect in the stress-strain relation.

Pressure P is used here to represent the components of stress in this one-dimensional (1-D) problem where equation (4-4) becomes:

$$P = K_2\varepsilon + \frac{1}{2}(3K_2 + K_3)\varepsilon^2 \tag{4-5}$$

where K_2 and K_3 are second- and third-order elastic constants. $K_2 = \rho c^2$ is the bulk modulus where ρ is the density and c is the sound velocity.

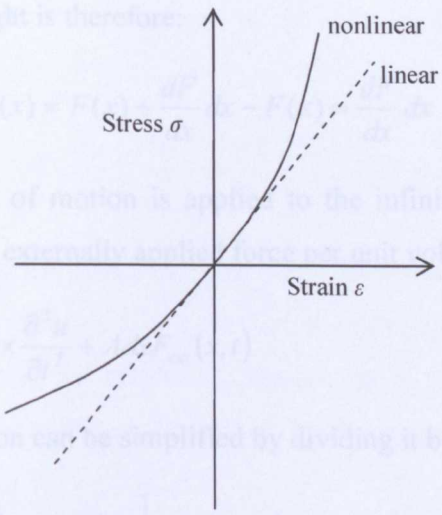

Figure 4.1. Stress-strain curve for a nonlinear material

Material damping introduces an extra pressure term associated with strain rate. With a viscous damping assumption, equation (4-5) becomes:

$$P = K_2\varepsilon + \frac{1}{2}(3K_2 + K_3)\varepsilon^2 + \delta\frac{\partial\varepsilon}{\partial t} \tag{4-6}$$

where δ is the damping coefficient.

Assuming small strains, we have $\varepsilon = \dfrac{\partial u}{\partial x}$ and (4-6) can be written as:

$$P = K_2\frac{\partial u}{\partial x} + \frac{1}{2}(3K_2 + K_3)\left(\frac{\partial u}{\partial x}\right)^2 + \delta\frac{\partial}{\partial t}\left(\frac{\partial u}{\partial x}\right) \tag{4-7}$$

If we consider an infinitely small element, dx, that has mass $\rho A dx$ where A is the cross-sectional area, the forces acting on either end of it are $F(x)$ acting to the left at one end and $F(x+dx)$ acting to the right at the other as drawn in Figure 4.2.

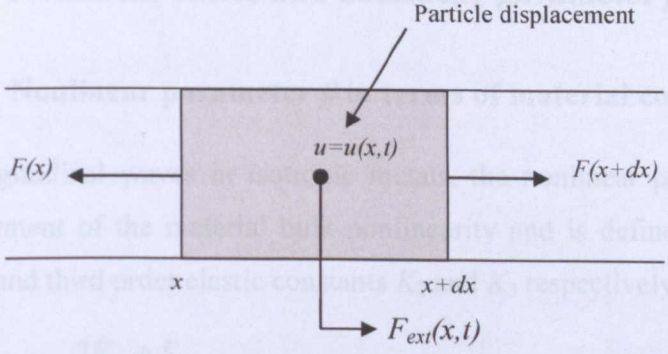

Figure 4.2. Particle displacement in an elastic bar for a 1-D ultrasonic wave

The net force to the right is therefore:

$$F(x+dx)-F(x)=F(x)+\frac{dF}{dx}dx-F(x)=\frac{dF}{dx}dx \tag{4-8}$$

Newton's second law of motion is applied to the infinitely small element dx, taking into account an externally applied force per unit volume $F_{ext}(x,t)$:

$$\frac{dF}{dx}dx=\rho A dx\times\frac{\partial^2 u}{\partial t^2}+AdxF_{ext}(x,t) \tag{4-9}$$

The previous expression can be simplified by dividing it by dx:

$$\frac{dF}{dx}=A\left[\rho\frac{\partial^2 u}{\partial t^2}+F_{ext}(x,t)\right] \tag{4-10}$$

To express the acoustic pressure described by equation (4-7) as a force, it is multiplied by the area A as $F = AP$:

$$F=A\left(K_2\frac{\partial u}{\partial x}+\frac{1}{2}(3K_2+K_3)\left(\frac{\partial u}{\partial x}\right)^2+\delta\frac{\partial}{\partial t}\left(\frac{\partial u}{\partial x}\right)\right) \tag{4-11}$$

The previous equation is differentiated with respect to x:

$$\frac{dF}{dx}=A\left(K_2\frac{\partial^2 u}{\partial x^2}+(3K_2+K_3)\frac{\partial^2 u}{\partial x^2}\frac{\partial u}{\partial x}+\delta\frac{\partial}{\partial t}\left(\frac{\partial^2 u}{\partial x^2}\right)\right) \tag{4-12}$$

Equating (4-10) and (4-12) gives the nonlinear wave equation:

$$\rho\frac{\partial^2 u}{\partial t^2}=\left[K_2+(3K_2+K_3)\frac{\partial u}{\partial x}\right]\frac{\partial^2 u}{\partial x^2}+\delta\frac{\partial}{\partial t}\left(\frac{\partial^2 u}{\partial x^2}\right)-F_{ext}(x,t) \tag{4-13}$$

4.3 Nonlinear ratios and nonlinear parameter β

4.3.1 Nonlinear parameter β in terms of material constants

For longitudinal waves in isotropic metals, the nonlinear parameter β gives a measurement of the material bulk nonlinearity and is defined as a function of second and third order elastic constants K_2 and K_3 respectively as follows:

$$\beta=-\frac{3K_2+K_3}{K_2} \tag{4-14}$$

The nonlinear equation can therefore be written for longitudinal waves in isotropic metals as:

$$\rho\frac{\partial^2 u}{\partial t^2}=\left[K_2-\beta K_2\frac{\partial u}{\partial x}\right]\frac{\partial^2 u}{\partial x^2}+\delta\frac{\partial}{\partial t}\left(\frac{\partial^2 u}{\partial x^2}\right)-F_{ext}(x,t) \qquad (4\text{-}15)$$

For an arbitrary fluid, the nonlinear parameter mentioned in literature is *B/A* where *A* and *B* are coefficients in a Taylor series expansion of the isentropic equation of state relating the material's pressure to its density [91]. *B/A* is the direct equivalent of the nonlinear parameter β mentioned in equation (4-14) for solids.

For ideal gases, *B/A* is replaced by $(\gamma-1)$ where γ is the ratio of specific heats [136].

4.3.2 Nonlinear parameter β in terms of harmonic amplitudes

The solution for the nonlinear wave equation (4-13) can be found through use of a perturbation technique ([137][86][87]). This is done by taking the solution to the linear wave equation and adding a small term that quantifies the deviation from the linear problem. This approximate solution is then substituted back into the nonlinear wave equation to find that small term. When the external force applied to the first element (at the structure boundary) $F_{ext}=AP_{ext}$ where P_{ext} is the acoustic pressure, is a sinusoidal wave, the approximate solution to the nonlinear wave equation is:

$$u(x,t)=\underbrace{\frac{1}{8}\beta k^2 A_1^2 x}_{A_0}+A_1\sin(-k(x-ct))-\underbrace{\frac{1}{8}\beta k^2 A_1^2 x}_{A_2}\sin(-2k(x-ct))+\ldots \qquad (4\text{-}16)$$

where k is the wavenumber, x is the propagation distance, A_0 is the direct current (DC) amplitude, A_1 is the amplitude of the centre frequency output signal and A_n ($n > 1$) is the amplitude of the n^{th} harmonic in the frequency spectrum.

In other words, when a sinusoidal wave of amplitude A_{ap} and fundamental frequency $f_0 = kc/2\pi$ is sent into a linear medium, the output is a sinusoidal wave of amplitude A_1 and frequency f_0. If the medium is nonlinear, then sinusoidal waves of amplitude A_n of nf_0 frequency where $n > 1$ called higher

harmonics are generated in the output. Higher harmonics can be seen in the frequency spectrum of the output signal, and their amplitudes measured as seen in Figure 4.3.

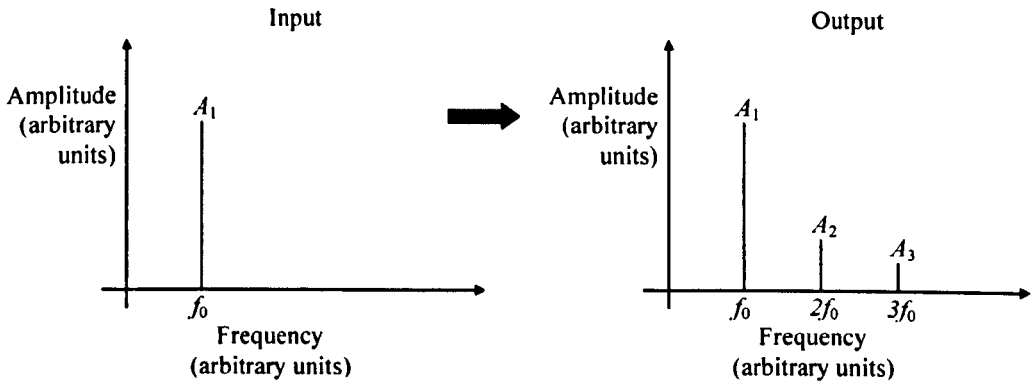

Figure 4.3. Amplitudes A_1, A_2 and A_3 in input and output frequency spectra

From the amplitude of the second harmonic A_2 in equation (4-16), the nonlinear parameter β can be expressed for undamped materials as:

$$\beta = \frac{8}{k^2 x}\frac{A_2}{A_1^2} \tag{4-17}$$

which involves the calculation of the nonlinear ratio Φ (Appendix B):

$$\Phi = \frac{A_2}{A_1^2} \tag{4-18}$$

In some cases, when higher harmonics such as the third harmonic are of interest, the following ratios are calculated:

$$\Phi_3 = \frac{A_3}{A_1^2} \tag{4-19}$$

$$\kappa = \sqrt{\frac{\sum_{n=2}^{\infty} A_n^2}{\sum_{n=1}^{\infty} A_n^2}} \tag{4-20}$$

where A_1, A_2, ..., A_n are the amplitudes of the fundamental frequency, second, ..., n^{th} harmonics respectively in the frequency spectrum of the received signal.

The ratio κ is called the distortion factor and gives the overall nonlinear content of the signal. A higher nonlinear ratio is an indication of higher nonlinearity.

The technique that involves the measurement of such nonlinear parameters and ratios is called the harmonic generation technique.

4.4 Nonlinear ultrasonic technique

For nonlinear measurements, the assumption is that an imperfect interface such as a kissing bond might introduce contact nonlinearity due to intermittent contact ('clapping') or frictional forces. Such nonlinear coupling would be expected to convert incident ultrasonic energy into harmonics of the exciting frequency, both in transmission and reflection. The idea is therefore to examine harmonics in the output frequency spectrum.

The nonlinear high-frequency transmission technique (NHFTT) [7] was used for these nonlinear measurements carried out on the contaminated adhesive joints described in Chapter 3. The experimental set-up is shown in Figure 4.4.

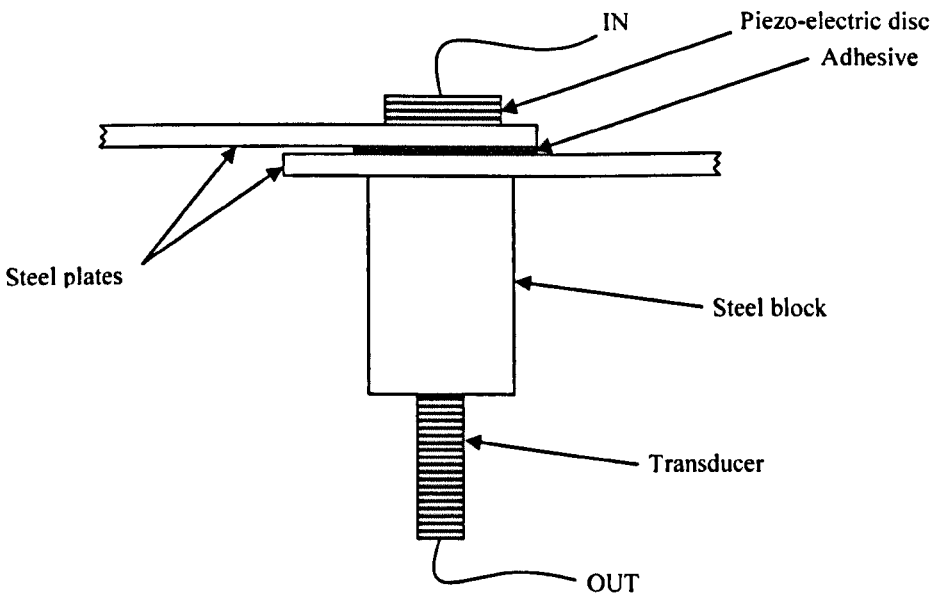

Figure 4.4. Schematic of the set-up for nonlinear measurements

An undamped piezoelectric disc (Pz26) was bonded using cyanoacrylate (i.e. "Super Glue") on one end of the specimen. The piezoelectric disc was driven by a 15-cycle tone-burst signal which was generated using an arbitrary function generator (AFG), and power amplified to 80V amplitude (zero to peak). The signal on the other side of the specimen was passed through a 30 mm thick steel block to create a delay and minimise crosstalk. Crosstalk is an electrical effect

where the signal leaks across between neighbouring wires. By adding a delay, the received signal could easily be separated from the electrical crosstalk appearing earlier in the time-domain signal. It was then received by a damped 5 MHz ultrasonic transducer before being amplified and digitised. The frequency spectrum of the transmitted signal was calculated for each specimen and plotted as seen in Figure 4.5.

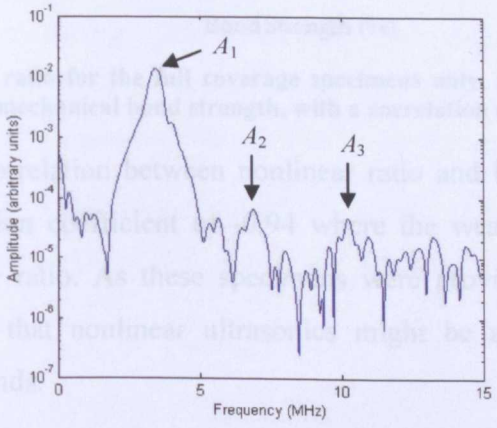

Figure 4.5. Example of output frequency spectrum (68% bond strength specimen). A_1, A_2 and A_3 are the amplitudes of the fundamental, second and third harmonics respectively.

The amplitudes A_1, A_2 and A_3 of the fundamental frequency, second and third harmonics respectively as shown in Figure 4.5 were measured and nonlinear ratios calculated. Across all twenty specimens no significant linear correlation could be found between nonlinear ratios and bond strength. In effect, there was no assurance that kissing bonds were present in any of the specimens. Also, for specimens in which the contaminant or the adhesive was applied with a screen, a single point measurement per bonded area is not representative of the whole area as it might be taken over a pristine, disbonded or contaminated area. Therefore, nonlinear ratios only for adhesive failure specimens where no screen was used were plotted against bond strength in Figure 4.6.

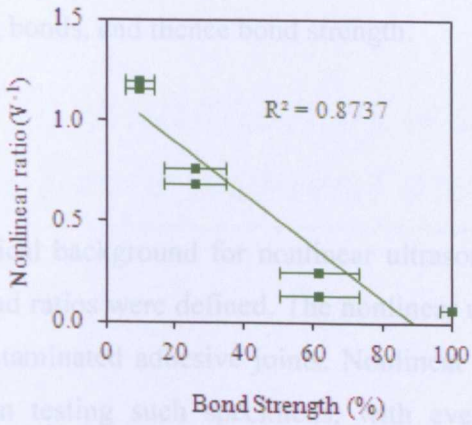

Figure 4.6. Nonlinear ratio for the full coverage specimens only, plotted against their measured mechanical bond strength, with a correlation coefficient of -0.94

A significant linear correlation between nonlinear ratio and bond strength was found with a correlation coefficient of -0.94 where the weaker the bond, the stronger the nonlinear ratio. As these specimens were providing for adhesive failure, this suggests that nonlinear ultrasonics might be able to detect the presence of kissing bonds.

It should however be noted that these measurements were limited to single point measurements. Also, it would not be practical for an inspection technique to have a piezoelectric disc glued to the specimen but the implications of using a transmitting transducer are not yet known considering that nonlinearities would not only occur at the bond interface. Other sources of nonlinearities include contributions from the electronic equipment, transducers, coupling medium, and material itself. The side lobes which are generated by the signal post-processing technique can also interfere on the second harmonic nonlinearity.

In order to establish the prospects of this nonlinear technique in the context of adhesive joints, it was therefore necessary firstly to be able to simulate the response of multilayer structures, incorporating kissing bonds, to nonlinear ultrasonics. Such a model should also incorporate other sources of nonlinearity which may arise from the measurement equipment used and also the material itself. A finite element model approach was developed, providing the facility to accommodate and incorporate nonlinearities from various sources. The model is expected to provide insights on the measurement scenario from which optimum measurement methodologies and appropriate signal processing procedures could

be derived and combined to produce a tractable technique for quantitative measurement of kissing bonds, and thence bond strength.

4.5 Conclusion

In this chapter, theoretical background for nonlinear ultrasonics was given and nonlinear parameters and ratios were defined. The nonlinear ultrasonic technique was carried out on contaminated adhesive joints. Nonlinear ultrasonics showed promising results when testing such specimens, with even slightly stronger correlation between measured nonlinear ratio and bond strength than the correlations obtained in the previous chapter with linear ultrasonics.

In the following chapter, a one dimensional finite element model is developed to simulate nonlinear wave propagation in multilayer structures.

Chapter 5

Theoretical formulation of a one-dimensional finite element model

5.1 Introduction

In the previous chapter, theoretical background for nonlinear ultrasonics was given and nonlinear parameters and ratios were defined. Nonlinear ultrasonic measurements were carried out on contaminated adhesive joints and showed promising results. In order to establish the prospects of this nonlinear technique in the context of adhesive joints, a time-domain finite element (FE) type model of one-dimensional (1-D) nonlinear wave propagation is developed in this chapter. This is to deliver a generalised 1-D model which provides a capability to quantitatively determine the detectability of defect-induced nonlinear effects.

5.2 An approximate discrete formulation of the nonlinear wave equation

The following FE model is a 1-D discretisation of the continuum into line elements of length Δx, uniform cross-sectional area A and the bulk modulus K_2. Nodes are located at each end of the line element, and each node has a displacement u in the x-direction. The vector $\mathbf{u} = [u_k, u_{k+1}]^T$ gives the displacements associated with the k^{th} node and its neighbouring node in the FE model.

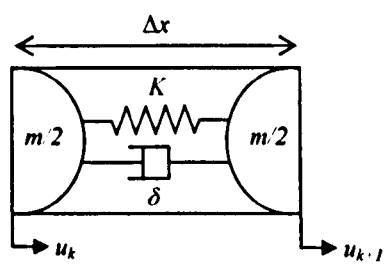

Figure 5.1. **Schematic of an element of mass m where the spring has stiffness K and the dashpot has damping δ**

The shape function that describes the displacements anywhere in the element can be written as follows:

$$u(x) = u_k + \frac{u_{k+1} - u_k}{\Delta x} x = \begin{bmatrix} N_k & N_{k+1} \end{bmatrix} \begin{bmatrix} u_k \\ u_{k+1} \end{bmatrix} = \mathbf{Nu} \tag{5-1}$$

where $N_k = \frac{1}{\Delta x}(\Delta x - x)$ and $N_{k+1} = \frac{1}{\Delta x} x$.

For small displacements, strain ε can be obtained by differentiating (5-1) with respect to x:

$$\varepsilon = \frac{du(x)}{dx} = \frac{u_{k+1} - u_k}{\Delta x} = \frac{1}{\Delta x} \begin{bmatrix} -1 & 1 \end{bmatrix} \begin{bmatrix} u_k \\ u_{k+1} \end{bmatrix} = \mathbf{Bu} \tag{5-2}$$

where $\mathbf{B} = \frac{1}{\Delta x} \begin{bmatrix} -1 & 1 \end{bmatrix}$ is the dimension vector.

The strain variation $\Delta\boldsymbol{\varepsilon}$ compatible with the displacement variation $\Delta\mathbf{u}$ and its rate $\Delta\dot{\boldsymbol{\varepsilon}}$ can therefore be written as follows:

$$\Delta\boldsymbol{\varepsilon} = \mathbf{B}\Delta\mathbf{u} \qquad \text{and} \qquad \Delta\dot{\boldsymbol{\varepsilon}} = \mathbf{B}\Delta\dot{\mathbf{u}} \tag{5-3}$$

The change in stress is:

$$\Delta\boldsymbol{\sigma} = \boldsymbol{\gamma}\Delta\boldsymbol{\varepsilon} + \delta\Delta\dot{\boldsymbol{\varepsilon}} \tag{5-4}$$

where $\boldsymbol{\gamma} = K_2 + \frac{1}{2}(3K_2 + K_3)\boldsymbol{\varepsilon}$, K_2 and K_3 are the second- and third-order elastic constants, and δ is the damping coefficient.

Each element is subjected to nodal forces resulting in stresses σ and small nodal displacements Δu and strains $\Delta\varepsilon$. Applying the principle of dynamic virtual work, the work done within an element is equal to the external work done by the forces applied at its nodes.

Within an element, the total work done by the internal forces comprises work done by inertial forces as well as strain energy:

$$W_{\text{int}} = \frac{1}{2} \int \rho \mathbf{N}^T \mathbf{N} \Delta\mathbf{u}^T \cdot \ddot{\mathbf{u}}\, dV + \int (\Delta\boldsymbol{\varepsilon})^T \boldsymbol{\sigma}\, dV \tag{5-5}$$

where ρ is the density and V is the element volume.

The external work is the work done by the forces $\mathbf{F}$ at the nodes:

$$W_{ext} = \Delta\mathbf{u}^T \cdot \mathbf{F} \tag{5-6}$$

Equating internal and external work:

$$\frac{1}{2}\int \rho \mathbf{N}^T \mathbf{N} \Delta\mathbf{u}^T \cdot \ddot{\mathbf{u}}\, dV + \int (\Delta\varepsilon)^T \boldsymbol{\sigma}\, dV = \Delta\mathbf{u}^T \cdot \mathbf{F}$$

$$\Delta\mathbf{u}^T \left\{ \frac{1}{2}\int \rho \mathbf{N}^T \mathbf{N} \ddot{\mathbf{u}}\, dV + \int \mathbf{B}^T \boldsymbol{\sigma}\, dV \right\} = \Delta\mathbf{u}^T \cdot \mathbf{F}$$

$$\Delta\mathbf{u}^T \left\{ \frac{1}{2}\int \rho \mathbf{N}^T \mathbf{N} \ddot{\mathbf{u}}\, dV + \int \mathbf{B}^T (\gamma\varepsilon + \delta\dot{\varepsilon}) dV \right\} = \Delta\mathbf{u}^T \cdot \mathbf{F}$$

$$\left(\frac{1}{2}\int \rho \mathbf{N}^T \mathbf{N}\, dV \right) \ddot{\mathbf{u}} + \int \mathbf{B}^T \gamma\varepsilon\, dV + \int \mathbf{B}^T \delta\dot{\varepsilon}\, dV = \mathbf{F}$$

$$\left(\frac{1}{2}\int \rho \mathbf{N}^T \mathbf{N} dV \right) \ddot{\mathbf{u}} + \left(\int \mathbf{B}^T \gamma \mathbf{B}\, dV \right) \mathbf{u} + \left(\int \mathbf{B}^T \delta \mathbf{B}\, dV \right) \dot{\mathbf{u}} = \mathbf{F}$$

$$\left(\frac{1}{2}\int \rho \mathbf{N}^T \mathbf{N} dV \right) \ddot{\mathbf{u}} + \left(\int \mathbf{B}^T \delta \mathbf{B}\, dV \right) \dot{\mathbf{u}} \ldots$$

$$\ldots + \left(\int \mathbf{B}^T \left(K_2 + \frac{1}{2}(3K_2 + K_3)\varepsilon \right) \mathbf{B}\, dV \right) \mathbf{u} = \mathbf{F}$$

$$\left(\frac{1}{2}\int \rho \mathbf{N}^T \mathbf{N} dV \right) \ddot{\mathbf{u}} + \left(\int \mathbf{B}^T \delta \mathbf{B}\, dV \right) \dot{\mathbf{u}} \ldots$$

$$\ldots + \left(\int \mathbf{B}^T K_2 \mathbf{B}\, dV + \int \mathbf{B}^T \frac{1}{2}(3K_2 + K_3) \mathbf{B}\varepsilon\, dV \right) \mathbf{u} = \mathbf{F} \tag{5-7}$$

The discretised form of equation (5-7) gives the equilibrium equation for each element:

$$\{\mathbf{M}\}^e \ddot{\mathbf{u}} + \{\mathbf{D}\}^e \dot{\mathbf{u}} + \left(\{\mathbf{K}_L\}^e + \{\mathbf{K}_{NL}(\mathbf{u})\}^e \right) \mathbf{u} = \mathbf{F} \tag{5-8}$$

where the element mass matrix $\{\mathbf{M}\}^e$ is the integral expression:

$$\{\mathbf{M}\}^e = \frac{1}{2}\int \rho \mathbf{N}^T \mathbf{N} dV = \frac{\rho A \Delta x}{2} \begin{bmatrix} 1 & 0 \\ 0 & 1 \end{bmatrix} \tag{5-9}$$

The element damping matrix $\{\mathbf{D}\}^e$ is the integral expression:

$$\{\mathbf{D}\}^e = \int_V \delta \mathbf{B}^T \mathbf{B}\, dV = \delta \frac{1}{\Delta x} \begin{bmatrix} -1 \\ 1 \end{bmatrix} \frac{1}{\Delta x} \begin{bmatrix} -1 & 1 \end{bmatrix} A \Delta x = \frac{\delta A}{\Delta x} \begin{bmatrix} 1 & -1 \\ -1 & 1 \end{bmatrix} \tag{5-10}$$

The element linear stiffness matrix $\{\mathbf{K}_L\}^e$ is the integral expression:

$$\{\mathbf{K}_L\}^e = \int_V \mathbf{B}^T K_2 \mathbf{B}\, dV$$

$$= \frac{1}{\Delta x}\begin{bmatrix}-1\\1\end{bmatrix} K_2 \frac{1}{\Delta x}\begin{bmatrix}-1 & 1\end{bmatrix} A\Delta x = \frac{K_2 A}{\Delta x}\begin{bmatrix}1 & -1\\-1 & 1\end{bmatrix} \tag{5-11}$$

The element nonlinear stiffness matrix $\{\mathbf{K}_{NL}\}^e$ is the integral expression:

$$\{\mathbf{K}_{NL}\}^e = \int_V \mathbf{B}^T \frac{1}{2}(3K_2 + K_3)\mathbf{B}\boldsymbol{\varepsilon}\, dV$$

$$= \frac{1}{\Delta x}\begin{bmatrix}-1\\1\end{bmatrix}\frac{1}{2}(3K_2 + K_3)\frac{1}{\Delta x}\begin{bmatrix}-1 & 1\end{bmatrix}\boldsymbol{\varepsilon} A\Delta x$$

$$= \frac{3K_2 + K_3}{2}\frac{A}{\Delta x}\begin{bmatrix}1 & -1\\-1 & 1\end{bmatrix}\boldsymbol{\varepsilon} \tag{5-12}$$

The element matrices are then put into place in the global matrix equation by adding each element of the structure:

$$\mathbf{M}\ddot{\mathbf{u}} + \mathbf{D}\dot{\mathbf{u}} + (\mathbf{K} + \mathbf{K}_{NL}(\mathbf{u}))\mathbf{u} = \mathbf{F}_{ext} \tag{5-13}$$

where **M**, **D**, **K** and $\mathbf{K}_{NL}(\mathbf{u})$ are the mass, damping, stiffness and nonlinear stiffness matrices respectively, and **u** is the displacement vector with its associated derivatives with respect to time ($\ddot{\mathbf{u}} = \frac{\partial^2 \mathbf{u}}{\partial t^2}$ and $\dot{\mathbf{u}} = \frac{\partial \mathbf{u}}{\partial t}$).

As an example for setting the matrices, a two-layer 1-D structure made of materials 1 and 2 is considered and illustrated in Figure 5.2.

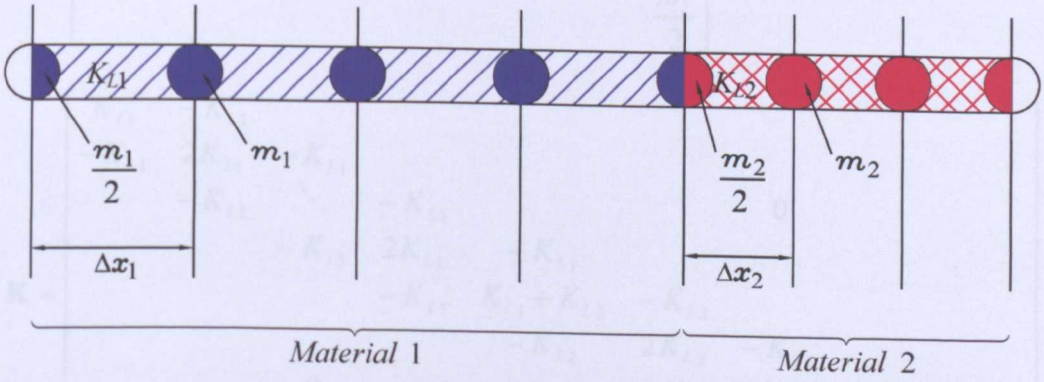

Figure 5.2. Schematic of the mechanical elements for a two-layer structure

All diagonal terms are positive and are directly attached to the corresponding nodes. Furthermore, all non-diagonal terms are negative and symmetric. They are

symmetric since they are attached to two elements and the effects are the same in these two elements (a condition known as Maxwell's Reciprocity Theorem). They are negative due to the relative displacements/velocities of the two attached nodes.

Matrices written for each element give the masses, stiffnesses and damping for the pair of nodes due to the line element between them:

$$\{\mathbf{M}\}^e = \begin{bmatrix} \frac{m_i}{2} & 0 \\ 0 & \frac{m_i}{2} \end{bmatrix}, \{\mathbf{K}_L\}^e = \begin{bmatrix} K_{Li} & -K_{Li} \\ -K_{Li} & K_{Li} \end{bmatrix}, \{\mathbf{D}\}^e = \begin{bmatrix} \delta_i & -\delta_i \\ -\delta_i & \delta_i \end{bmatrix}$$

where i is the element's material.

These element matrices are then combined by adding the mass, stiffness and damping contributions for both the elements that share each node to obtain the overall global matrices:

$$\mathbf{M} = \begin{bmatrix} \frac{m_1}{2} & & & & & & & & \\ & m_1 & & & & & & & \\ & & \ddots & & & 0 & & & \\ & & & m_1 & & & & & \\ & & & & \frac{m_1}{2}+\frac{m_2}{2} & & & & \\ & & & & & m_2 & & & \\ & & 0 & & & & \ddots & & \\ & & & & & & & m_2 & \\ & & & & & & & & \frac{m_2}{2} \end{bmatrix} \tag{5-14}$$

$$\mathbf{K} = \begin{bmatrix} K_{L1} & -K_{L1} & & & & & & & \\ -K_{L1} & 2K_{L1} & -K_{L1} & & & & & & \\ & -K_{L1} & \ddots & -K_{L1} & & & 0 & & \\ & & -K_{L1} & 2K_{L1} & -K_{L1} & & & & \\ & & & -K_{L1} & K_{L1}+K_{L2} & -K_{L2} & & & \\ & & & & -K_{L2} & 2K_{L2} & -K_{L2} & & \\ & & 0 & & & -K_{L2} & \ddots & -K_{L2} & \\ & & & & & & -K_{L2} & 2K_{L2} & -K_{L2} \\ & & & & & & & -K_{L2} & K_{L2} \end{bmatrix} \tag{5-15}$$

$$\mathbf{D}=\begin{bmatrix}
\delta_1 & -\delta_1 & & & & & & & \\
-\delta_1 & 2\delta_1 & -\delta_1 & & & & & & \\
 & -\delta_1 & \ddots & -\delta_1 & & & 0 & & \\
 & & -\delta_1 & 2\delta_1 & -\delta_1 & & & & \\
 & & & -\delta_1 & \delta_1+\delta_2 & -\delta_2 & & & \\
 & & & & -\delta_2 & 2\delta_2 & -\delta_2 & & \\
 & & 0 & & & -\delta_2 & \ddots & -\delta_2 & \\
 & & & & & & -\delta_2 & 2\delta_2 & -\delta_2 \\
 & & & & & & & -\delta_2 & \delta_2
\end{bmatrix} \quad (5\text{-}16)$$

Taking into account inherent material nonlinearity (K_{NL1} and K_{NL2}), the nonlinear stiffness matrix K_{NL} is defined as follows:

$$\mathbf{K}_{NL}=\begin{bmatrix}
K_{NL1} & -K_{NL1} & & & & & & & & & \\
-K_{NL1} & 2K_{NL1} & -K_{NL1} & & & & & & & & \\
 & -K_{NL1} & \ddots & -K_{NL1} & & & & 0 & & & \\
 & & -K_{NL1} & 2K_{NL1} & -K_{NL1} & & & & & & \\
 & & & -K_{NL1} & K_{NL1}+K_{NL2} & -K_{NL2} & & & & & \\
 & & & & -K_{NL2} & 2K_{NL2} & -K_{NL2} & & & & \\
 & & 0 & & & -K_{NL2} & \ddots & -K_{NL2} & & & \\
 & & & & & & -K_{NL2} & 2K_{NL2} & -K_{NL2} & & \\
 & & & & & & & -K_{NL2} & K_{NL2} & &
\end{bmatrix} \quad (5\text{-}17)$$

If material i is linear, then $K_{NL,i}=0$.

The main values used in the four diagonal and tridiagonal matrices are as follows:

$$\begin{cases}
m=\rho A\Delta x \\
\delta=\dfrac{\alpha f_0}{\Delta x}\dfrac{2Z}{k^2}A \\
K_L=K_2\dfrac{A}{\Delta x} \\
K_{NL}(u)=\left(\dfrac{3K_2+K_3}{2}\right)\dfrac{A}{\Delta x}\dfrac{\partial u}{\partial x}
\end{cases}$$

where α is the attenuation coefficient, f_0 is the fundamental frequency, Z is the acoustic impedance and k is the wavenumber.

The second-order elastic constant K_2 is the bulk modulus of the material:

$$K_2 = \rho c^2 \tag{5-18}$$

where c is the sound velocity in this material.

Values for the third-order elastic constant can either be found in the literature or deduced from known values for β e.g. $\beta = -\dfrac{3K_2 + K_3}{K_2}$ for longitudinal waves in an isotropic solid.

The equilibrium equation for each node is contained in the whole model. The nodal force (resulting from element displacement) must be equal and opposite to the externally applied force $\mathbf{F}_{ext}$:

$$\mathbf{F}_{ext} = \begin{bmatrix} F_1 \\ F_2 \\ \vdots \\ \\ \\ \\ F_n \end{bmatrix} \tag{5-19}$$

5.3 The computational algorithm

The finite difference time discretisation of the second and first derivatives of displacement with respect to time in (5-13) is accomplished by central and backward difference approximations respectively:

$$\ddot{\mathbf{u}}_t \cong \frac{1}{\Delta t^2}\left[\mathbf{u}_{t+\Delta t} - 2\mathbf{u}_t + \mathbf{u}_{t-\Delta t}\right] \tag{5-20}$$

$$\dot{\mathbf{u}}_t \cong \frac{1}{\Delta t}\left[\mathbf{u}_t - \mathbf{u}_{t-\Delta t}\right] \tag{5-21}$$

where $\ddot{\mathbf{u}}_t$ and $\dot{\mathbf{u}}_t$ are the approximations for the second and first time derivatives of $\mathbf{u}$, Δt is the time step, and $\mathbf{u}_{t+\Delta t}$, $\mathbf{u}_t$, $\mathbf{u}_{t-\Delta t}$ are values of displacements at the three consecutive time instants $t + \Delta t$, t and $t - \Delta t$.

Replacing $\ddot{\mathbf{u}}$ and $\dot{\mathbf{u}}$ by (5-20) and (5-21) in (5-13) as well as keeping only $\mathbf{u}_{t+\Delta t}$ on the left hand side of the equation to get the displacement at time $t+\Delta t$, the following algorithm is obtained:

$$\mathbf{u}_{t+\Delta t} = \underbrace{\Delta t^2 \mathbf{M}^{-1}\mathbf{F}}_{ext.force} - \underbrace{\Delta t^2 \mathbf{M}^{-1}(\mathbf{K}+\mathbf{K}_{NL}(\mathbf{u}_t))\mathbf{u}_t}_{stiffness} + \underbrace{\Delta t \mathbf{M}^{-1}\mathbf{D}(\mathbf{u}_{t-\Delta t}-\mathbf{u}_t)}_{damping} + 2\mathbf{u}_t - \mathbf{u}_{t-\Delta t} \tag{5-22}$$

It should be noted that the gradient values $\frac{\partial u}{\partial x}$ in the nonlinear matrix $\mathbf{K}_{NL}(\mathbf{u}_t)$ are calculated in each time step.

5.4 Summary

In this chapter, the 1-D FE model was developed by dividing the continuum into line elements, finding their equilibrium equation, adding their contributions to form global matrices and deriving the time-domain computational algorithm. This specific implementation was coded in Matlab by the author.

It should be noted that the 1-D model is sufficient for understanding the nonlinear phenomenon but is limited to modelling compression waves. Extending it to two-dimensions (2-D) would enable shear waves to be modelled as well and would therefore enable mode conversion to be taken into account. With a 2-D model, oblique-incidence methods could be simulated.

In the following chapter, the 1-D FE model is validated for both linear and nonlinear wave propagation.

Chapter 6

Validation of the one-dimensional finite element model

6.1 Introduction

In the previous chapter, the theoretical formulation of the one-dimensional (1-D) finite element (FE) model was given by developing the algorithm that simulates ultrasonic nonlinear wave propagation.

In this chapter, the model is first validated in the linear regime against experimental data and verified against an input impedance model. Material nonlinearity is then introduced and the model is validated for nonlinear wave propagation by recovering the specified material nonlinearity parameter β from the model output. Subtleties such as the scalings that must be performed are explained.

6.2 Validation for linear wave propagation

In this section, the time-domain FE type model of 1-D wave propagation is benchmarked against an input impedance model in order to validate it for linear ultrasonic wave propagation.

Acoustic wave propagation is studied by means of an input impedance approach, analogous to transmission line theory [140] and its derivation can be found in Appendix A. The model yields results that are mathematically identical to those obtained using the transfer matrix approach of Wilcox et al. [141], Thomson [142], Haskell [143], Pialucha [144], Challis *et al.* [50] and Mienczakowski et al. [145] – they are all exact solutions to the 1-D wave equation.

6.2.1 Computational approach of input impedance model

The basic calculation procedure is executed in the frequency domain. For a multi-layered structure, the impedance is calculated recursively looking into successive layers, working back from the final interface numbered 1 towards the transducer. The input impedance for the n^{th} layer is:

$$Z_{in}^{(n)} = \left(\frac{Z_{in}^{(n-1)} + iZ_n \tan\phi_n}{Z_n + iZ_{in}^{(n-1)} \tan\phi_n} \right) Z_n \qquad (6\text{-}1)$$

where for normal incidence $\phi_n = k_n d_n$, k_n is the wave number, d_n is the layer thickness and Z_{in} is defined as the acoustic impedance of the reflecting medium.

In principle, any input signal can be sent into the structure and is defined by the user. It would however typically be tonebursts of some prescribed window shape (e.g. Hanning, Gaussian) described by two parameters, centre frequency f_0 and quality factor Q which controls its frequency bandwidth. An arbitrary stand-off delay is applied in order to minimise problems with wrap-around in time. The multi-layered structure is specified in terms of the constituent materials and their respective thicknesses. The number of points in the frequency-domain output array, and hence the duration of the simulated time-domain waveform, is determined by the time range and time step parameters, and these are again specified by the user.

The impedance is calculated for each layer starting from the last layer, incrementing towards the transducer, using equation (6-1).

The particle velocity on the top surface v_{out} is:

$$v_{out} = \frac{P_{ext}}{Z_{in}^{(n)}} \qquad (6\text{-}2)$$

where P_{ext} is the externally input acoustic pressure.

Hence the displacement u_{out} in the frequency domain is:

$$u_{out}(\omega) = \frac{v_{out}}{i\omega}, \qquad (6\text{-}3)$$

where $\omega = 2\pi f_0$ is the circular frequency and $\sqrt{i} = -1$.

The inverse Fourier transform applied to the output displacement in the frequency domain gives the output time-domain signal:

$$u_{out}(t) = 2\,\mathrm{Re}\left(\int u_{out}(\omega) e^{it\omega} d\omega\right) \tag{6-4}$$

If the specimen is immersed in water, the reflection coefficient r is:

$$r = \frac{Z_{water} - Z_{in}^{(n)}}{Z_{water} + Z_{in}^{(n)}} \tag{6-5}$$

and the acoustic pressure P_{out} is:

$$P_{out}(t) = 2\,\mathrm{Re}\left(\int P_{out}(\omega) e^{it\omega} d\omega\right) \tag{6-6}$$

where $P_{out}(\omega) = rP_{in}(\omega)$.

6.2.2 Validation of models against experimental data

The simulated pulse-echo (PE) response from an adhesive joint — similar to those studied in Chapter 3 — was compared with the experimental A-scan for the pristine specimen (100% bond strength) as shown in Figure 6.1.

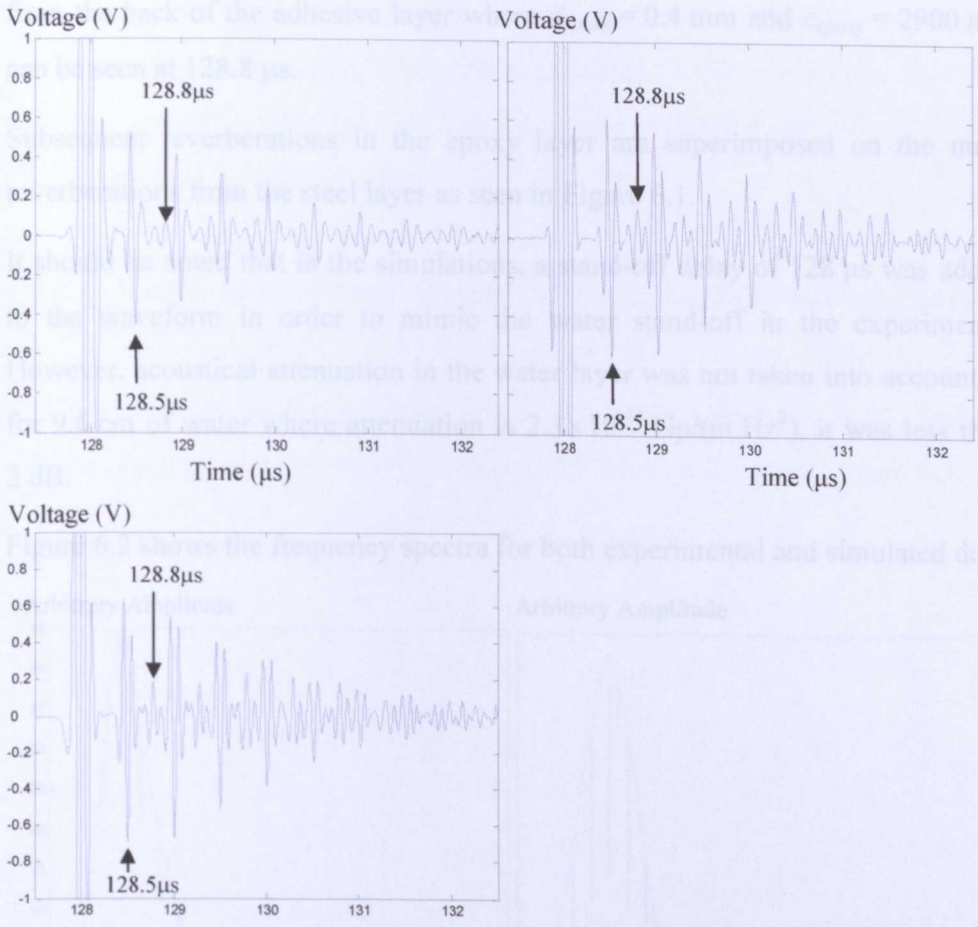

Figure 6.1. Received PE response for an adhesive lap joint bond specimen (1.5 mm steel plates with a 0.4 mm epoxy layer in between) at 10 MHz, from experiment (top left) and from simulation (impedance model and FE model) (top right and bottom left respectively)

The time interval between reverberations occurring in a layer of material when sending ultrasound in PE mode is:

$$\Delta t = \frac{2d}{c} \tag{6-7}$$

where c is the speed of sound.

In the case of the adhesive lap-joint bond specimen of Chapter 3, the main reverberations occur in the upper steel plate where d_{steel} = 1.5 mm and c_{steel} = 5900 m/s, hence Δt = 0.5 μs. This is indeed the time interval found between reverberations in Figure 6.1.

The front wall echo occurs at 128 μs — the time for the signal to travel in water between the transducer and the specimen that are 9.6 cm apart, and the back wall echo from the upper steel plate occurs 0.5 μs later at 128.5 μs. The echo coming

from the back of the adhesive layer where $d_{epoxy} = 0.4$ mm and $c_{epoxy} = 2900$ m/s can be seen at 128.8 μs.

Subsequent reverberations in the epoxy layer are superimposed on the main reverberations from the steel layer as seen in Figure 6.1.

It should be noted that in the simulations, a stand-off delay of 128 μs was added to the waveform in order to mimic the water stand-off in the experiments. However, acoustical attenuation in the water layer was not taken into account as for 9.6 cm of water where attenuation is 2.3×10^{-14} Np/(m.Hz^2), it was less than 2 dB.

Figure 6.2 shows the frequency spectra for both experimental and simulated data.

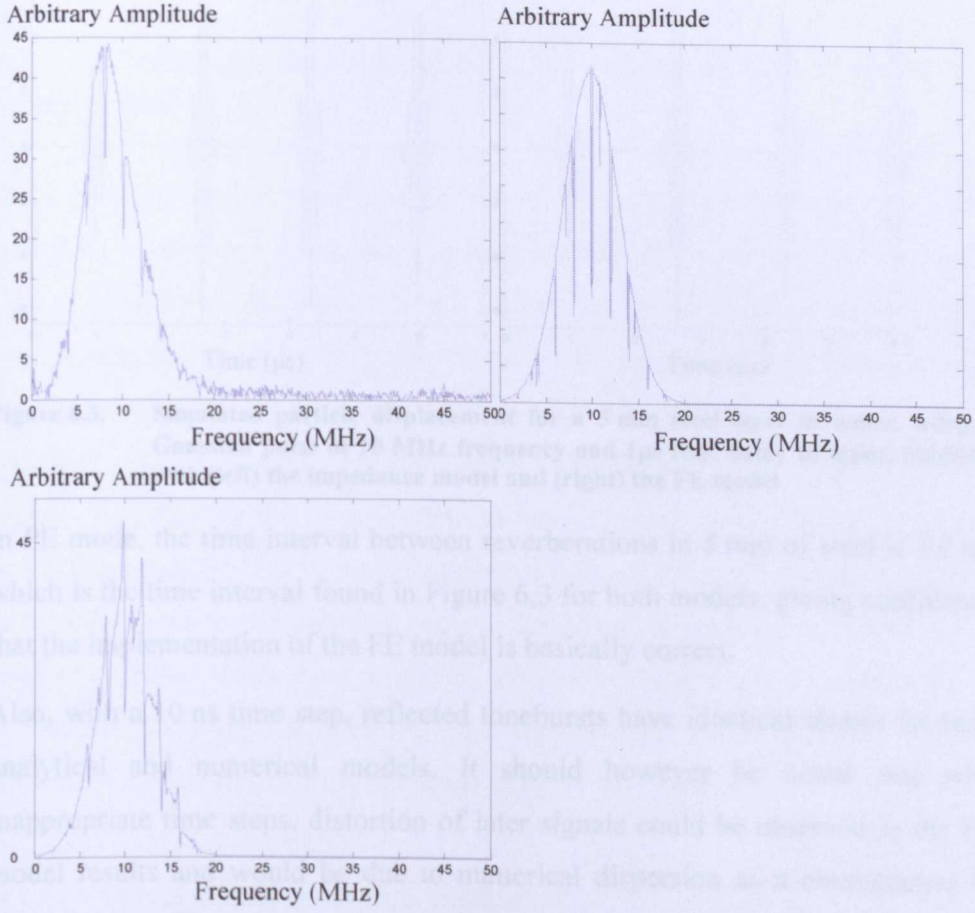

Figure 6.2. Frequency spectra of received PE response for an adhesive lap joint bond specimen (1.5 mm steel plates with a 0.4 mm epoxy layer in between) at 10 MHz, from experiment (top left) and simulation (impedance model and FE model) (top right and bottom left respectively)

In both experimental and simulated data, the troughs occur at the same frequencies (or very close). With the exception of noise in the former (arising

from equipment electronics), which was not modelled in the simulations, the models are in good agreement with the experiment. The loss in amplitude of the spectrum envelope obtained for the FE model might be an effect of poor discretisation in frequency domain.

6.2.3 Verification of finite element model against input impedance model

The simulated mechanical displacement for propagation through a single layer of steel (5 mm thickness) immersed in water in PE mode is shown in Figure 6.3.

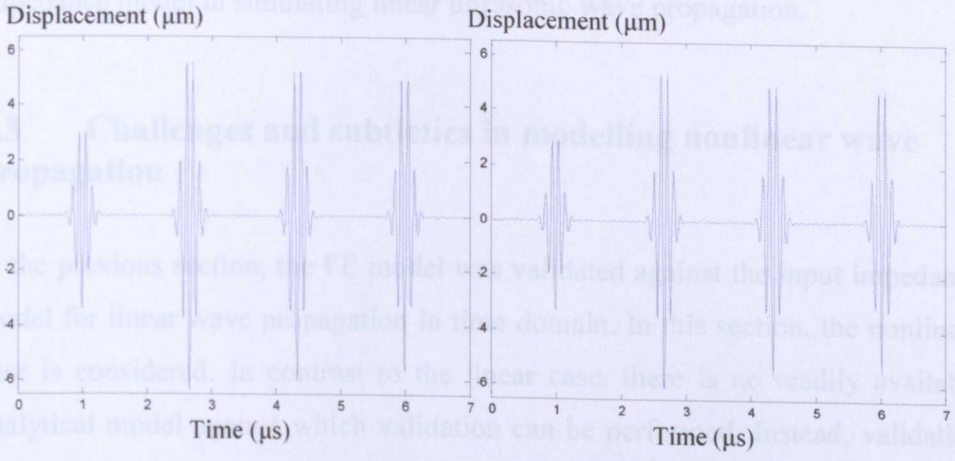

Figure 6.3. Simulated particle displacement for a 5 mm steel layer in water, using a Gaussian pulse of 10 MHz frequency and 1μs time delay as input, obtained with (left) the impedance model and (right) the FE model

In PE mode, the time interval between reverberations in 5 mm of steel is 1.7 μs, which is the time interval found in Figure 6.3 for both models, giving confidence that the implementation of the FE model is basically correct.

Also, with a 10 ns time step, reflected tonebursts have identical shapes for both analytical and numerical models. It should however be noted that with inappropriate time steps, distortion of later signals could be observed in the FE model results and would be due to numerical dispersion as a consequence of discretisation. The velocity of waves is not exactly constant with frequency as it should be, resulting in a gradual accumulation of phase error the further the wave propagates. Work described later will involve refining the mesh to insure this error stays at an acceptable level in all cases. The impedance model, on the other

hand, is an exact solution to the 1-D wave equation that implicitly includes the phase shift required for the boundary conditions at each interface to be satisfied.

The first signal is the displacement of the single wave propagating away from the top surface into the steel when the force is applied. The signal associated with the first reflection is twice the first signal amplitude because it is due to the displacements of two waves – the one coming towards the measurement point that has been reflected from the steel-water interface and the reflection of this wave going away from the measurement point back into the steel.

The above results provide confidence that the FE model is equivalent to the input impedance model in simulating linear ultrasonic wave propagation.

6.3 Challenges and subtleties in modelling nonlinear wave propagation

In the previous section, the FE model was validated against the input impedance model for linear wave propagation in time domain. In this section, the nonlinear case is considered. In contrast to the linear case, there is no readily available analytical model against which validation can be performed. Instead, validation for nonlinear wave propagation will be assumed to have been achieved if the specified material nonlinearity parameter β can be recovered from the model output. To extract β, the model output (a time-domain signal) will be processed in the frequency domain in the same way as a signal obtained experimentally. In order to be able to theoretically recover the absolute value of β (rather than a relative β value) from such a signal, several scalings must be performed to compensate for effects such as the finite length of the input toneburst. Specific choices of parameters will also be made to optimise its accuracy.

6.3.1 Signal post-processing method

In the FE model, time $t = 0$ corresponds to the start of the input signal. The model output is a time-domain signal $u_{out}(t)$ that represents particle displacement at the other end of the specimen in the case of through-transmission (TT). A

single layer of material with thickness d and sound velocity c is considered here to describe how the model output was processed to extract β.

First, a portion of the transmitted raw signal $u_{out}(t)$ is cut for analysis at $t_{start} = d/c$ and $t_{end} = d/c + T_w$ where T_w is the time window length that covers at least the first transmitted toneburst:

$$T_w = T_{tb} + T_{cut} \tag{6-8}$$

where T_{tb} is the toneburst duration and T_{cut} is an additional duration to enable a larger portion of the raw signal to be analysed.

T_{cut} is defined as a fraction of T_{tb}:

$$T_{cut} = f_{cut}\, T_{tb} \tag{6-9}$$

where $f_{cut} \geq 0$ is the cut factor as seen in Figure 6.4. The choice of f_{cut} will be discussed in a later section (7.7).

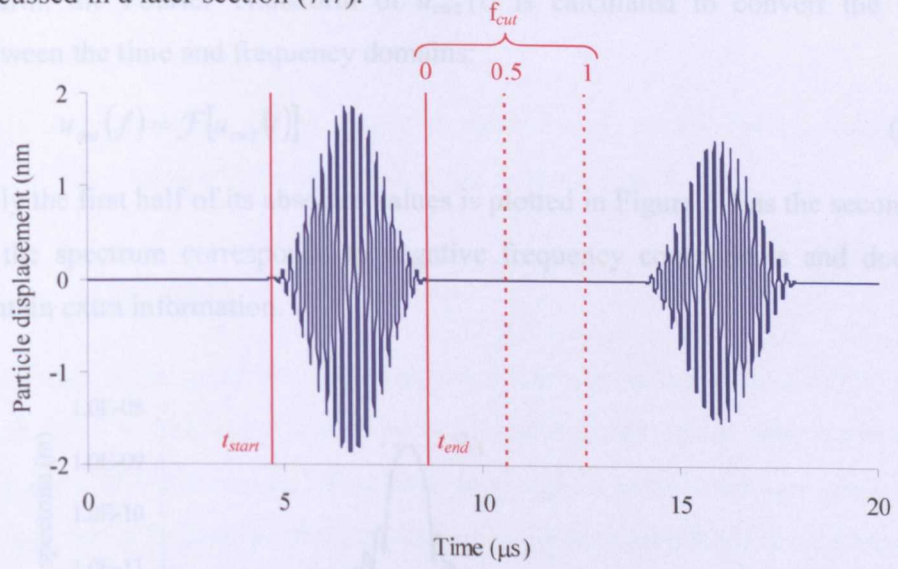

Figure 6.4. Model output raw signal $u_{out}(t)$ transmitted through 30 mm of aluminium at 5 MHz with examples of where it can be cut depending on the cut factor f_{cut}

Second, the cut signal obtained $u_c(t)$ is multiplied by a window function $w(t)$ whose choice will also be discussed in a later section (7.8):

$$u_{cw}(t) = u_c(t)\, w(t) \tag{6-10}$$

Third, it is zero-padded up to n_f points to provide the required resolution in the frequency spectrum. The resulting signal $u_{cwz}(t)$ containing the first transmitted toneburst only can be seen in Figure 6.5.

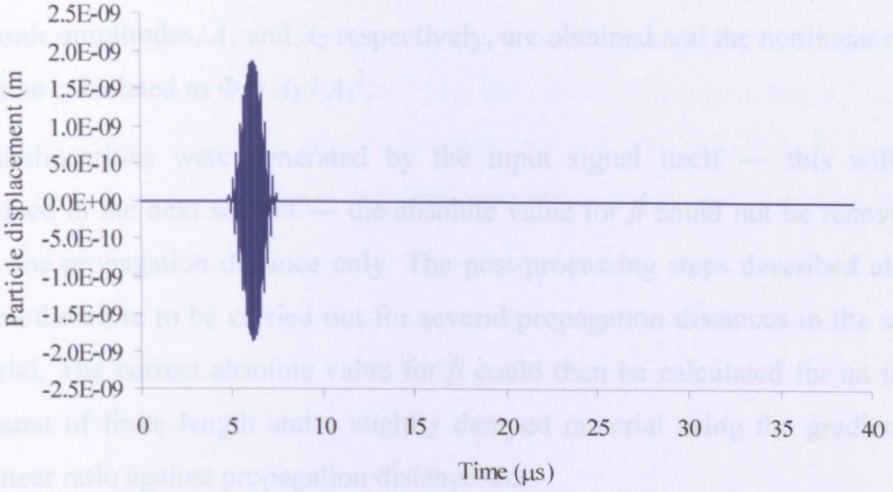

Figure 6.5. Output signal containing only the first transmitted toneburst transmitted through 30 mm of aluminium at 5 MHz

Fourth, the Fourier Transform of $u_{cwz}(t)$ is calculated to convert the signal between the time and frequency domains:

$$u_{out}(f) = \mathcal{F}[u_{cwz}(t)] \tag{6-11}$$

Only the first half of its absolute values is plotted in Figure 6.6 as the second half of the spectrum corresponds to negative frequency components and does not contain extra information.

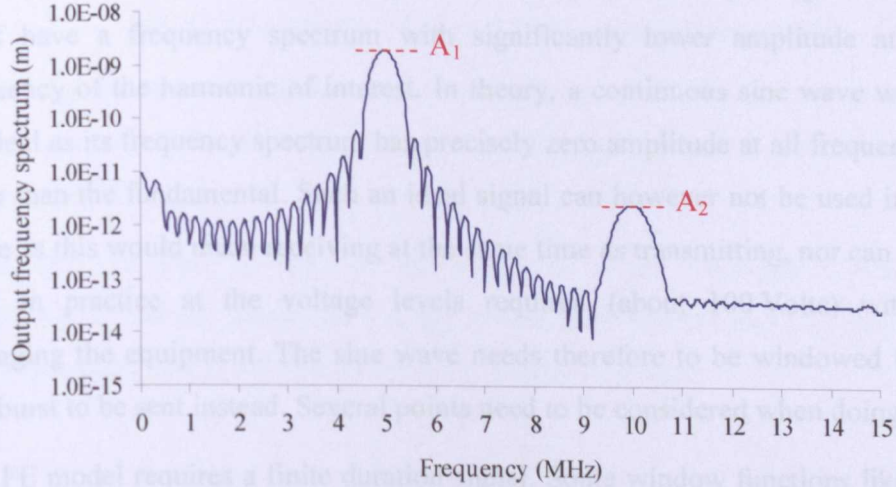

Figure 6.6. Frequency spectrum of the transmitted toneburst plotted in Figure 6.5

Finally, from this frequency spectrum, the fundamental frequency and 2nd harmonic amplitudes, A_1 and A_2 respectively, are obtained and the nonlinear ratio Φ can be calculated as $\Phi = A_2 / A_1^2$.

As nonlinearities were generated by the input signal itself — this will be explained in the next section — the absolute value for β could not be recovered from one propagation distance only. The post-processing steps described above needed therefore to be carried out for several propagation distances in the same material. The correct absolute value for β could then be calculated for an input toneburst of finite length and a slightly damped material using the gradient of nonlinear ratio against propagation distance Φ/x:

$$\beta = \frac{r_w r_d}{r_s} \frac{8}{k^2} \frac{\Phi}{x} \tag{6-12}$$

where r_w is the window ratio, r_d is the damping factor, r_s is the FFT scaling factor and k is the wavenumber.

These scaling factors are necessary to recover the correct absolute value for β and will be explained in more detail in the following sections.

6.3.2 Input signal

The input signal used for detecting nonlinearities in the output signal should itself have a frequency spectrum with significantly lower amplitude at the frequency of the harmonic of interest. In theory, a continuous sine wave would be ideal as its frequency spectrum has precisely zero amplitude at all frequencies other than the fundamental. Such an ideal signal can however not be used in PE mode as this would mean receiving at the same time as transmitting, nor can it be used in practice at the voltage levels required (about 100 Volts) without damaging the equipment. The sine wave needs therefore to be windowed for a toneburst to be sent instead. Several points need to be considered when doing so.

The FE model requires a finite duration signal. Some window functions like the Gaussian window however only tend asymptotically to zero and will therefore be truncated $T_{tb}/2$ either side of their peak. This truncation is performed symmetrically with respect to the ordinate to avoid problems with direct current

(DC) offset. Such problems include a shifting effect with time that makes signal processing difficult. In effect, if the input signal integral is not null, the nodes will be pushed more in one direction than the other. This means that instead of oscillating back and forth around their initial position, they will over time move away from it. Finally, this truncation introduces sidelobes in the signal's frequency spectrum.

To compare the level of sidelobes introduced in the frequency spectrum when applying a window, seven types of windows were chosen. Their time-domain implementation is plotted in Figure 6.7.

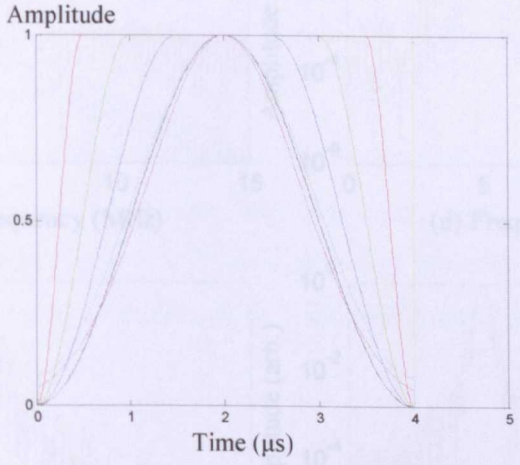

Figure 6.7. **Time-domain implementation of seven different windows: Rectangular (yellow), Gaussian (magenta), Hamming (cyan), Tukey r = 0.25 (red), Tukey r = 0.5 (green), Tukey r = 0.75 (blue) and Hanning (black)**

A Rectangular window is equivalent to no window at all. Tukey windows are cosine-tapered windows where r is the ratio of taper to constant sections and is between 0 and 1.

These different types of windows are compared in the frequency domain in Figure 6.8 to find out which one has the lowest level of sidelobes and therefore gives the most chances for harmonics in the output to be seen.

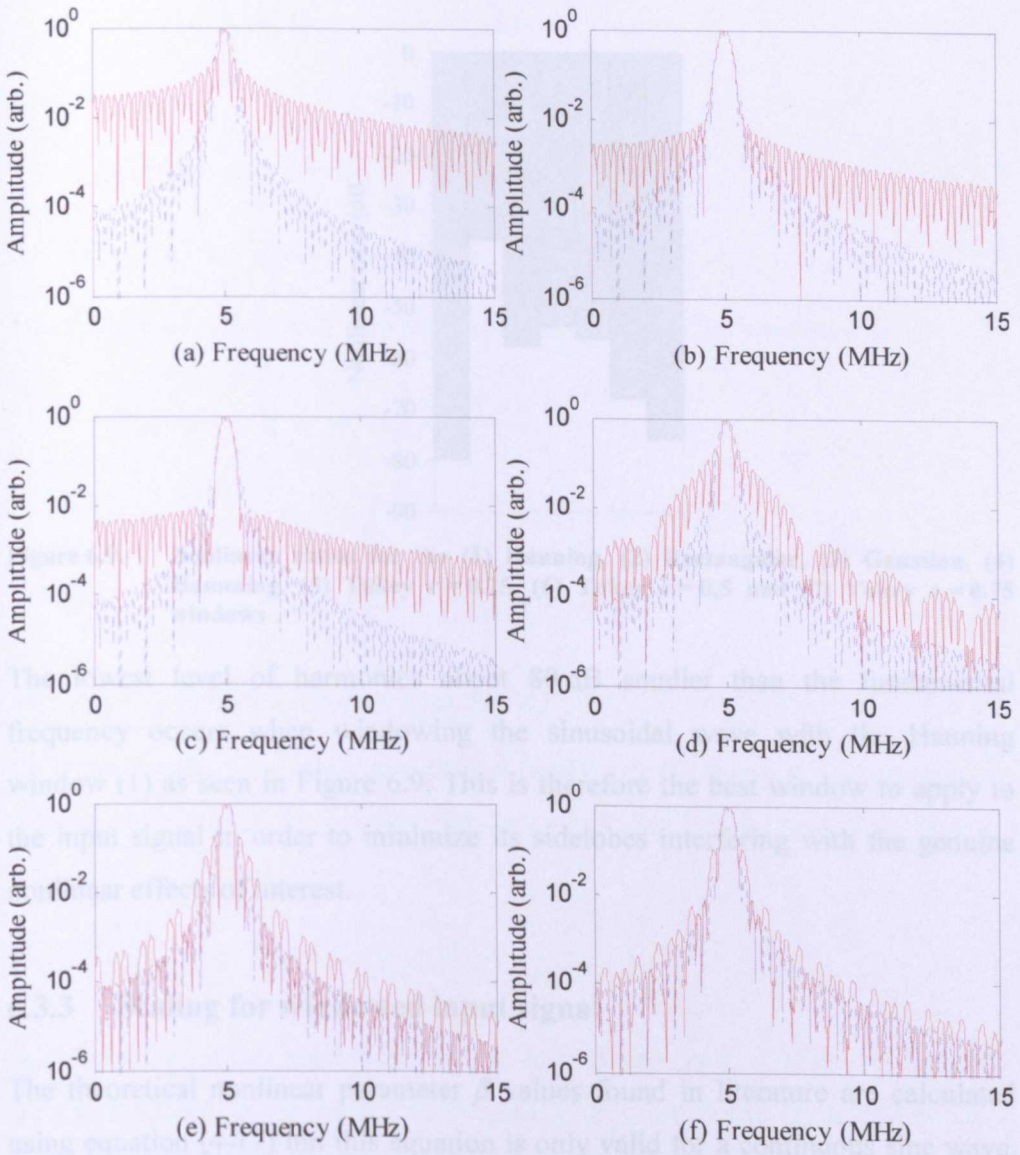

Figure 6.8. **Effect of windowing on size of sidelobes in the frequency spectrum of sinusoidal waves windowed with (a) Rectangular, (b) Gaussian (truncation of the Gaussian window 97 dB relative to the peak), (c) Hamming, (d) Tukey r = 0.25, (e) Tukey r = 0.5 and (f) Tukey r = 0.75 windows (red solid lines) in comparison with the Hanning window (blue dotted line) for a 4 μs toneburst (20 cycles at 5 MHz) and 8192 pts**

Taking the amplitudes A_1 and A_2 in the frequency spectra of Figure 6.8, the nonlinear ratios Φ are calculated for each window applied and plotted in Figure 6.9.

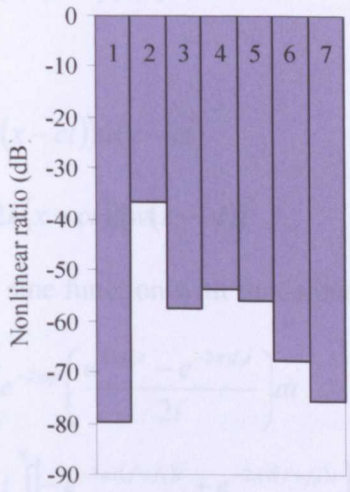

Figure 6.9. Nonlinear ratios for the (1) Hanning, (2) Rectangular, (3) Gaussian, (4) Hamming, (5) Tukey r = 0.25, (6) Tukey r = 0.5 and (7) Tukey r = 0.75 windows

The lowest level of harmonics about 80 dB smaller than the fundamental frequency occurs when windowing the sinusoidal wave with the Hanning window (1) as seen in Figure 6.9. This is therefore the best window to apply to the input signal in order to minimize its sidelobes interfering with the genuine nonlinear effects of interest.

6.3.3 Scaling for windowed input signal

The theoretical nonlinear parameter β values found in literature are calculated using equation (4-17) but this equation is only valid for a continuous sine wave, not a toneburst. Another correction factor, the window ratio r_w, needs therefore to be calculated from the frequency spectrum of the window used in order to recover the theoretical value for the nonlinear parameter.

As seen in Chapter 4, when the external acoustic pressure P_{ext} is a continuous sinusoidal wave, the approximate solution to the nonlinear wave equation is:

$$u(x,t) = \underbrace{\frac{1}{8}\beta k^2 A_1^2 x}_{A_0} + A_1 \sin(-k(x-ct)) - \underbrace{\frac{1}{8}\beta k^2 A_1^2 x}_{A_2} \sin(-2k(x-ct)) + \ldots \quad (4\text{-}16)$$

where A_0 is the DC amplitude.

However, when applying a window w to the input continuous sinusoidal wave, the solution to the nonlinear wave equation (4-13) is of the form:

$$u(x,t) = u_0(x) + u_1(x,t) + u_2(x,t) + \ldots \tag{6-13}$$

where

$$u_1(x,t) = A_1 \sin(-k(x-ct))w(x-ct) \tag{6-14}$$

$$u_2(x,t) = A_2 \sin(-2k(x-ct))(w(x-ct))^2 \tag{6-15}$$

The Fourier transform of a sine function with fundamental frequency f_0 is:

$$\begin{aligned}\mathcal{F}[\sin(2\pi f_0 t)] &= \int_{-\infty}^{\infty} e^{-2\pi i f t}\left(\frac{e^{2\pi i f_0 t} - e^{-2\pi i f_0 t}}{2i}\right)dt \\ &= \frac{1}{2}i\int_{-\infty}^{\infty}\left[-e^{-2\pi i(f-f_0)t} + e^{-2\pi i(f+f_0)t}\right]dt \\ &= \frac{1}{2}i[\delta(f+f_0) - \delta(f-f_0)]\end{aligned} \tag{6-16}$$

where $\delta(h)$ is the delta function such that $\delta(h) = 1$ if $h = 0$ and $\delta(h) = 0$ otherwise.

So if the Fourier transforms of $w(t)$ and $(w(t))^2$ are $W_1(f)$ and $W_2(f)$ respectively, then looking only at the positive frequency half, the Fourier transform of $u(x,t)$ is:

$$|U(x,f)| = \frac{A_1}{2}W_1(f-f_0) + \frac{A_2}{2}W_2(f-2f_0) \tag{6-17}$$

In other words, it is a peak at the fundamental frequency f_0 of shape W_1 scaled by $A_1/2$ and a peak at the harmonic frequency, $2f_0$, of shape W_2 scaled by $A_2/2$. Therefore the peaks at f_0 and $2f_0$ in the frequency domain have amplitudes:

$$A_1' = \frac{A_1}{2}W_1(0) \tag{6-18}$$

$$A_2' = \frac{A_2}{2}W_2(0) \tag{6-19}$$

and the theoretical nonlinear ratio is recovered by:

$$\Phi = \frac{A_2}{A_1^2} = \frac{A_2'}{A_1'^2}\frac{W_1(0)^2}{2W_2(0)} \tag{6-20}$$

The correction term, called the window ratio r_w, is based on the zero frequency components of the Fourier transforms of the envelope function and its square:

$$r_w = \frac{W_1(0)^2}{2W_2(0)} \tag{6-21}$$

When using the Hanning window as recommended in section 6.3.2, the window ratio r_w will vary between 1.32 and 1.34 when changing the number of points per wavelength, the number of cycles and the number of points in the signal.

6.3.4 Scaling for damping

If attenuation is accounted for in the model, then the nonlinear parameter obtained has to be multiplied by a correction factor, the damping factor r_d [147]:

$$r_d = \left(\sum_{n=1}^{\infty} \frac{(-2\alpha x)^{n-1}}{n!} \right)^{-1} \tag{6-22}$$

where α is the attenuation coefficient in Np/(m.Hz).

It was found that for a lightly damped ultrasonic wave, adjusted nonlinear ratio values converged if n was greater than 50 as seen in Figure 6.10.

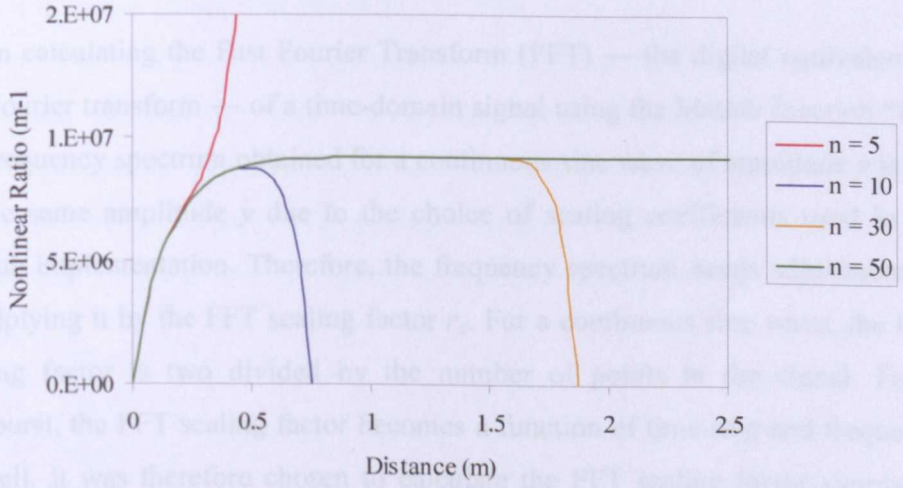

Figure 6.10. Nonlinear ratio for a lightly damped ultrasonic wave travelling in aluminium at 5 MHz

Damping factors for $n = 50$ as plotted in Figure 6.11 were therefore used to adjust the output nonlinear parameter found when taking into account material attenuation in the model.

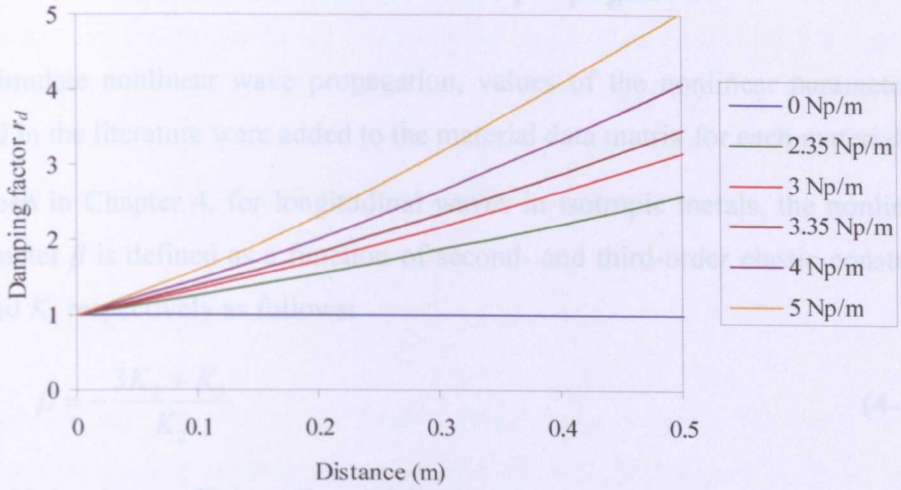

Figure 6.11. Damping factor for $n = 50$ for materials with different attenuation coefficients

At 5 MHz, aluminium has a 3.35 Np/m attenuation coefficient [77] and the damping factor varies from 1 to 1.8 for propagation distances up to 20 cm.

6.3.5 Scaling for Fast Fourier Transform

When calculating the Fast Fourier Transform (FFT) — the digital equivalent of the Fourier transform — of a time-domain signal using the Matlab function "fft", the frequency spectrum obtained for a continuous sine wave of amplitude y is not of the same amplitude y due to the choice of scaling coefficients used in the Matlab implementation. Therefore, the frequency spectrum needs adjustment by multiplying it by the FFT scaling factor r_s. For a continuous sine wave, the FFT scaling factor is two divided by the number of points in the signal. For a toneburst, the FFT scaling factor becomes a function of time step and frequency as well. It was therefore chosen to calculate the FFT scaling factor simply by taking the ratio of the time-domain signal amplitude by its frequency spectrum amplitude:

$$r_s = \frac{\max(u(t))}{\max(abs(fft\,(u(t))))} \tag{6-23}$$

6.4 Validation for nonlinear wave propagation

To simulate nonlinear wave propagation, values of the nonlinear parameter β found in the literature were added to the material data matrix for each material.

As seen in Chapter 4, for longitudinal waves in isotropic metals, the nonlinear parameter β is defined as a function of second- and third-order elastic constants K_2 and K_3 respectively as follows:

$$\beta = -\frac{3K_2 + K_3}{K_2} \tag{4-14}$$

The third-order coefficient K_3 used in the algorithm was therefore calculated from β according to:

$$K_3 = -(\beta + 3)K_2 \tag{6-24}$$

As mentioned previously, a way to validate the model for nonlinear wave propagation is to extract from the output the same nonlinear parameter β as the one entered in the model.

To this end, the model was run with a 5 MHz input signal for a 25 mm single layer of aluminium. The element size was 43 μm, the time step was 4.8 ns and the number of points was 8192. The choice of these parameters will be explained in the next chapter. Nonlinear ratios were calculated from the frequency spectra of the model output signals at propagation distances from 1 to 10 mm with 1 mm increments. They were plotted against propagation distance in Figure 6.12.

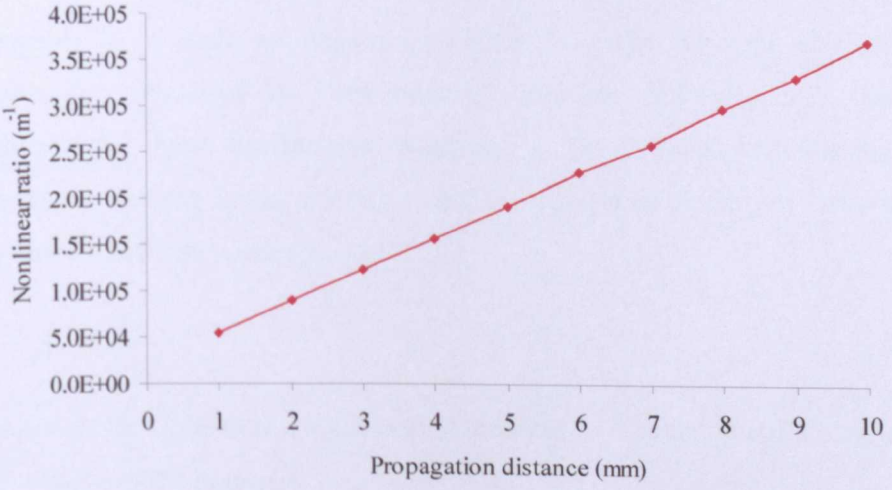

Figure 6.12. Nonlinear ratio vs. propagation distance in aluminium at 5 MHz

From the gradient of the curve in Figure 6.12, the extracted nonlinear parameter calculated using equation (6-12) was found to be 15.74 compared with a value of 16 entered in the model. The 1.6 % error is believed to be due to numerical dispersion as a consequence of discretisation. The model was therefore deemed to be validated for nonlinear wave propagation.

6.5 Conclusion

In this chapter, the FE model was validated and verified for linear wave propagation against experimental data and an analytical model with an input impedance approach based on transmission line theory respectively. For nonlinear wave propagation, a few important points needed first to be addressed such as input signal windowing, damping and Fourier transform functions. The model could then be run and the output data was processed in the frequency domain. The nonlinear parameter β was recovered which implied that the model was basically correct.

In the following chapter, modelling rules and recommendations for TT are given.

Chapter 7

Modelling rules for the one-dimensional finite element model

7.1 Introduction

In the previous chapter, the finite element (FE) model was first validated in the linear regime against experimental data and verified against an input impedance model. Material nonlinearity was then introduced and the model was validated for nonlinear wave propagation by recovering the specified material nonlinearity parameter β from the model output. Subtleties such as the scalings that must be performed were explained.

In this chapter, for the user to run the model for any structure (single or multi-layered) at any driving frequency in through-transmission (TT), modelling rules are set by generalised equations with dimensionless factors. Recommendations on the choice of factors are then given accordingly.

7.2 Element size and time step

In the author's implementation of the FE model in Matlab, each point corresponds to a node as drawn in Figure 7.1. The element size Δx_i is automatically calculated for each material with the following user defined parameters: the signal fundamental frequency f_0, the material under inspection which determines the sound velocity c_i and the number of points per wavelength at the fundamental frequency n_λ, as:

$$\Delta x_i = \frac{\lambda_i}{n_\lambda} \tag{7-1}$$

where $\lambda_i = c_i / f_0$ is the wavelength at the fundamental frequency and i is an index representative of the material.

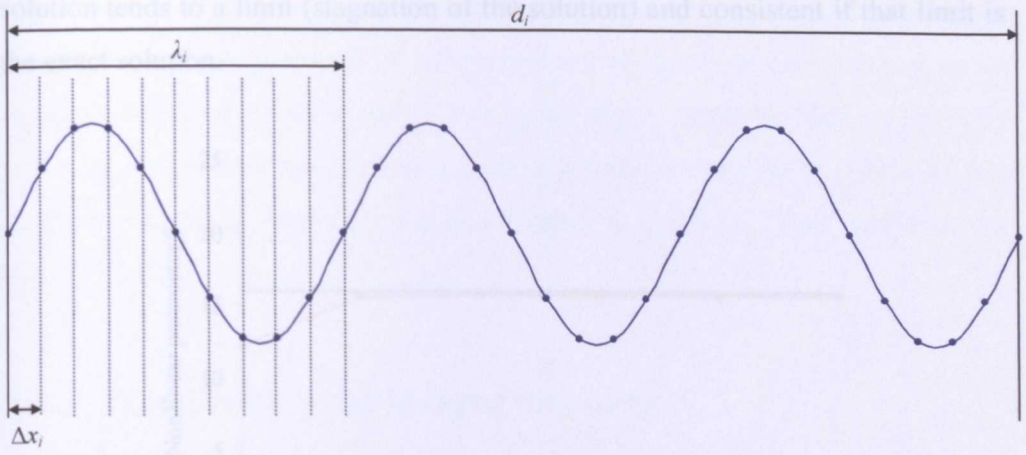

Figure 7.1. Schematic of a sine wave travelling in a layer of material of thickness d_i where $n_\lambda = 10$.

The time step Δt is calculated with respect to the element size. When applying the Fourier (or von Neumann) stability analysis [146], it is found that the time step Δt should be smaller than the time required for sound to travel across the element length such that:

$$\Delta t \leq \frac{\Delta x}{c} \tag{7-2}$$

In other words, $\Delta t = \mathrm{f}_{\Delta t} \min\left(\frac{\Delta x_i}{c_i}\right)$ such that $\mathrm{f}_{\Delta t} \leq \frac{\sqrt{2}}{2}$ where $\mathrm{f}_{\Delta t}$ is the time step factor and $\frac{\sqrt{2}}{2}$ is a safety factor.

The time step factor $\mathrm{f}_{\Delta t}$ was chosen to be $\frac{\sqrt{2}}{2}$ in order for the model to be stable while keeping its running time to a minimum as a smaller time step will increase the running time.

However, when generating a toneburst of duration $T_{tb} = n_c / f_0$ where n_c is the number of cycles per toneburst, it is also required that T_{tb} is an integer multiple of Δt to guarantee that its integral is null (see section 6.3.2). This can be achieved if the sampling frequency $f_s = 1 / \Delta t$ is an integer multiple of f_0.

Convergence is an essential condition for any numerical scheme and is ensured if the model is stable and consistent. The numerical model is stable when the

solution tends to a limit (stagnation of the solution) and consistent if that limit is the exact solution.

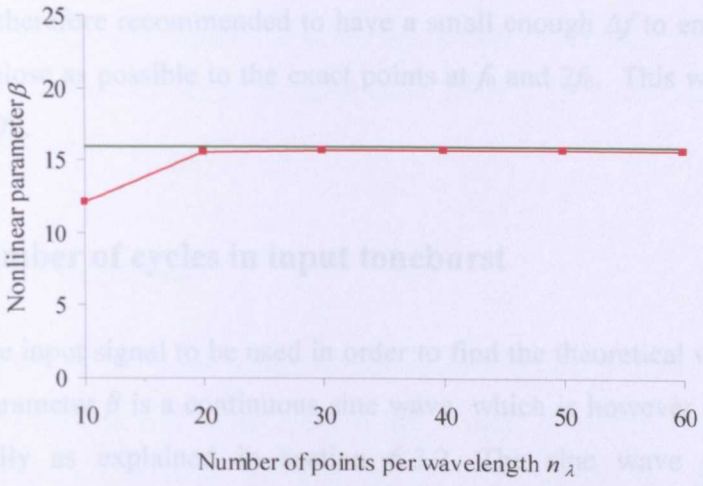

Figure 7.2. Nonlinear parameter β obtained when running the model in aluminium at 5 MHz for different numbers of points per wavelength (at 5 MHz) compared with its theoretical value

It can be seen from Figure 7.2 that from 30 points per wavelength, the nonlinear parameter obtained tends towards its theoretical value.

7.3 Frequency step

For the toneburst duration to be an integer multiple of the time step Δt as mentioned in the previous section, the sampling frequency f_s which is the inverse of Δt should be an integer multiple of the fundamental frequency f_0. f_s should therefore be rounded up to the next multiple of f_0, and Δt recalculated by taking the reciprocal of f_s.

Also, to optimise Fast Fourier Transform (FFT) operations which are most efficient when the array length is an exact power of two, the time-domain signals should be padded with zeros for their number of points to reach the nearest integer power of two n_f.

The frequency step Δf is calculated by dividing f_s by n_f:

$$\Delta f = \frac{f_s}{n_f} = \frac{1}{n_f \Delta t} \tag{7-3}$$

In an ideal case, for the β calculation, there should be points in the frequency spectrum at exactly f_0 and $2f_0$. It is however not always possible to have f_0 as an integer multiple of Δf while still following the above recommendations about Δt and n_f. It is therefore recommended to have a small enough Δf to enable A_1 and A_2 to be as close as possible to the exact points at f_0 and $2f_0$. This was achieved with $n_f = 8192$.

7.4 Number of cycles in input toneburst

In theory, the input signal to be used in order to find the theoretical values of the nonlinear parameter β is a continuous sine wave, which is however not possible experimentally as explained in section 6.3.2. The sine wave is therefore windowed with a Hanning window shown to give the lowest level of side lobes when truncated at times 0 and T_{tb}, the toneburst duration calculated from the chosen number of cycles per toneburst n_c.

A higher n_c will reduce the sideband level at the second harmonic frequency but may also lead to practical problems such as transducer overheating and in some cases, difficult signal post-processing. At 20 cycles, the sideband level is already at -80 dB which is typically sufficient to detect the nonlinear ratios of interest.

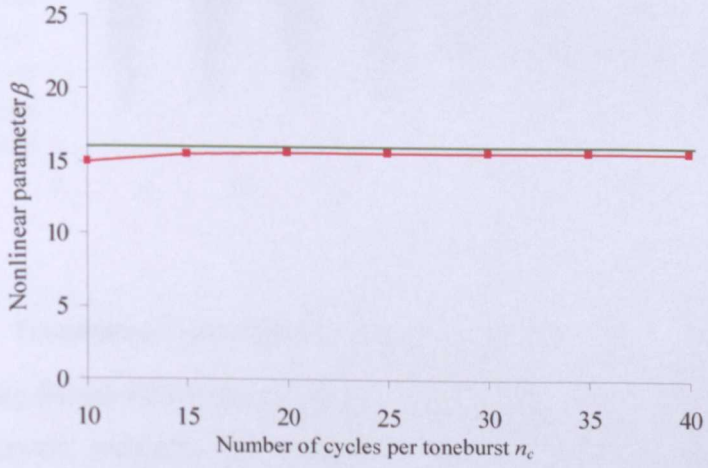

Figure 7.3. Effect of the number of cycles in input toneburst on the model's accuracy for TT in a single layer of aluminium

However as the specimen thickness is reduced, n_c could in some cases be reduced for the complete transmitted toneburst to still be isolated from subsequent reverberations. When sending a 5 MHz ultrasonic wave in TT in a

single layer of aluminium, 15 cycles is still adequate to recover the nonlinear parameter as seen in Figure 7.3.

For thinner specimens where it is not possible to have such separation between transmitted and reflected signals, it is recommended to increase the number of cycles to 20 to improve signal-to-noise ratio (SNR). In such cases, it is not possible to recover the absolute value of β.

7.5 Input amplitude

Sufficient power in the input signal — the external acoustic pressure P_{ext} — is required for nonlinearities to be seen in the output. However, if the external acoustic pressure's amplitude A_{ap} was too high, the signal was distorted and shifting was found to occur as a result (Figure 7.4). It should be noted that this effect was always there but just not visible if the input amplitude was lower.

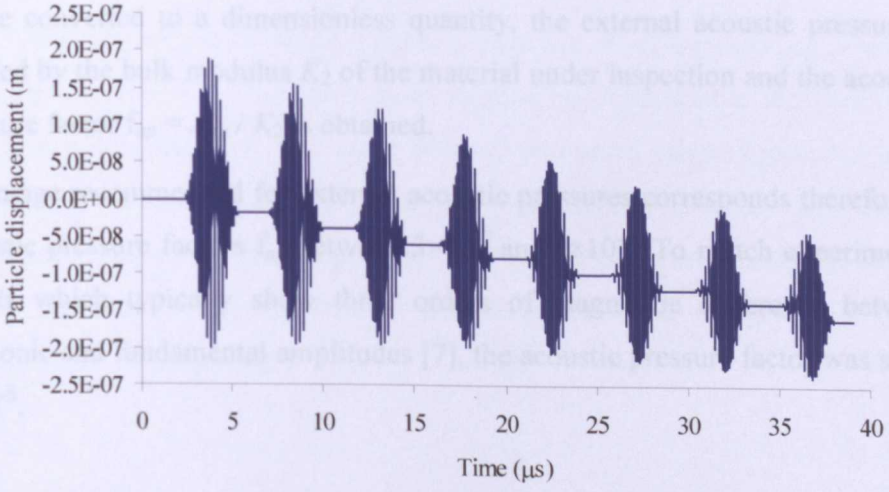

Figure 7.4. Transmitted 5 MHz signal in 15 mm aluminium

When running the model for aluminium at 5 MHz, it was found that from 1 MPa external acoustic pressure, the extracted nonlinear parameter β converged towards its theoretical value (Figure 7.5).

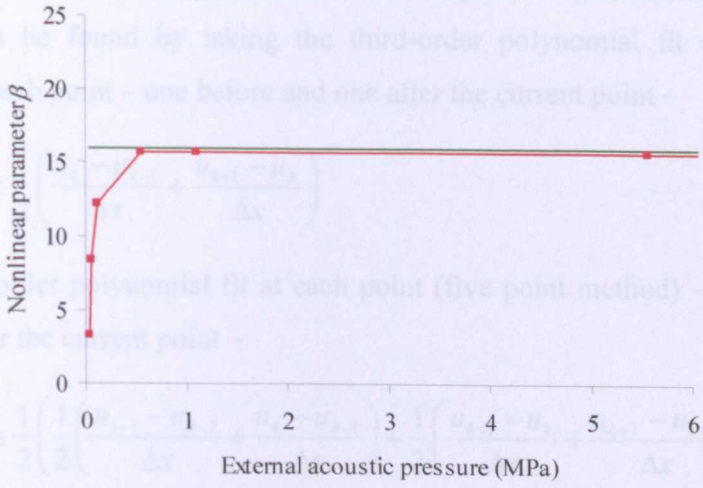

Figure 7.5. Effect of input acoustic pressure on model's accuracy

However although β stayed within the 1.6 % error margin for any $A_{ap} \geq 1$ MPa, shifting was occurring within the signal and made data analysis difficult from $A_{ap} \geq 10$ MPa as the cutting operation then effectively put a step into the signal.

To be converted to a dimensionless quantity, the external acoustic pressure is divided by the bulk modulus K_2 of the material under inspection and the acoustic pressure factor $f_{ap} = A_{ap} / K_2$ is obtained.

The range recommended for external acoustic pressures corresponds therefore to acoustic pressure factors f_{ap} between 3×10^{-7} and 1×10^{-4}. To match experimental results which typically show three orders of magnitude difference between harmonic and fundamental amplitudes [7], the acoustic pressure factor was set to 1×10^{-5}.

7.6 Gradient function

In the equation for the algorithm defined in section 5.2, the nonlinear matrix K_{NL} includes the calculation of a gradient $\frac{\partial u}{\partial x}$:

$$\mathbf{K}_{NL} = (3K_2 + K_3)\frac{A}{\Delta x}\frac{\partial u}{\partial x} \tag{7-4}$$

where K_3 is the third-order elastic constant and A is the cross-sectional area.

It is the gradient of the displacement u with respect to spatial position x. This gradient can be found by taking the third-order polynomial fit (three point method) at each point – one before and one after the current point –

$$\frac{\partial u}{\partial x} \cong \frac{1}{2}\left(\frac{u_k - u_{k-1}}{\Delta x} + \frac{u_{k+1} - u_k}{\Delta x}\right) \tag{7-5}$$

or the fifth-order polynomial fit at each point (five point method) – two before and two after the current point –

$$\frac{\partial u}{\partial x} \cong \frac{1}{2}\left(\frac{1}{2}\left(\frac{u_{k-1} - u_{k-2}}{\Delta x} + \frac{u_k - u_{k-1}}{\Delta x}\right) + \frac{1}{2}\left(\frac{u_{k+1} - u_k}{\Delta x} + \frac{u_{k+2} - u_{k+1}}{\Delta x}\right)\right) \tag{7-6}$$

It should be noted that for end points or two points only, the gradient was calculated for both methods with respect to one neighbouring point only, e.g. at the first point:

$$\frac{\partial u}{\partial x} \cong \frac{u_{k+1} - u_k}{\Delta x} \tag{7-7}$$

The choice of gradient calculation method does not affect the ultimate measured nonlinear parameter β. The three point method requires double the number of sampling points than the five point method to ensure convergence but when running the model with both methods, no significant difference was found as convergence occurred from the same number of points per wavelength as seen in Figure 7.6. The three point method was therefore recommended as it had a slightly faster running time.

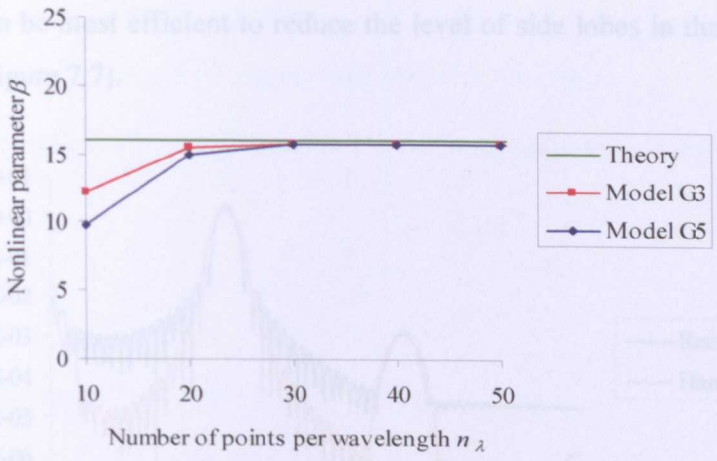

Figure 7.6. **Nonlinear parameter β obtained when running the model in aluminium at 5 MHz using the three and five point methods (G3 and G5 respectively) for different numbers of points per wavelength compared with its theoretical value**

7.7 Time window length

For TT in a single layer, it was found that the nonlinear parameter β extracted from the model tended towards its theoretical value when the fraction of signal cut for analysis T_w was minimum. It is therefore recommended to set the factor f_{cut} at zero when processing the data for TT in a single layer of material. It should however be noted that the absolute value for β can only be recovered if the processed signal does not include overlapping reverberations.

For multiple layers, it was explained and shown in Chapter 3 how looking at multiple reverberations could increase sensitivity by enhancing interfacial effects. This can be done when taking a larger section of the output signal for analysis and will be developed further in the next chapter.

7.8 Extraction window function

The model output signal $u_{out}(t)$ was cut to the portion of interest to obtain $u_c(t)$ which was then multiplied by a window function $w(t)$. This windowing was carried out to remove artefacts due to the offset issue where the zero levels on either side of the toneburst are slightly different. The Hanning window $w_{hann}(t)$

was found to be most efficient to reduce the level of side lobes in the frequency spectrum (Figure 7.7).

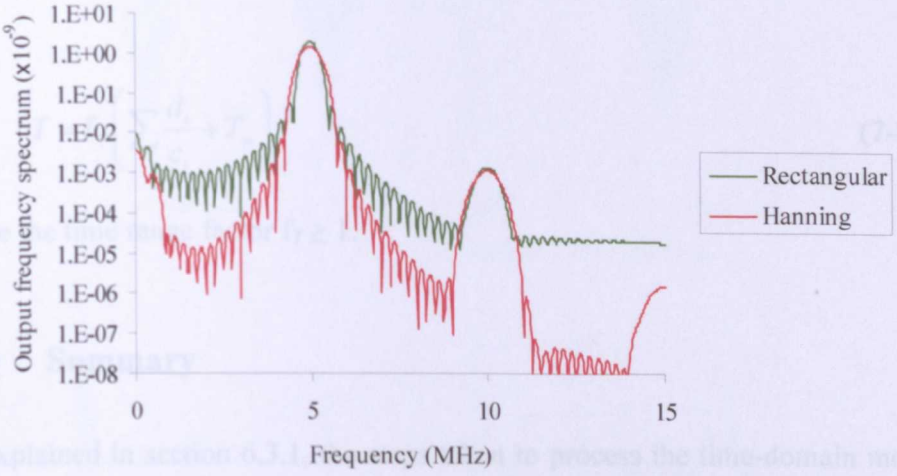

Figure 7.7. Frequency spectra of $u_{cut}(t)$ multiplied by a rectangular and a Hanning window

In effect, the offset observed in $u_{out}(t)$ corresponds to a sharp step in $u_c(t)$. This gives rise to some of the sidelobes that span the complete frequency range and interfere with the frequency peaks of interest. For this reason, $u_c(t)$ is multiplied by a smooth window to smear out the sharp step in the time domain and suppress the higher frequency sidelobes. There still is an artefact at the direct current (DC) offset but this does not interfere with the frequencies of interest anymore.

Using a smooth window, however, modifies the shape of the spectrum of interest as well as the absolute values of A_1 and A_2 — multiplication in the frequency domain is convolution in the time domain. When extracting β for model validation where the values need to stay true to their absolute values, no windowing was therefore carried out. This is the equivalent of applying a rectangular window $w_{rect}(t)$.

7.9 Time range

The time range T should either be set to the minimum time required for the model to output the section of signal chosen by the user, or to any longer period

of time desired. The minimum time in TT is the time taken for the directly-transmitted signal to propagate through all layers in the model.

For a specimen with i layers of material, the time range T was therefore defined as:

$$T = \mathrm{f_T}\left(\sum_i \frac{d_i}{c_i} + T_w\right) \tag{7-8}$$

where the time range factor $f_T \geq 1$.

7.10 Summary

As explained in section 6.3.1, the steps taken to process the time-domain model output signal $u_{out}(t)$ at different propagation distances were the following:

1. The signal was cut, windowed and zero-padded.

$$u_{cwz}(t) = u_{out}(t) \times w(t) \tag{7-9}$$

where $w(t) = \begin{cases} w_{hann}(t) \text{ for } t \in [t_{start}, t_{end}] \\ 0 \text{ for } t \in [0, t_{start}[\cup]t_{end}, n_f \Delta t] \end{cases}$

2. The obtained signal $u_{cwz}(t)$ was Fourier transformed to obtain $u_{out}(f)$ from which A_1 and A_2 were taken.

$$A_1 = |u_{out}(f_0)|, \; A_2 = |u_{out}(2f_0)| \tag{7-10}$$

and the nonlinear ratio Φ calculated:

$$\Phi = \frac{A_2}{A_1^2} \tag{7-11}$$

3. The nonlinear parameter β was calculated from the gradient Φ/x.

$$\beta = \frac{r_w r_d}{r_s} \frac{8}{k^2} \frac{\Phi}{x} \tag{7-12}$$

where r_s, r_w, and r_d are the scaling factors for the FFT, input signal windowing and damping respectively.

This process is shown in Figure 7.8.

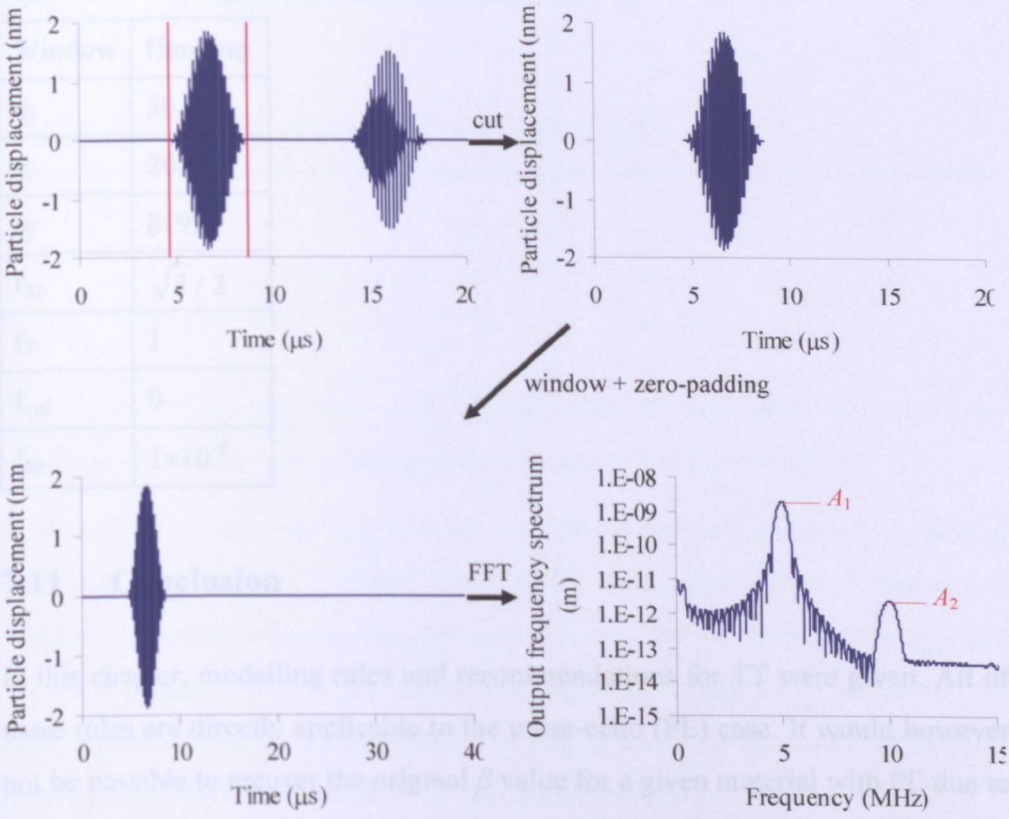

Figure 7.8. **Diagram of signal post-processing: raw model output signal $u_{out}(t)$ (upper left) from which the transmitted toneburst is extracted using a rectangular window (upper right) then zero-padded (lower left), and finally Fourier transformed to obtain a frequency spectrum (lower right)**

If the modelling rules summarised in Table 7.1 are adhered to, the model is acceptably accurate: for aluminium, β values in the range 15.53 to 15.74 will be determined to within -3%.

Table 7.1. **Modelling rules**

$\Delta t = f_{\Delta t} \frac{\Delta x}{c}$	such that	$f_{\Delta t} \leq \frac{\sqrt{2}}{2}$
$T = f_T \left(\sum_i \frac{d_i}{c_i} + T_{tb} + T_{cut} \right)$		$1 \leq f_T$
$T_{cut} = f_{cut} T_{tb}$		$0 \leq f_{cut}$
$A_{ap} = f_{ap} K_2$		$7 \times 10^{-6} < f_{ap} < 10^{-4}$

Modelling settings for model optimisation and accuracy in TT at 5 MHz are summarised in Table 7.2.

Table 7.2. Settings recommended for TT at 5 MHz

Window	Hanning
n_λ	30
n_c	20
n_f	8192
$f_{\Delta t}$	$\sqrt{2}/2$
f_T	1
f_{cut}	0
f_{ap}	1×10^{-5}

7.11 Conclusion

In this chapter, modelling rules and recommendations for TT were given. All of these rules are directly applicable to the pulse-echo (PE) case. It would however not be possible to recover the original β value for a given material with PE due to partial 'phase cancellation' occurring in the nonlinear signal when reflected back to the transducer. In a "perfect" 1-D set-up where there are no diffraction effects (beam spreading), no attenuation and a 100% reflection, the transmitted harmonic wave is suppressed by the reflected harmonic wave that has a 180° phase shift [148].

In the following chapter, the FE model is further developed by adding elements that simulate kissing bonds (KB), noise and external sources of nonlinearities. Experimental measurements will be used to find the variables required for these elements.

Chapter 8

Additional model elements

8.1 Introduction

In the previous chapter, rules and recommendations were given for modelling nonlinear ultrasonic wave propagation in through-transmission (TT).

In this chapter, the finite-element (FE) model is further developed by adding elements that simulate kissing bonds (KB), noise and external sources of nonlinearities. Experimental measurements are used to find the variables required for these elements. The model can then be run as a prediction tool (Chapter 9) to find out, for example, if the presence of KB in a typical aeronautical adhesive joint can be detected in immersion or in pulse-echo (PE).

8.2 Additional model elements

8.2.1 Simulation of a kissing bond

In order to simulate the presence of a KB between two materials such as an adherend and an adhesive, a very thin layer of the adhesive is selected to represent the 'KB layer'. For this case, it was chosen to consider the kissing bond as a massless spring where the 'KB layer' thickness d_{KB} has to be minimum such that $d_{KB} << \lambda$ where λ is the wavelength in the adhesive. On that basis, d_{KB} is therefore one element thick.

Its linear stiffness K_{LKB} is the interfacial stiffness per unit area of the contacting interface.

Its nonlinear stiffness K_{NLKB} is:

$$K_{NLKB} = -\beta_{KB} K_{LKB} \tag{8-1}$$

where β_{KB} is the KB nonlinear parameter which is not the same as the material nonlinear parameter β as defined in (4-14) where β is related to second and third order elastic constants.

The most common way KB behaviour is experimentally reproduced is by taking two contacting surfaces pressed together by an external pressure, enabling them to be in intimate mechanical contact without an actual bond ([6] [10][131][151][152]). A phenomenological contact model has been developed to establish the relationship between the external applied mechanical pressure and the resulting interfacial stiffness:

$$K_{LKB} = CP^m \tag{8-2}$$

where P is the external applied mechanical pressure, C and m are constants.

It should be noted that this model is built on the basis of asperities present on dissimilar surfaces which is a slightly different kind of interface than a kissing bond where both surfaces are perfectly matched.

8.2.2 Instrumentation noise

It was important to quantify the noise level generated by the electronic equipment in order to know the threshold above which nonlinearities might be seen.

In most measurement systems, the receiver amplifier is the main source of random electronic noise which can be modelled according to Figure 8.1.

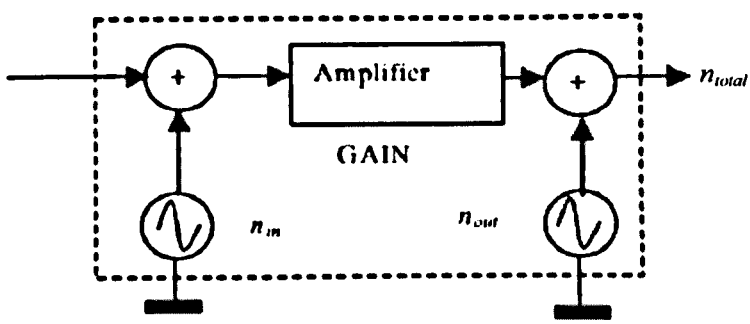

Figure 8.1. Schematic diagram of the noise model for a typical receiver amplifier [149]

The two noise sources contributing to the electronic device inherent noise are: the root-mean-squared (RMS) noise amplitude n_{out} which is independent of the

amplifier gain setting G and the RMS noise amplitude n_{in} which is an effective input component that is amplified. The noise processes are usually assumed to be zero mean Gaussian noise with a certain variance, the standard deviation squared σ^2. When two such processes are added together, it is the variances which add, hence the form of the following equation for the standard deviation or RMS amplitude of the net additive noise at the amplifier output:

$$n_{total} = \sqrt{(n_{in}G)^2 + n_{out}^2} \tag{8-3}$$

Equation (8-3) could be incorporated into the model by adding to the output signal normally distributed random numbers with a standard deviation of n_{total}. This would simulate noise as a function of receiver gain G and make the signal more realistic. But as amplifier noise is additive Gaussian noise, there is no need to physically add it to the FE model. The RMS noise level found by equation (8-3) was therefore used to draw a line and indicate its expected level in the final signal.

8.2.3 Nonlinearities from external sources

The general challenge associated with making reliable nonlinear measurements is the presence of nonlinearities from external sources. For the model to predict optimal measurement settings and defect detection capability, it should simulate these external sources of nonlinearity. A mathematical formulation was developed so they could be added to the model: these instrumentation nonlinearities were incorporated by adding to the main input signal another signal at twice the fundamental frequency:

$$P_{ext}(t) = A_{ap} \sin(2\pi f_0 t) w(t) + A_{NL} \sin(4\pi f_0 t) w(t) \tag{8-4}$$

where P_{ext} is the input acoustic pressure, k is the wavenumber, c is the sound velocity, A_{ap} and A_{NL} are the amplitudes of the input acoustic pressure signal component at the driving frequency and second harmonic frequency respectively. It is reminded that the input signal in the model is the external force applied to the first element $F_{ext} = AP_{ext}$ where A is the element's cross-sectional area.

Measurements described in a later section (8.3.3) enabled to quantify the level of nonlinearities generated by the external sources Φ_{EXT} for a TT set-up.

Consequently, by running the model in TT for a given specimen with no material or KB nonlinearities, A_{NL} can be found by matching the output nonlinear ratio with Φ_{EXT}.

8.2.4 Overview of the complete model

It can be seen in Figure 8.2 how the different parts of the model described in the previous section fit together.

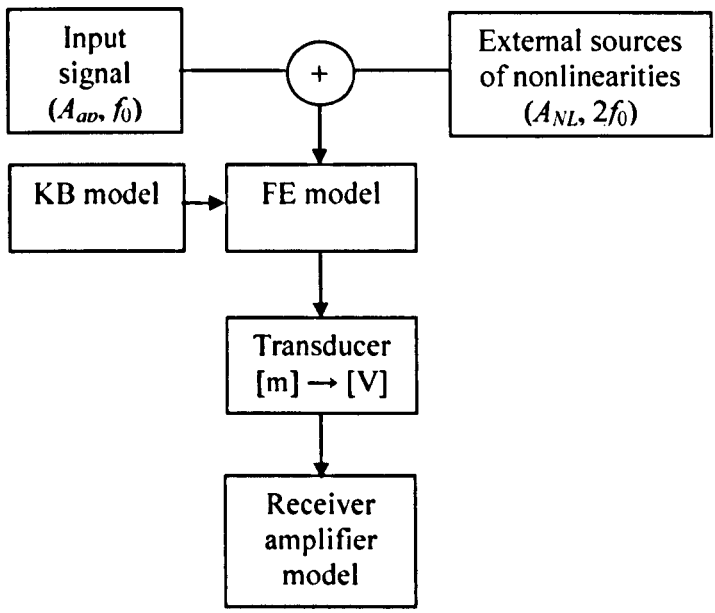

Figure 8.2. Block diagram of the complete model

8.3 Experimental measurements

Experimental measurements were carried out to obtain the parameters for the additional model elements described in the previous section.

8.3.1 Kissing bond nonlinearity

Measurements were taken by Yan [8] for a specimen consisting of two aluminium blocks, one of which had an adhesive layer (Table 8.1).

Table 8.1. Properties of compressively loaded specimen

Specimen	Shape	Thickness (mm) (Al/Ad/Al)	Description of nonlinearity
Compressively loaded specimen	Cylinder	40/2/50	Loaded disbond

The interfacial stiffness K_{LKB} was measured for a range of compressive loads corresponding to contact pressures from 0.1 to 11.2 MPa. In order to fit the experimental data, the relationship between interfacial stiffness and contact pressure in equation (8-2) was plotted in Figure 8.3 with the constants C and m at 1.15×10^{11} and 0.4539 respectively.

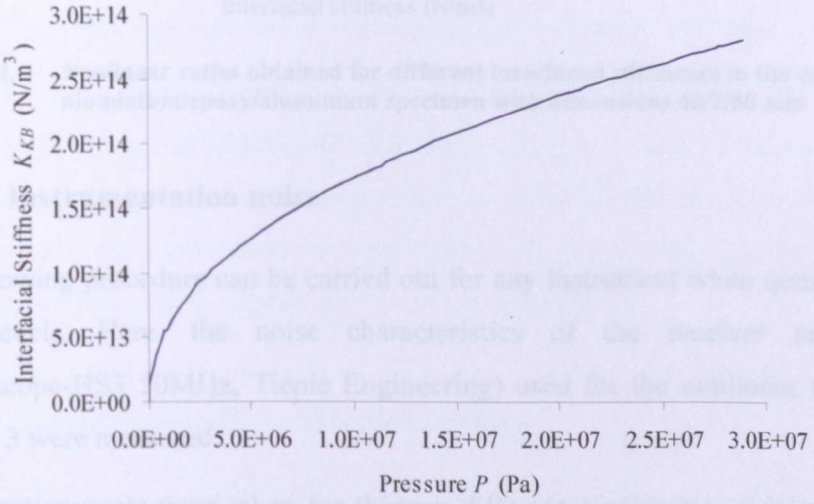

Figure 8.3. Empirical equation for quasi-static interfacial stiffness (K_{LKB}) as a function of contact pressure (P)

To compare Yan's experimental data with simulated data, the FE model was run sending the same signal (15-cycle Hanning windowed 3.5 MHz toneburst) into a model of the same specimen which consisted of 40 mm aluminium / 2 mm epoxy / 50 mm aluminium with a kissing bond at the first aluminium-epoxy interface (**Table 8.1**).

The stiffness factor $f_{KBstiff}$ was varied from 0.05 to 0.8 to have interfacial stiffnesses K_{LKB} ranging from 1.67×10^{13} to 2.68×10^{14} N/m^3. In order to have good agreement between simulated and experimental results (Figure 8.4), it was found that the nonlinear stiffness factor β_{KB} should be set to 300.

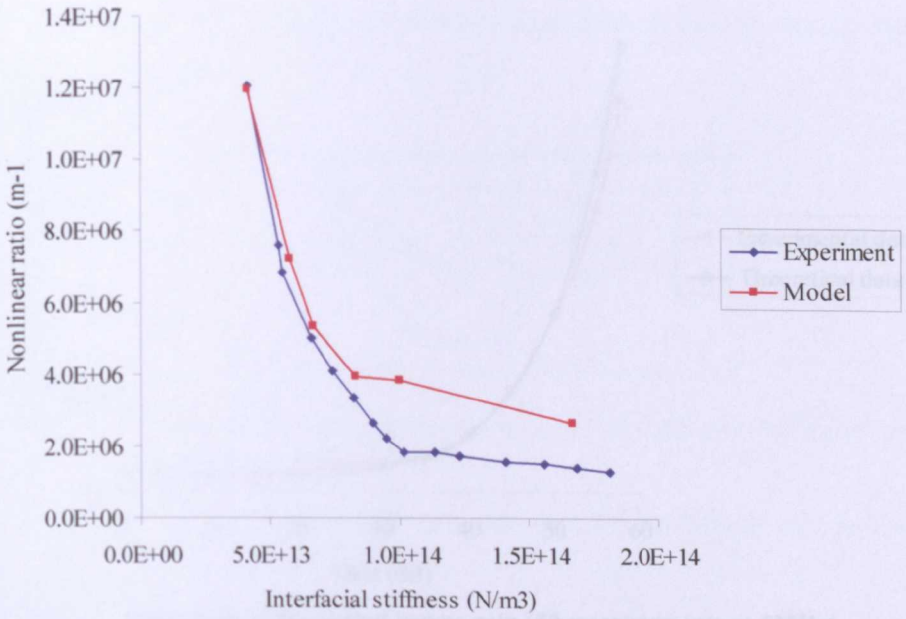

Figure 8.4. Nonlinear ratios obtained for different interfacial stiffnesses in the case of an aluminium/epoxy/aluminium specimen with dimensions 40/2/50 mm

8.3.2 Instrumentation noise

The following procedure can be carried out for any instrument when quantifying noise levels. Here, the noise characteristics of the receiver amplifier (Handyscope-HS3 50MHz, Tiepie Engineering) used for the nonlinear trials in Chapter 3 were measured.

Fifty measurements were taken for thirteen different sensitivities S from 0.1 to 80 V where the value of S denotes the full-scale range. These correspond therefore to amplification gains G between 1 and 800 according to the following formula:

$$G = 80/S \tag{8-5}$$

The RMS output noise amplitude was measured at these different gain levels and plotted in Figure 8.5. At low gains, n_{out} can be seen and as the gain increases, the contribution from n_{in} starts to dominate. To obtain the curve that fits best the experimental data points, two of these points — the experimental RMS noise amplitudes at $G = 1$ and $G = 100$ (i.e. 0 and 40 dB) respectively — were used for the two unknowns n_{in} and n_{out} in equation (8-3). By plotting the result, it can be seen in Figure 8.5 that there is good agreement between the experimental data and the theoretical values found using equation (8-3).

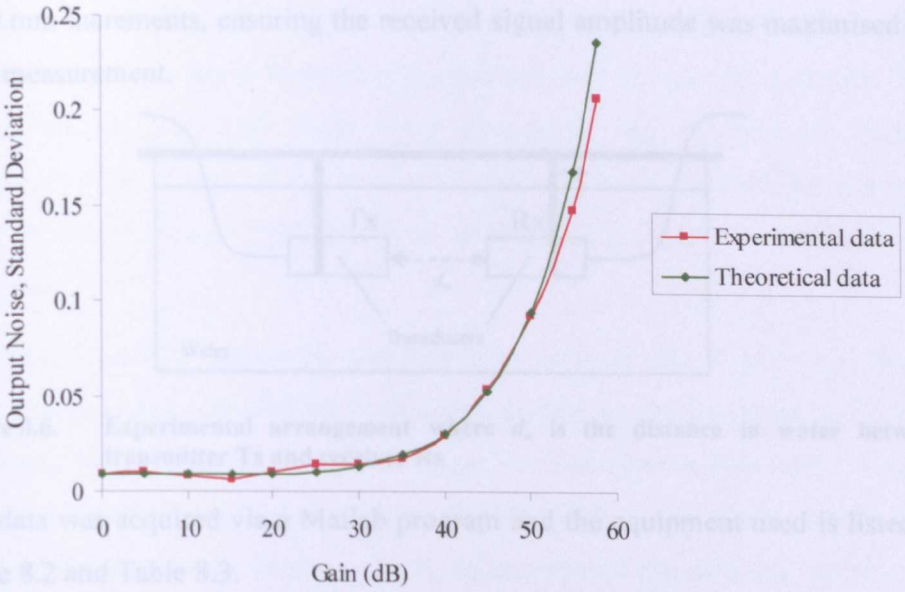

Figure 8.5. Noise level at the output versus gain (50 measurements at 5MHz)

It can be seen from Figure 8.5 that adding a receiver amplifier to the experimental set-up would generate an RMS noise level of 0.01 in the output i.e. would result in a signal-to-noise ratio (SNR) of about 46 dB. This noise curve is illustrative but not what would be experienced with the system described in the following section using a pulser-receiver as pre-amplifier.

8.3.3 Nonlinearities from external sources

Experimental measurements were carried out to quantify nonlinearities due to external sources. With an immersed TT configuration, nonlinearities might be generated by the electronic equipment (waveform generator, power amplifier, pre-amplifier), the transducers (both transmitter and receiver), the cables and water. A typical TT arrangement was set up in water with no specimen between transmitter Tx and receiver Rx. The aim was to measure nonlinear ratios Φ_x for different water propagation distances d_x as the ordinate at the origin of the curve Φ_x / d_x quantifies the amount of nonlinearities due to external sources.

Figure 8.6 shows the arrangement for an experiment that was carried out where a plastic container was filled with water. The transducers were held by identical purpose-built arms fitted to an aluminium rail which rested on the edges of the container. The vertical arm holding the receiver was progressively slid outwards

in 10 mm increments, ensuring the received signal amplitude was maximised for each measurement.

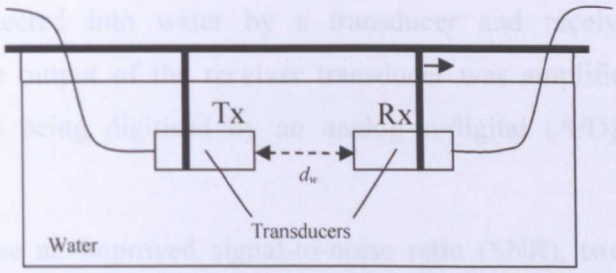

Figure 8.6. Experimental arrangement where d_x is the distance in water between transmitter Tx and receiver Rx

The data was acquired via a Matlab program and the equipment used is listed in Table 8.2 and Table 8.3.

Table 8.2. Electronics

Function	Model
Power Amplifier	Amplifier Research 75A250
Waveform generator	Handyscope HS3
Ultrasonic pulser- receiver	Panametrics 5072PR
Mains Power Pack	RS, 27.0 V, 2 A

Table 8.3. Transducers/hydrophone

Frequency	Model	Diameter/Number
5 MHz	Panametrics V310-SM	0.25"
10 MHz	Panametrics V312	0.25"
Needle Hydrophone	Precision Acoustics - HP Series High Performance	Needle No 498

Figure 8.7 shows the block diagram of the measurement system employed.

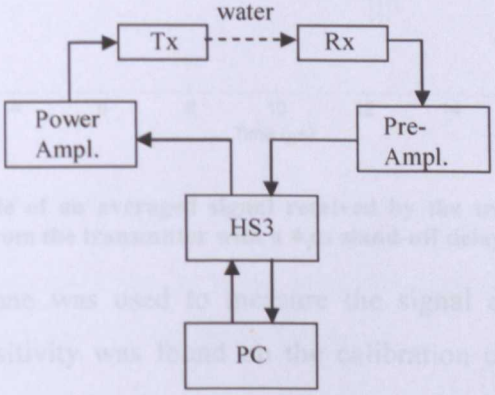

Figure 8.7. Experimental signal path

A 20-cycle Hanning windowed toneburst with a 5 MHz centre frequency was generated by an arbitrary function generator and sent to a power amplifier. This signal was injected into water by a transducer and received by another transducer. The output of the receiver transducer was amplified by a pulser-receiver before being digitised by an analog-to-digital (A/D) converter and processed.

In order to have an improved signal-to-noise ratio (SNR), twenty waveforms were averaged and recorded for each distance between the transducers, from 10 to 90 mm with 10 mm increments. A larger number of waveforms did not make the SNR significantly higher. The excitation voltage was about 100 V. The received signal was amplified by 12 dB. An example of the received waveform is shown in Figure 8.8.

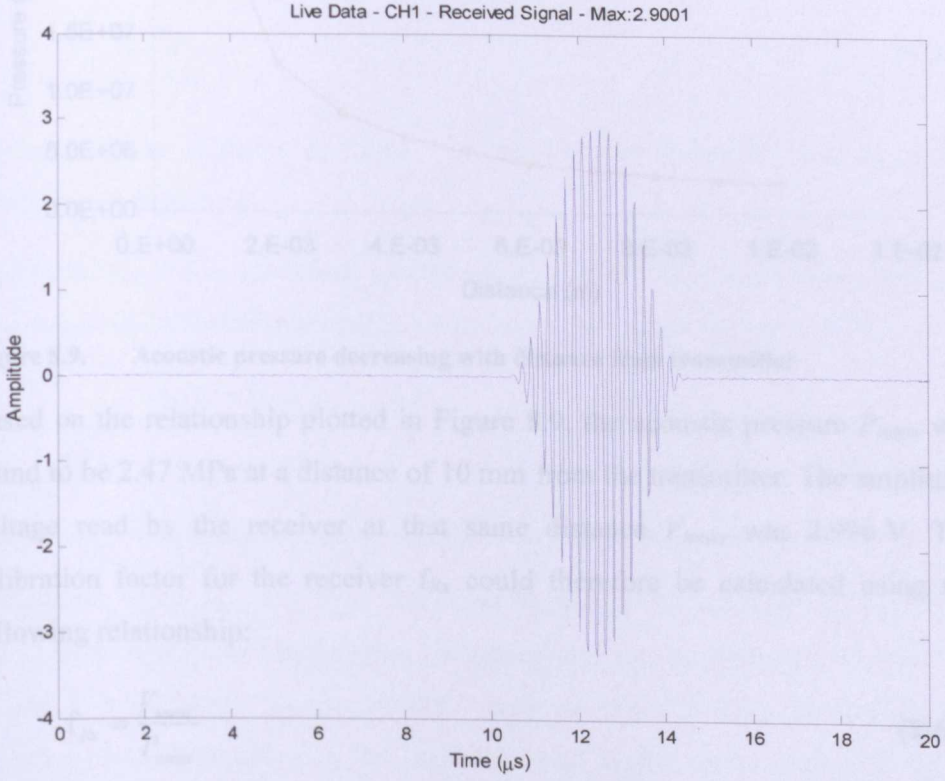

Figure 8.8. Example of an averaged signal received by the transducer placed 10 mm away from the transmitter with a 4 μs stand-off delay

A needle hydrophone was used to measure the signal coming out from the transmitter. Its sensitivity was found on the calibration chart provided by the

manufacturer, Precision Acoustics. It was therefore possible to calculate the equivalent acoustic pressure as seen in Table 8.4.

Table 8.4. Output acoustic pressure straight from the transmitter

Hydrophone at Tx	Sensitivity at 5 MHz	Acoustic Pressure
0.23 V	9.3 mV/MPa	24.7 MPa

The acoustic pressure 10 mm away from the transmitter was found by applying the inverse distance law stating that the acoustic pressure decreases with one over distance as seen in Figure 8.9.

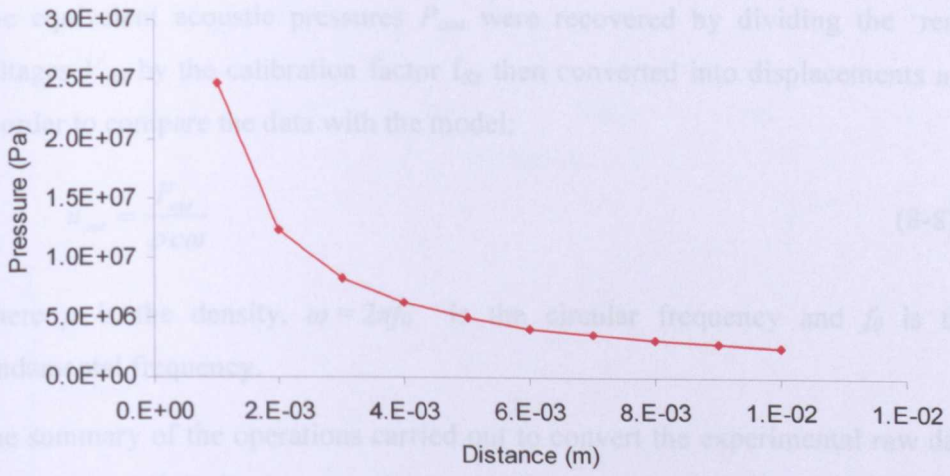

Figure 8.9. Acoustic pressure decreasing with distance from transmitter

Based on the relationship plotted in Figure 8.9, the acoustic pressure P_{meas} was found to be 2.47 MPa at a distance of 10 mm from the transmitter. The amplitude voltage read by the receiver at that same distance V_{meas} was 2.996 V. The calibration factor for the receiver f_{Rx} could therefore be calculated using the following relationship:

$$f_{Rx} = \frac{V_{meas}}{P_{meas}} \tag{8-6}$$

and was found to be 1.21×10^{-6} V/Pa.

The collected data was in Volts. As it had been pre-amplified, the actual voltage received by the transducer V_{out} was recovered by:

$$V_{out} = \frac{V_{meas}}{10^{G_{dB}/20}} \tag{8-7}$$

where G_{dB} is the receiver amplification gain in dB.

Results are given in Table 8.5.

Table 8.5. Output signal amplitude

Amplified output amplitude V_{meas} (V)	Amplification gain G (dB)	Real output amplitude V_{out} (V)
2 – 3	12	0.5 – 0.75

The equivalent acoustic pressures P_{out} were recovered by dividing the 'real' voltages V_{out} by the calibration factor f_{Rx} then converted into displacements u_{out} in order to compare the data with the model:

$$u_{out} = \frac{P_{out}}{\rho c \omega} \tag{8-8}$$

where ρ is the density, $\omega = 2\pi f_0$ is the circular frequency and f_0 is the fundamental frequency.

The summary of the operations carried out to convert the experimental raw data into output particle displacement is given in the flow chart in Figure 8.10.

$$\underset{[V]}{V_{meas}} \xrightarrow{\div 10^{G_{dB}/20}} \underset{[V]}{V_{out}} \xrightarrow{\div f_{Rx}} \underset{[Pa]}{P_{out}} \xrightarrow{\div \rho c \omega} \underset{[m]}{u_{out}}$$

Figure 8.10. Conversion of experimental raw data into particle displacement

The output signal u_{out} was then processed by taking its Fast Fourier Transform (FFT) from which the fundamental frequency and second harmonic amplitudes, A_1 and A_2 respectively, were extracted. Nonlinear ratios Φ were calculated using equation (4-18) where $\Phi = A_1/A_2^2$ and multiplied by the corresponding damping factor r_d to take damping into account:

$$r_d = \left(\sum_{n=1}^{\infty} \frac{(-2\alpha x)^{n-1}}{n!} \right)^{-1} \tag{6-22}$$

where α is the attenuation coefficient in Np/(m.Hz).

Ultrasonic attenuation is very low in water with an attenuation coefficient of 2.3×10^{-14} Np/(m.Hz^2) [77]. The values obtained for Φ are plotted against propagation distance in Figure 8.11.

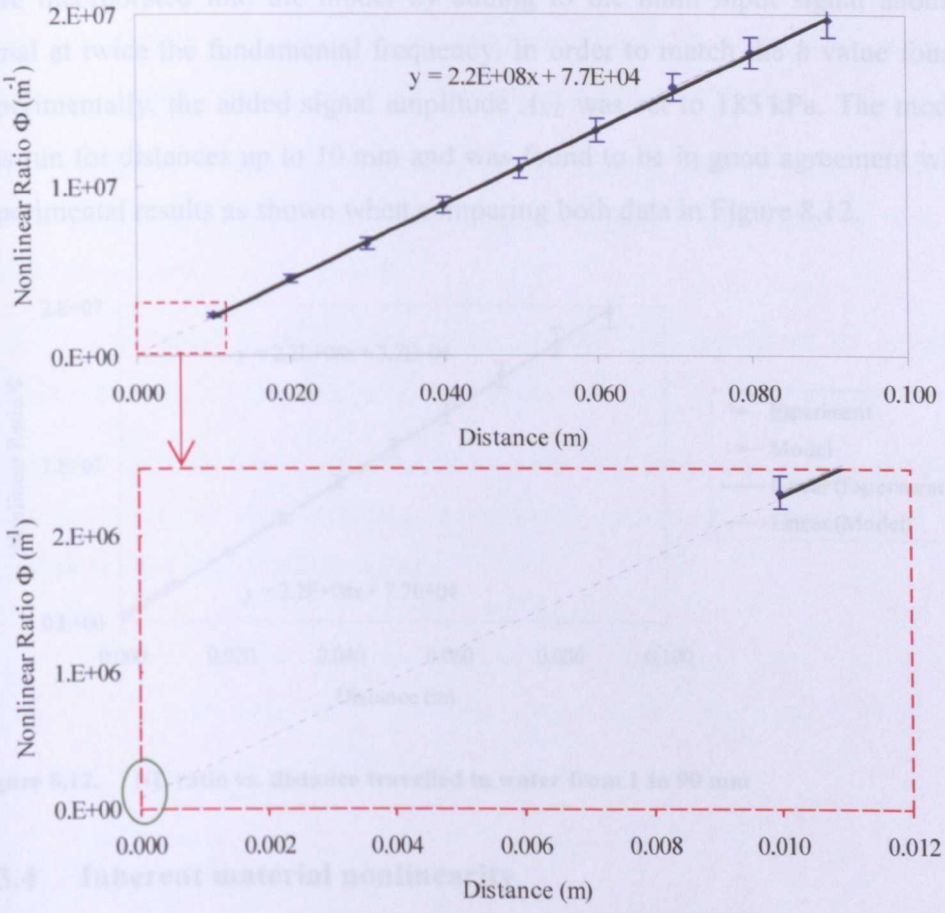

Figure 8.11. NL ratio vs. distance travelled in water from 10 to 90 mm

As the signal propagates towards the receiver, it is attenuated due to beam spreading and dissipative attenuation of ultrasound. The latter increases with frequency according to a power law so harmonics experience greater attenuation than the fundamental. However, compared to the harmonic signal amplitude, the nonlinear ratio $\Phi = A_1/A_2^2$ typically utilised in nonlinear ultrasonic analysis has no dependency on both incident ultrasound pressure A_{ap} and attenuation as demonstrated in Appendix B.

Figure 8.11 shows that the level of nonlinearity measured in the received signal was increasing with distance propagated in water. This confirms that water is a nonlinear medium that distorts the ultrasonic propagating wave. The fact that the

graph does not pass through the origin indicates system nonlinearity. The value that therefore quantifies system nonlinearity is the ordinate at the origin b which in the case of this TT configuration is 7.7×10^{4} m^{-1}.

As mentioned in section 8.2.3, these nonlinearities caused by external sources were incorporated into the model by adding to the main input signal another signal at twice the fundamental frequency. In order to match the b value found experimentally, the added signal amplitude A_{NL} was set to 185 kPa. The model was run for distances up to 10 mm and was found to be in good agreement with experimental results as shown when comparing both data in Figure 8.12.

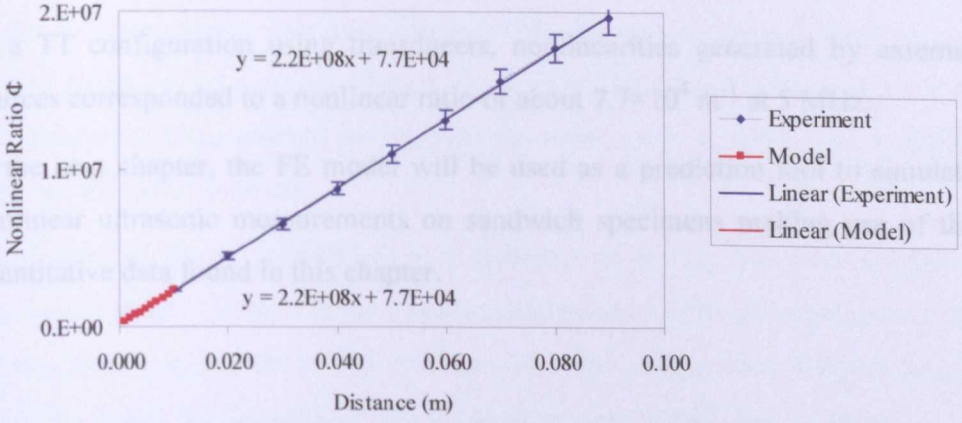

Figure 8.12. NL ratio vs. distance travelled in water from 1 to 90 mm

8.3.4 Inherent material nonlinearity

From the experimental measurements carried out in section 8.3.3, the linear fit obtained in Figure 8.11 enabled the calculation of the nonlinear parameter β for water using:

$$\beta = r_w r_d \frac{8c^2}{\omega^2} \times \frac{\Phi}{x} \tag{8-9}$$

where r_w is the window ratio, r_d is the damping factor, Φ/x is the gradient of nonlinear ratio vs. distance (plot shown in Figure 8.11). The FFT scaling factor r_s was already applied when calculating the Fast Fourier Transforms (FFT).

A nonlinear value β of 5.3 was found which is only 1.9 % larger than 5.2, the most common nonlinear value found in the literature [91].

8.4 Conclusion

In this chapter, the FE model was further developed by adding elements that simulate KB, noise and external sources of nonlinearities.

A KB was modelled as one element of the adhesive layer with a linear stiffness $K_{LKB} = 1.15\times10^{11} P^{0.4539}$ where P is the external applied mechanical pressure from Yan's experiment [7], and nonlinear stiffness $K_{NLKB} = -300\ K_{LKB}$.

When adding an electronic instrument to the set-up, the root-mean-squared (RMS) amplitude of the net additive noise at the output was found to be 0.01 which corresponds to a 46 dB SNR.

In a TT configuration using transducers, nonlinearities generated by external sources corresponded to a nonlinear ratio of about 7.7×10^{4} m^{-1} at 5 MHz.

In the next chapter, the FE model will be used as a prediction tool to simulate nonlinear ultrasonic measurements on sandwich specimens making use of the quantitative data found in this chapter.

Chapter 9

Application of the one-dimensional finite element model to optimise experimental measurements

9.1 Introduction

In the previous chapter, the finite-element (FE) model was further developed by adding elements that simulate kissing bonds (KB), noise and external sources of nonlinearities. Experimental measurements were used to find the variables required for these elements.

In this chapter, the model will be run as a prediction tool on two given sandwich specimens. Based on these results, recommendations will be given regarding the driving frequency and the set-up configuration. The maximum water path length that still enables the detection of KB for such specimens will also be given.

9.2 Figures of merit

Several figures of merit were defined to quantitatively compare the performance of post-processing time window lengths as well as different set-up configurations.

The first figure of merit C_1 evaluates the feasibility of detecting nonlinearities, and if so, how well they can be seen. The questions to be answered are therefore whether a peak is discernible at the second harmonic $2f_0$ and how high is its amplitude A_2 compared to those of its adjacent side lobe peaks. This was done by measuring the amplitude of the signal adjacent peaks on either side of the expected second harmonic peak, calculating their mean and comparing it with A_2 as sketched in Figure 9.1. The logarithmic difference obtained represents C_1:

$$C_1 = 20\log_{10}\left(\frac{A_2}{0.5\left(\left|u_{out}(2f_0 - f_-)\right| + \left|u_{out}(2f_0 + f_+)\right|\right)}\right) \quad (9\text{-}1)$$

where f_- and f_+ are the frequencies of the first maxima below and above $2f_0$.

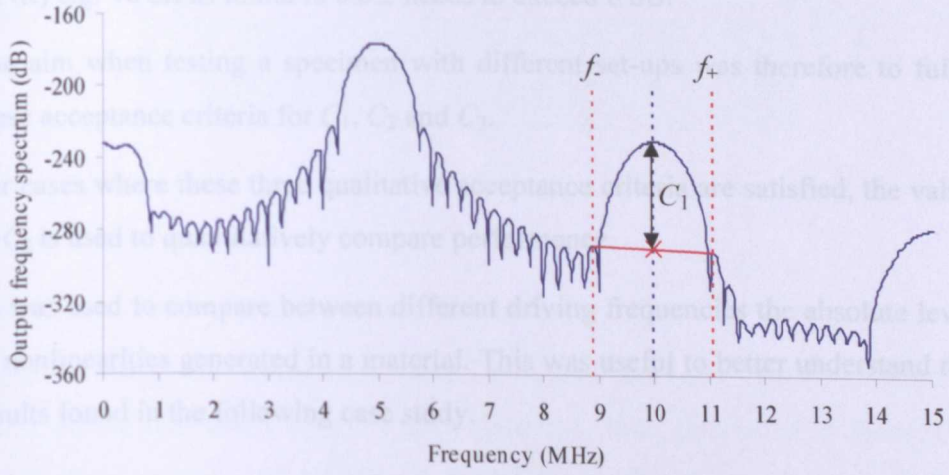

Figure 9.1. Sketch of the calculation method for C_1

The second figure of merit C_2 measures the ability of a KB to be detected by measuring the contrast between both cases (with and without a KB present — $\exists$KB and $\nexists$KB respectively). This was done by calculating the logarithmic difference between the nonlinear ratios Φ of both cases:

$$C_2 = 20\log_{10}(\Phi(\exists\text{KB}) / \Phi(\nexists\text{KB})) \quad (9\text{-}2)$$

The third figure of merit C_3 captures a sense of the size of nonlinearities that need to be measured by comparing the second harmonic and fundamental frequency amplitudes, A_1 and A_2 respectively, in a logarithmic scale:

$$C_3 = 20\log_{10}\left(\frac{A_2}{A_1}\right) \quad (9\text{-}3)$$

The fourth figure of merit C_4 measures the overall system output nonlinearity independently of input amplitude by calculating the nonlinear ratio in a logarithmic scale:

$$C_4 = 20\log_{10}\left(\frac{A_2}{A_1^2}\right) \quad (9\text{-}4)$$

For the second harmonic peak to be considered "discernible" and for any difference to be seen between the cases with and without KB, C_1 and C_2 need to exceed a minimum threshold (6 dB for both). Also, to be able to measure the nonlinearities in practice, the sum of C_3 and the expected signal-to-noise ratio (SNR) e.g. 46 dB as found in 8.3.2 needs to exceed 6 dB.

The aim when testing a specimen with different set-ups was therefore to fulfil these acceptance criteria for C_1, C_2 and C_3.

For cases where these three qualitative acceptance criteria are satisfied, the value of C_2 is used to quantitatively compare performance.

C_4 was used to compare between different driving frequencies the absolute level of nonlinearities generated in a material. This was useful to better understand the results found in the following case study.

9.3 Specimens

Two adhesive joints — sandwich specimens made of aluminium adherends and epoxy resin adhesive — were considered. The thick specimen had 20 and 5 mm thick aluminium and epoxy layers respectively to enable the first transmitted toneburst to be isolated from any subsequent reflections. The thin specimen had 2 and 0.3 mm thick aluminium and epoxy layers respectively to be more representative of the dimensions of adhesive joints used in the aerospace industry.

When a KB was simulated, it was located at the aluminium-epoxy interface near side 1 as seen in Figure 9.2.

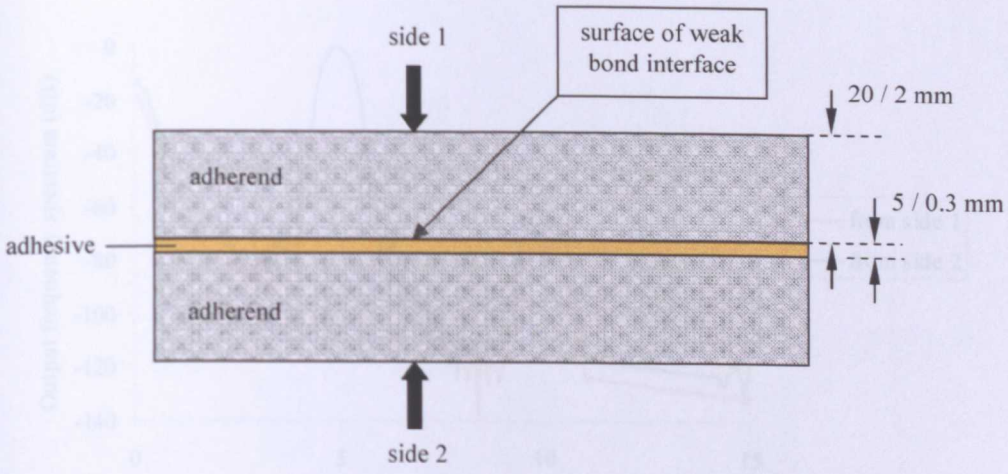

Figure 9.2. Adhesive joint specimen

When sending an ultrasonic wave in these adhesive joint specimens, recommendations from Chapter 7 were followed. Also, interfacial stiffnesses of 3×10^{12} N/m^3 and 6.4×10^{13} N/m^3 were chosen to simulate the presence of a KB in the thick and the thin specimens respectively. The external sources of nonlinearities were added by setting A_{NL} to 415 and 813 Pa for the thick and the thin specimens respectively. This approach used is a reasonable approximation but in reality, A_{NL} changes with different distances and more work on this area is required.

The only parameters that had to be set by the operator were the driving frequency and the time window length for post-processing. The model was therefore run changing these parameters in order to find out which ones gave the best results based on the figures of merit defined in section 9.2.

This study is about finding the ultimate performance but it should be noted that for industry, it is worst case performance that is of most interest. Also, the following results are obtained from simulations not experiments.

9.4 Through-transmission in contact

First, it had to be decided from what side of the specimen to send the ultrasonic signal for TT testing. Frequency spectra obtained when sending the toneburst from each side are plotted in Figure 9.3.

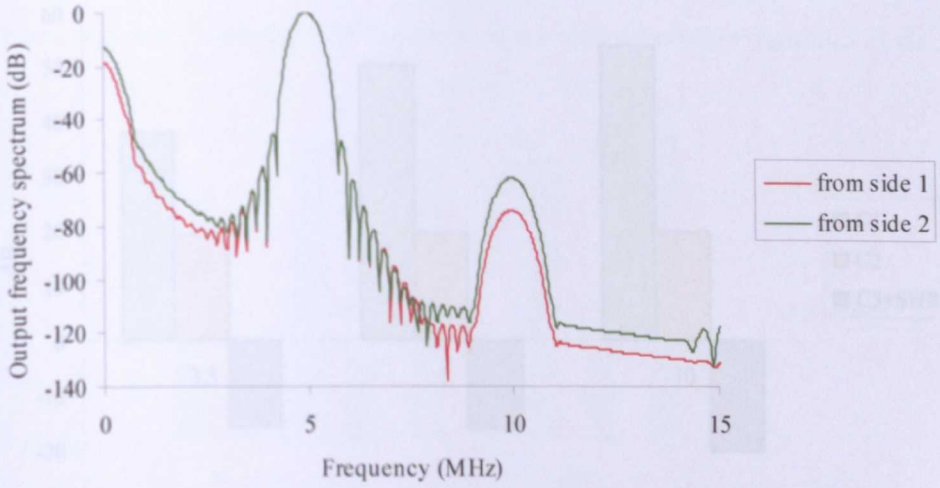

Figure 9.3. **Frequency spectra of signal transmitted through the thick specimen at 5 MHz from sides 1 and 2 (sides near or further away from the weak bond respectively) with a KB present**

It was found that sending the signal from side 2 resulted in a higher second harmonic amplitude as seen in Figure 9.3 and therefore in a higher figure of merit C_2. In effect, if the KB is situated on the side further from the transmitter then the signal is first transmitted through two layers of nonlinear material and has, as a result, a larger nonlinear component when hitting the KB. The nonlinearities generated by the KB seem therefore to be further enhanced when the signal has already gone through layers of nonlinear material.

The model was therefore run from side 2 for both specimens at 3.5, 5 and 10 MHz driving frequencies with a set-up similar to the one used for measuring nonlinearities from external sources in section 8.3.3. All input tonebursts had 20 cycles. The output transmitted signal was processed as described in section 6.3.1.

The thick specimen enabled the first transmitted toneburst to be resolved. The values obtained for C_1, C_2 and C_3 with each driving frequency are plotted in Figure 9.4 for comparison.

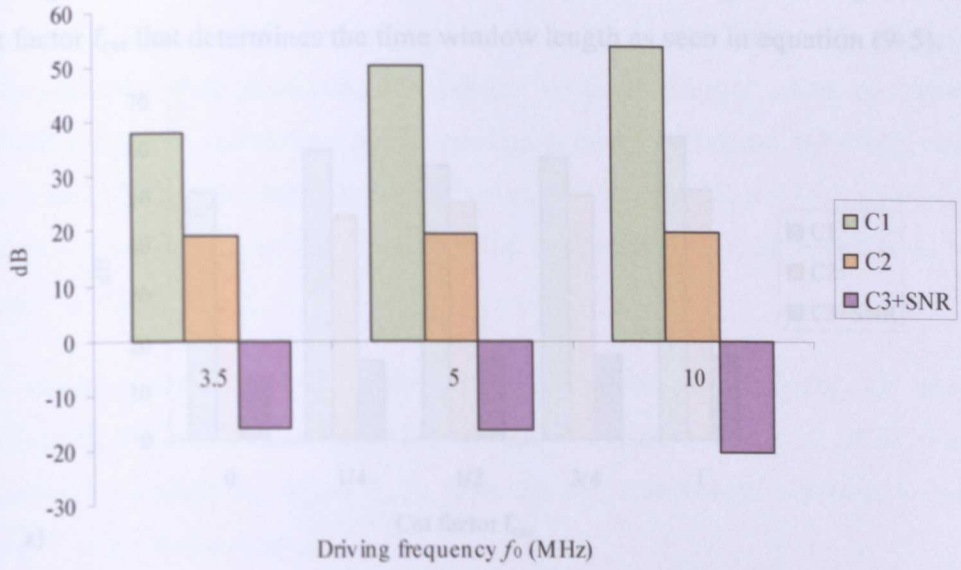

Figure 9.4. **Figures of merit C_1, C_2 and C_3 obtained for the thick specimen in contact TT at 3.5, 5 and 10 MHz driving frequencies where SNR = 46 dB**

It can be seen from Figure 9.4 that C_3 does not fulfil the acceptance criterion whichever the driving frequency. This means that nonlinearities would not be seen in the output frequency spectra with a SNR of 46 dB. However, if a SNR of 72 dB was achieved, then nonlinearities generated by the KB would be detected. And although more contrast between the second harmonic peak and its side lobe levels (higher C_1) as well as slightly more contrast between the cases with and without KB (higher C_2) would be achieved at 10 MHz, the differences in C_2 are marginal between driving frequencies.

For the thin specimen, as the transmitted toneburst could not be resolved, the output signal portions extracted for analysis were taken using different time window lengths. The portion of the transmitted raw signal $u_{out}(t)$ was cut for analysis at $t_{start} = \Sigma\, d_i/c_i$ where d_i and c_i are the thickness and sound velocity of each material layer, and $t_{end} = t_{start} + T_w$ where T_w is the time window length that, in the TT case, is defined by:

$$T_w = T_{tb} + f_{cut}\, T_{tb} \tag{9-5}$$

where f_{cut} is the cut factor and T_{tb} is the toneburst duration.

The figures of merit obtained in each case are plotted in Figure 9.5 against the cut factor f_{cut} that determines the time window length as seen in equation (9-5).

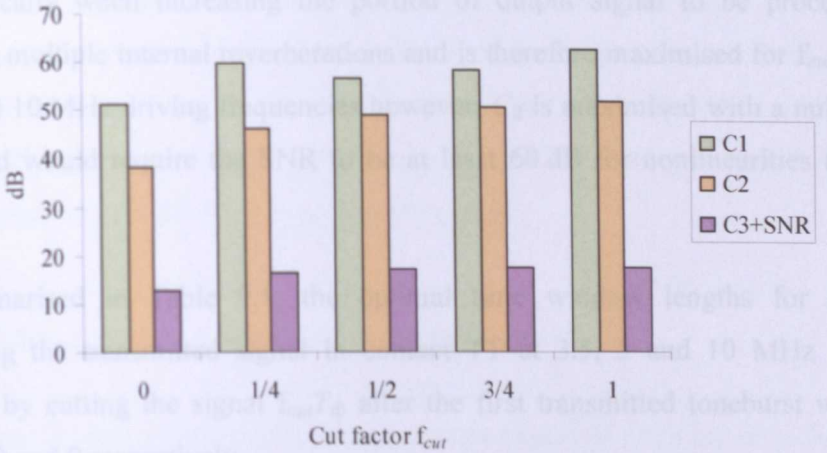

a)

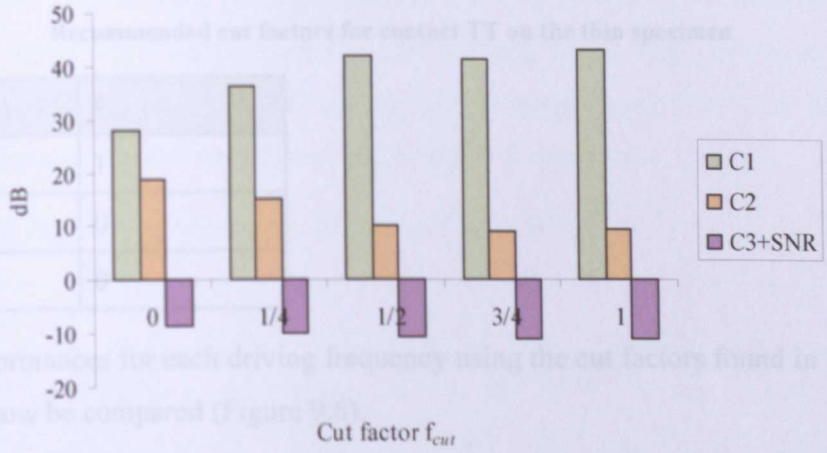

b)

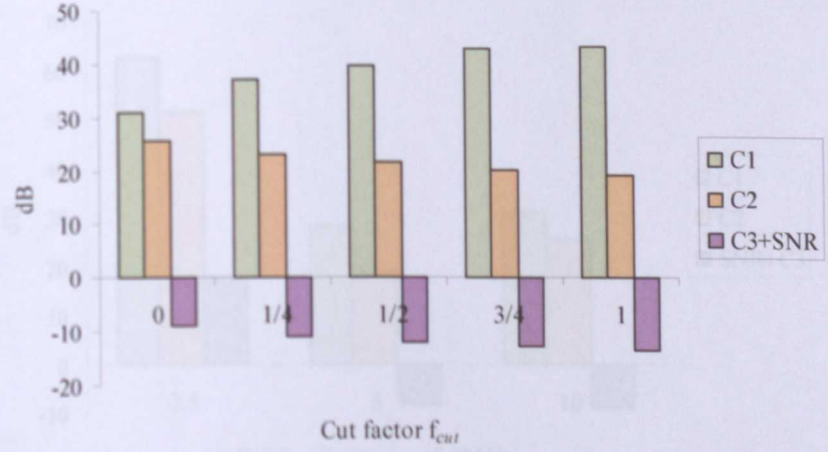

c)

Figure 9.5. **Figures of merit C_1, C_2 and C_3 obtained for different time window lengths at 3.5, 5 and 10 MHz driving frequencies — a), b) and c) respectively — when testing the thin specimen in contact TT where SNR = 46 dB**

From Figure 9.5, it can be seen that 3.5 MHz is the only frequency at which the figure of merit C_3 fulfils the acceptance criterion. At that frequency, C_2 rises monotonically when increasing the portion of output signal to be processed including multiple internal reverberations and is therefore maximised for $f_{cut} = 1$. For 5 and 10 MHz driving frequencies however, C_2 is maximised with a null cut factor and would require the SNR to be at least 60 dB for nonlinearities to be seen.

As summarised in Table 9.1, the optimal time window lengths for post-processing the transmitted signal in contact TT at 3.5, 5 and 10 MHz were obtained by cutting the signal $f_{cut}T_{tb}$ after the first transmitted toneburst where $f_{cut} = 1, 0$ and 0 respectively.

Table 9.1. Recommended cut factors for contact TT on the thin specimen

f_0 (MHz)	f_{cut}
3.5	1
5	0
10	0

The performances for each driving frequency using the cut factors found in Table 9.1 can now be compared (Figure 9.6).

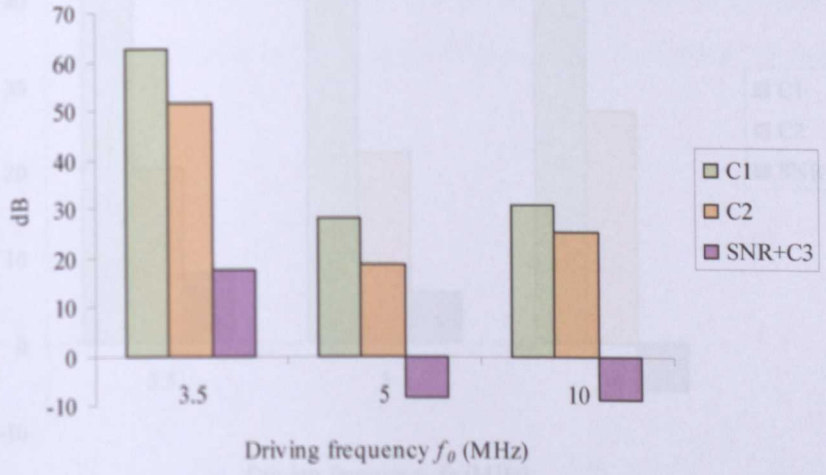

Figure 9.6. Figures of merit C_1, C_2 and C_3 obtained for the thin specimen in contact TT at 3.5, 5 and 10 MHz driving frequencies where SNR = 46 dB

It can be seen in Figure 9.6 that all three figures of merit were optimised when using a 3.5 MHz driving frequency. In effect, the second harmonic peak was more apparent (C_1 maximum), the difference between the cases with and without KB was larger (C_2 maximum) and the level of nonlinearities was above the noise level measured for the equipment described in 8.3.2. (SNR+C_3 > 6 dB). Nonlinearities generated by the KB would only be seen using 5 and 10 MHz driving frequencies if the SNR is no less than 60 dB.

9.5 Through-transmission in immersion

To simulate immersion testing in TT, two water layers of identical thickness d_w were added, one in front of the specimen and one behind the specimen. The received signal was measured after the water back layer. The same figures of merit were calculated for 3.5, 5 and 10 MHz driving frequencies with 10 mm water distances between transducers and immersed specimen.

Results for the thick specimen are plotted in Figure 9.7.

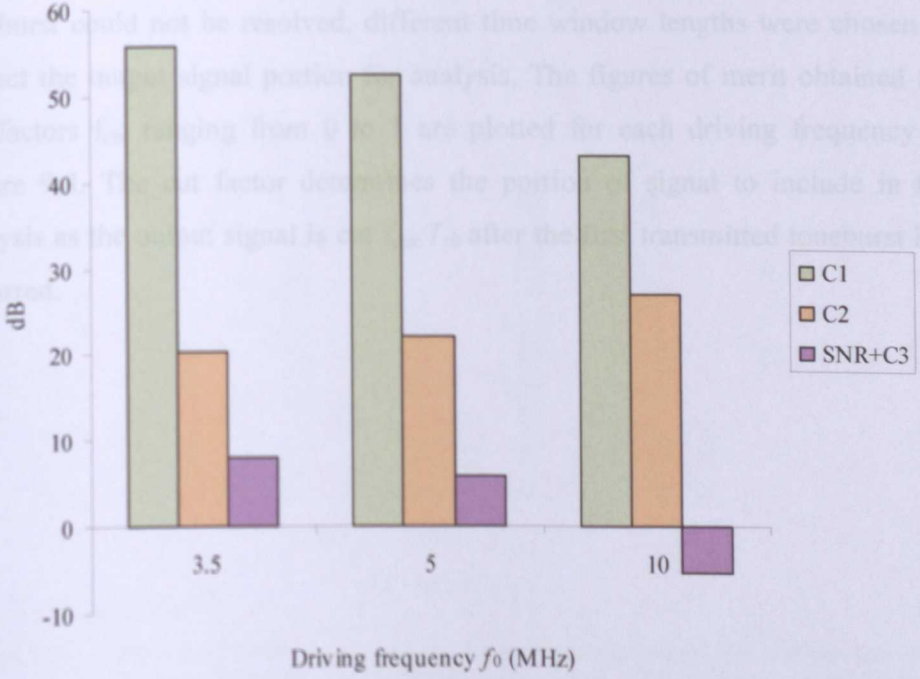

Figure 9.7. **Figures of merit C_1, C_2 and C_3 obtained for the thick specimen in immersion TT at 3.5, 5 and 10 MHz driving frequencies where d_w = 10 mm and SNR = 46 dB**

It can be seen in Figure 9.7 that the level of nonlinearities in the transmitted signal (C_3) is larger than when testing the specimen in contact TT where they could not be detected with the 46 dB SNR at any driving frequency. This is probably due to the compounded nonlinearities generated by the extra layers of water.

Nonlinearity in 10 mm of water was compared between driving frequencies by calculating C_4. It was found that the nonlinearity in water is higher at 5 and 10 MHz (131 and 144 dB) compared with that at 3.5 MHz (124 dB). This would explain the fact that the transmitted signal has a higher nonlinear component after the water layer at higher frequencies that gets significantly more distorted by the presence of a KB. This results in the figure of merit C_2 increasing with driving frequency. However, at 10 MHz, a minimum SNR of 60 dB is required for nonlinearities to be seen. This is due to the higher attenuation of the second harmonic amplitude in epoxy as found when comparing C_3 values for single layers of material.

For the thin specimen, the same procedure as for the thick specimen was carried out: adding a 10 mm water layer each side of the specimen. As the transmitted toneburst could not be resolved, different time window lengths were chosen to extract the output signal portion for analysis. The figures of merit obtained for cut factors f_{cut} ranging from 0 to 1 are plotted for each driving frequency in Figure 9.8. The cut factor determines the portion of signal to include in the analysis as the output signal is cut $f_{cut}\, T_{tb}$ after the first transmitted toneburst has occurred.

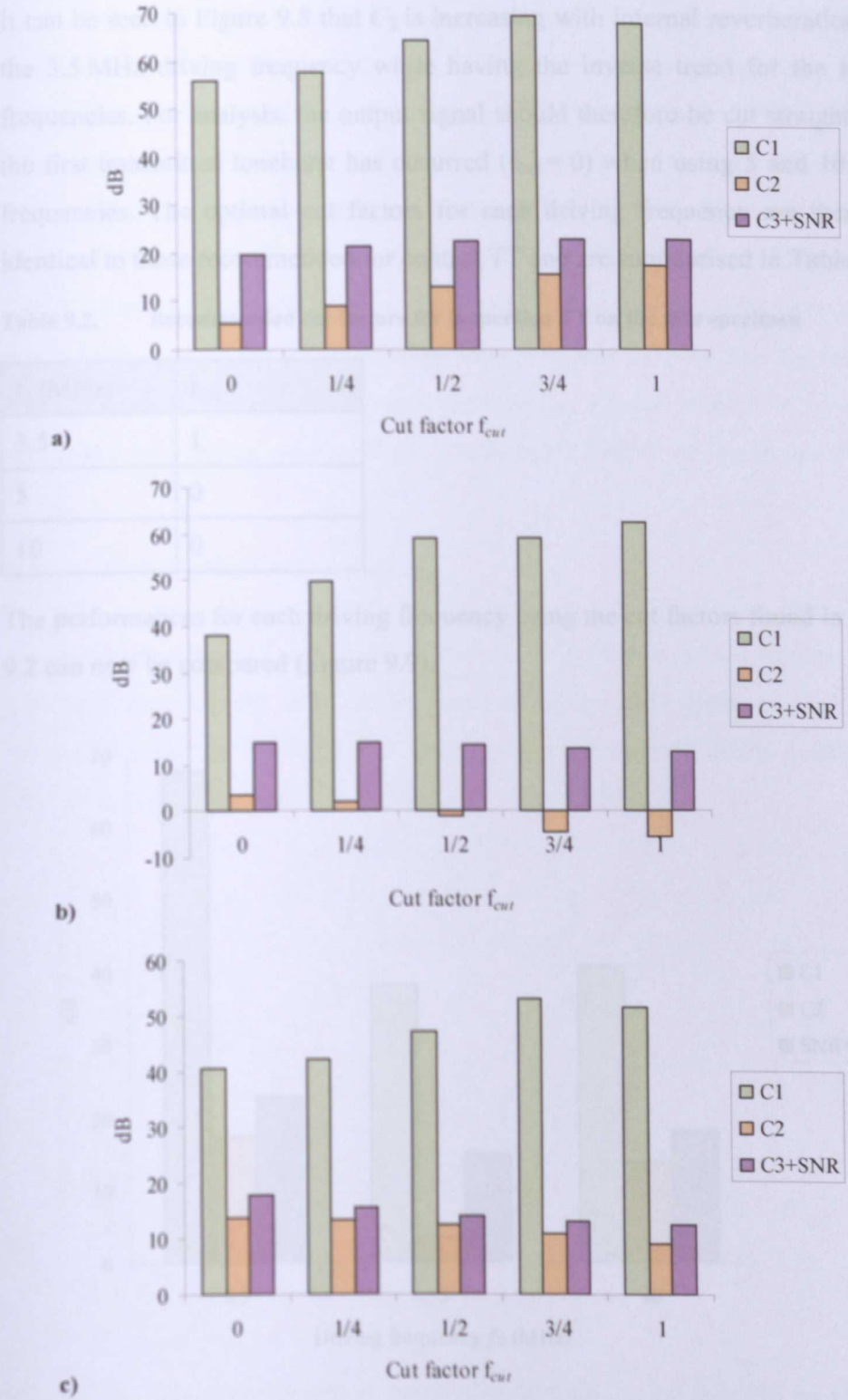

Figure 9.8. **Figures of merit C_1, C_2 and C_3 obtained for different time window lengths at 3.5, 5 and 10 MHz driving frequencies — a), b) and c) respectively — when testing the thin specimen in immersion TT where d_w = 10 mm and SNR = 46 dB**

It can be seen in Figure 9.8 that C_2 is increasing with internal reverberations for the 3.5 MHz driving frequency while having the inverse trend for the higher frequencies. For analysis, the output signal should therefore be cut straight after the first transmitted toneburst has occurred ($f_{cut} = 0$) when using 5 and 10 MHz frequencies. The optimal cut factors for each driving frequency are therefore identical to those recommended for contact TT and are summarised in Table 9.2.

Table 9.2. Recommended cut factors for immersion TT on the thin specimen

f_0 (MHz)	f_{cut}
3.5	1
5	0
10	0

The performances for each driving frequency using the cut factors found in Table 9.2 can now be compared (Figure 9.9).

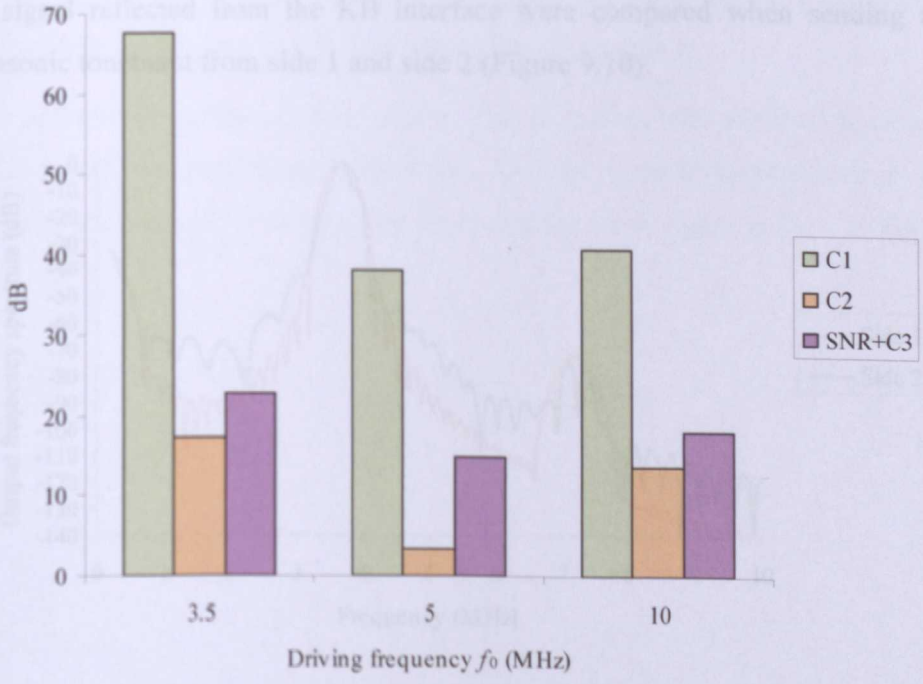

Figure 9.9. Figures of merit C_1, C_2 and C_3 obtained for the thin specimen in immersion TT at 3.5, 5 and 10 MHz driving frequencies where $d_w = 10$ mm and SNR = 46 dB

Figure 9.9 shows that for a 10 mm water distance either side of the specimen, nonlinearities due to a KB are not discernible using a 5 MHz driving frequency

($C_2 < 6$ dB). At 10 MHz, nonlinearities in water are larger than at lower frequencies as found when calculating C_4. The resulting larger nonlinear signal component gets increased more significantly when interacting with the KB. This could explain C_2 being higher at 10 MHz than at 5 MHz. However, when taking a larger portion of the transmitted signal at 3.5 MHz, all three figures of merit are higher than those obtained with higher driving frequencies. In effect, it was found when calculating C_4 for single layers of aluminium and epoxy, that nonlinearities generated by these materials are higher at 3.5 MHz. By taking a larger portion of the transmitted signal for analysis, internal reflections within the adhesive joint were included making C_2 higher at 3.5 MHz driving frequency.

9.6 Pulse-echo in contact

The major advantage of pulse-echo (PE) over TT for industrial application is that it requires access to the structure from one side only. First, frequency spectra of the signal reflected from the KB interface were compared when sending the ultrasonic toneburst from side 1 and side 2 (Figure 9.10).

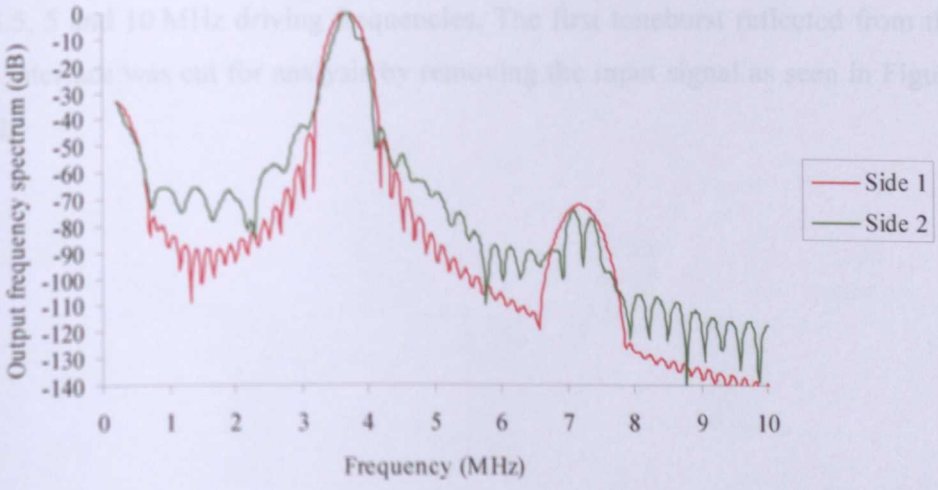

Figure 9.10. Frequency spectra of signal reflected from the KB interface for the thick specimen at 3.5 MHz from sides 1 and 2 (sides near or further away from the weak bond respectively)

It was found as seen in Figure 9.10 that a slightly higher second harmonic amplitude was found when the signal was sent from side 1 but also that the

frequency spectrum showed lower side lobes. The figures of merit for these two cases (transmit from side 1 and from side 2) are compared in Figure 9.11.

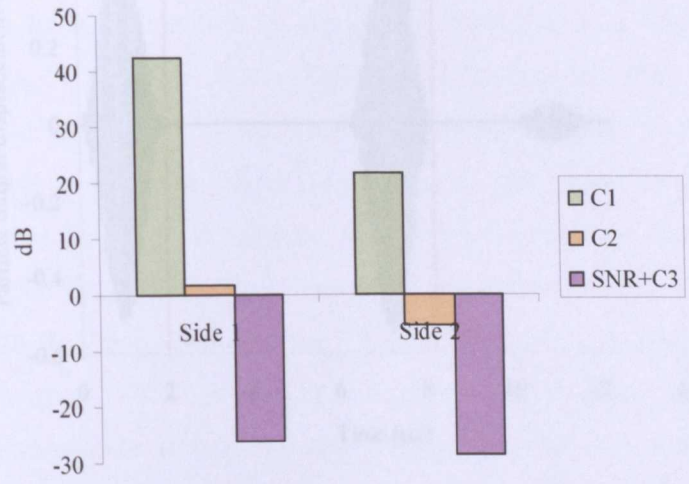

Figure 9.11. Figures of merit C_1, C_2 and C_3 obtained for the thick specimen when reflecting a 3.5 MHz toneburst from the KB interface where SNR = 46 dB

The results plotted in Figure 9.11 confirm that the three figures of merit are higher when sending the signal from side 1 than from side 2.

PE was therefore performed from side 1, first in contact with the thick specimen at 3.5, 5 and 10 MHz driving frequencies. The first toneburst reflected from the KB interface was cut for analysis by removing the input signal as seen in Figure 9.12.

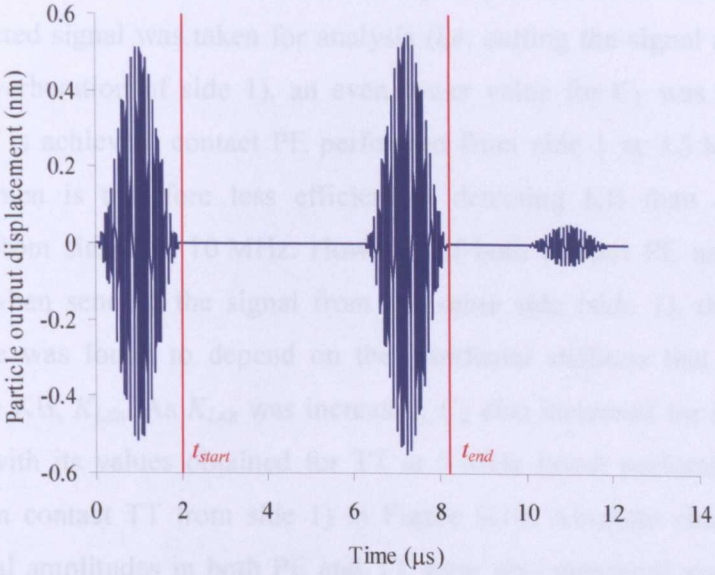

Figure 9.12. Example of time-domain PE signal for the thick specimen with cutting lines at t_{start} (to remove input signal) and t_{end} (to take the first reflection from the top adherend layer only)

The figures of merit obtained for the different driving frequencies were compared in Figure 9.13.

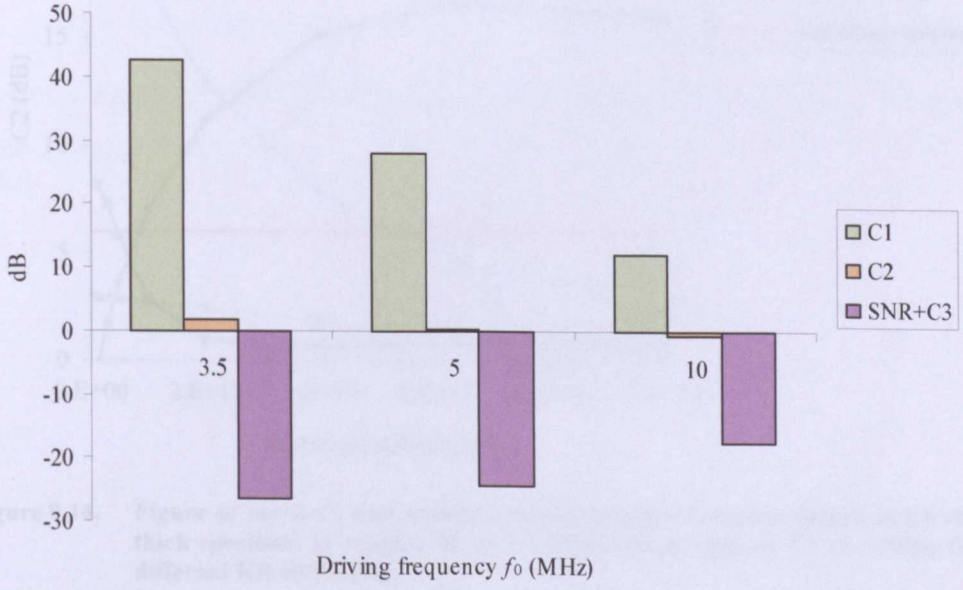

Figure 9.13. Figures of merit C_1, C_2 and C_3 obtained for the thick specimen in contact PE where SNR = 46 dB

It was found as seen in Figure 9.13 that the figures of merit C_2 and C_3 did not fulfil the acceptance criteria for any driving frequency. However, both C_1 and C_2

were optimised when using a 3.5 MHz driving frequency. When a larger portion of the reflected signal was taken for analysis (i.e. cutting the signal after the 4th multiple reverberation of side 1), an even lower value for C_2 was found. If a 72 dB SNR is achieved, contact PE performed from side 1 at 3.5 MHz on the thick specimen is therefore less efficient at detecting KB than contact TT performed from side 2 at 10 MHz. However, if both contact PE and TT were compared when sending the signal from the same side (side 1), their relative performance was found to depend on the interfacial stiffness that was set to simulate the KB, K_{LKB}. As K_{LKB} was increased, C_2 also increased for PE and was compared with its values obtained for TT at 5 MHz (most performing driving frequency in contact TT from side 1) in Figure 9.14. Absolute changes of the output signal amplitudes in both PE and TT were also measured and plotted as dotted lines in Figure 9.14 to understand how linear ultrasonic measurements compared with nonlinear ones.

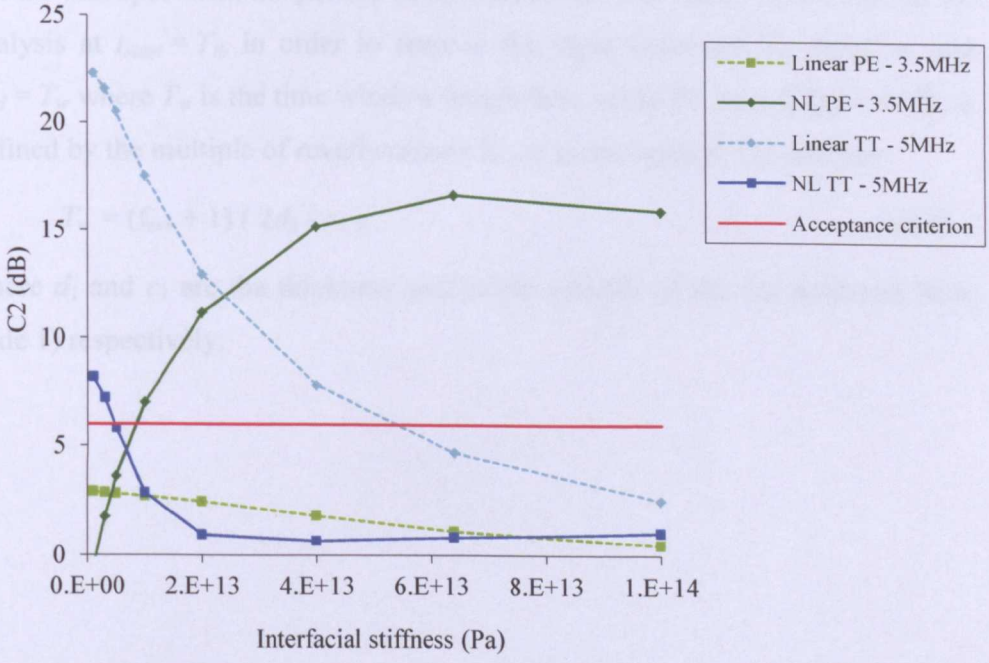

Figure 9.14. Figure of merit C_2 and absolute output amplitude change obtained for the thick specimen in contact PE at 3.5 MHz and in contact TT at 5 MHz for different KB stiffnesses

From the results plotted in Figure 9.14, it can be seen that when testing the thick specimen from side 1, KB with the weakest interfacial stiffnesses ($K_{LKB} < 2.5\times10^{13}$ Pa) would be better detected with linear measurements in contact TT at 5 MHz (light blue dotted line). However, for interfacial stiffnesses

from about 2.5×10^{13} Pa, nonlinear measurements in contact PE are more efficient than linear TT to detect KB (dark green solid line).

It should be noted that for nonlinear measurements, the difference between the cases with and without KB is significantly larger for PE than for TT where it is below acceptance level. In effect, the inherent material nonlinearities generated by the forward travelling wave are significantly reduced by those generated by the backward travelling wave due to phase inversion, but KB nonlinearities are still visible. In the case of perfect reflection (reflection coefficient R = 1) in an undamped material, the nonlinear component of the transmitted signal $-A_2 \sin(-2k(x-ct))$ would be reflected with respect to the ordinate axis with opposite signs (180° phase shift) and constant amplitude A_2. Material nonlinearities would therefore, in such a case, be cancelled out by the nonlinear component of the reflected signal [148].

For the thin specimen, the portion of the transmitted raw signal $u_{out}(t)$ was cut for analysis at $t_{start} = T_{tb}$ in order to remove the input toneburst T_{tb} duration, and $t_{end} = T_w$ where T_w is the time window length that, in the PE case (Figure 9.15), is defined by the multiple of reverberations f_{rev} to be included in the analysis:

$$T_w = (f_{rev} + 1)(2d_1 / c_1) \qquad (9\text{-}6)$$

where d_1 and c_1 are the thickness and sound velocity of the top adherend layer (side 1) respectively.

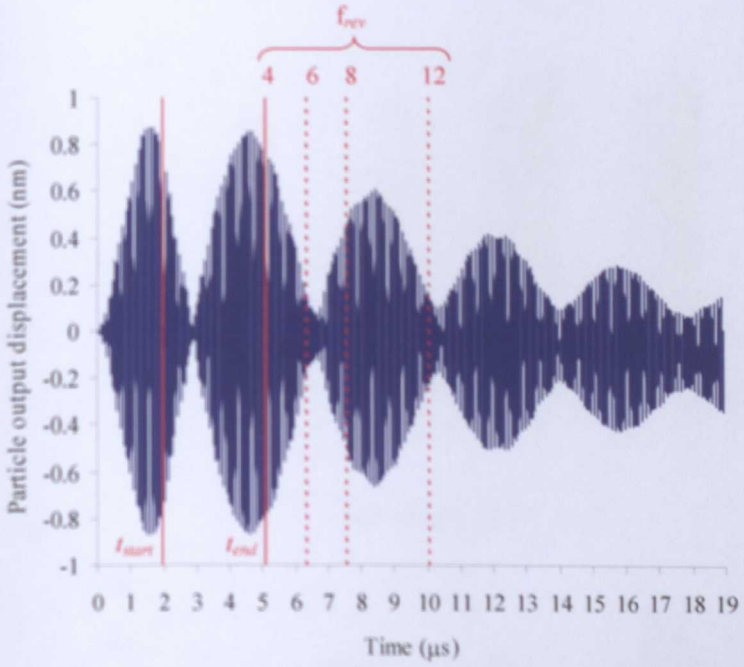

Figure 9.15. Example of time-domain PE signal for the thin specimen with cutting lines at t_{start} (to remove input signal) and t_{end} (to cut after the f_{rev}^{th} multiple reverberation of side 1)

Figures of merit were calculated for the output PE signal cut after the 4^{th}, 6^{th}, 8^{th} and 12^{th} multiple reverberations of side 1, and for the three driving frequencies 3.5, 5 and 10 MHz (Figure 9.16).

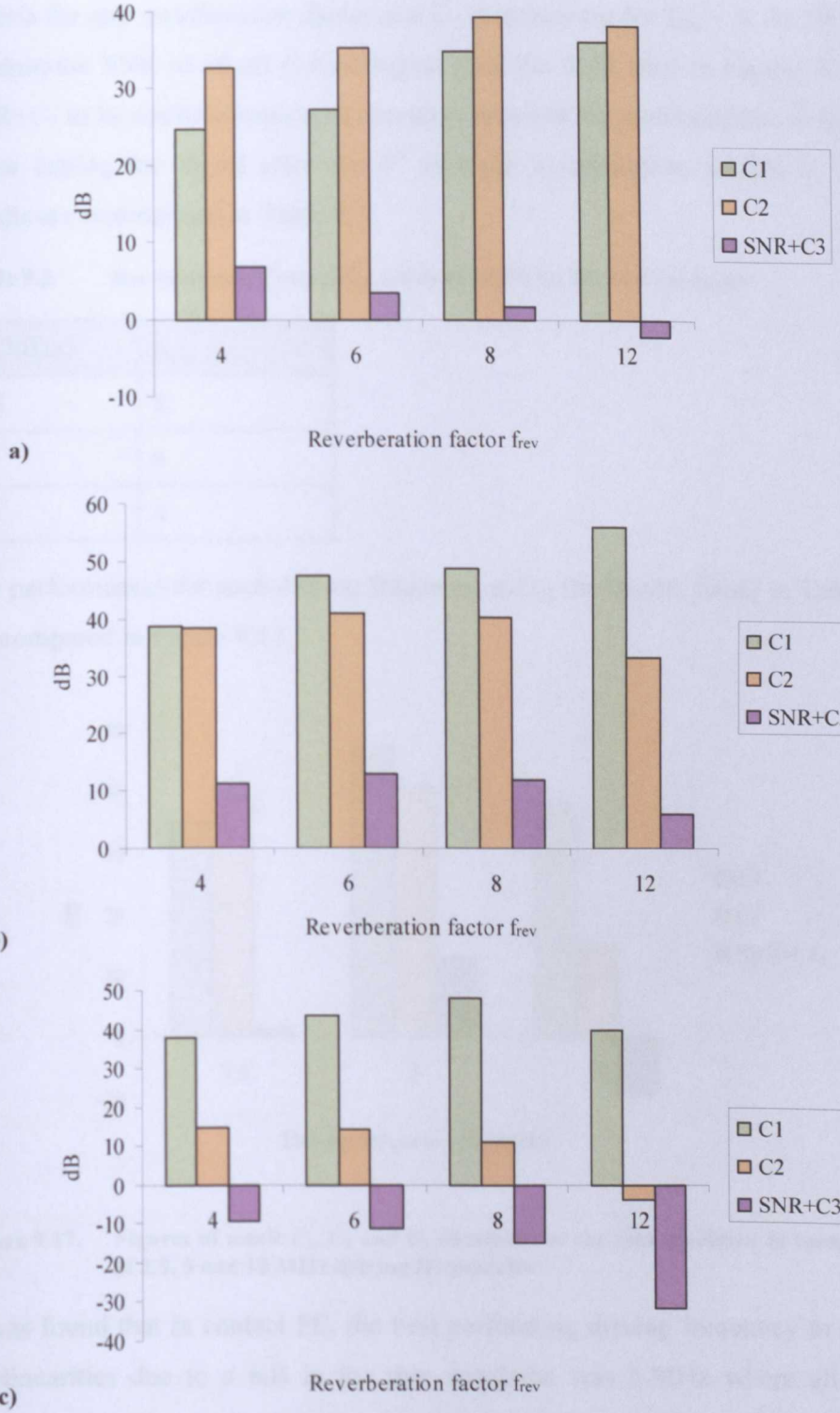

Figure 9.16. Figures of merit C_1, C_2 and C_3 obtained for different time window lengths at 3.5, 5 and 10 MHz driving frequencies — a), b) and c) respectively — when testing the thin specimen in contact PE where SNR = 46 dB

It can be seen in Figure 9.16 that for the 3.5 MHz driving frequency, C_2 rises with reverberations up to the 8th multiple but the acceptance criteria for C_3 is only achieved for $f_{rev} = 4$. At 5 MHz, the figures of merit fulfil the acceptance

criteria for any reverberation factor and C_2 is maximum for $f_{rev} = 6$. At 10 MHz, a minimum SNR of 60 dB (14 dB higher than the SNR used in Figure 9.16 for SNR+C_3 to be above acceptance criteria) is required for nonlinearities to be seen when cutting the signal after the 4th multiple reverberation of side 1. These results are summarised in Table 9.3.

Table 9.3. Recommended factors f_{rev} for contact PE on the thin specimen

f_0 (MHz)	f_{rev}
3.5	8
5	6
10	4

The performances for each driving frequency using the factors found in Table 9.3 are compared in Figure 9.17.

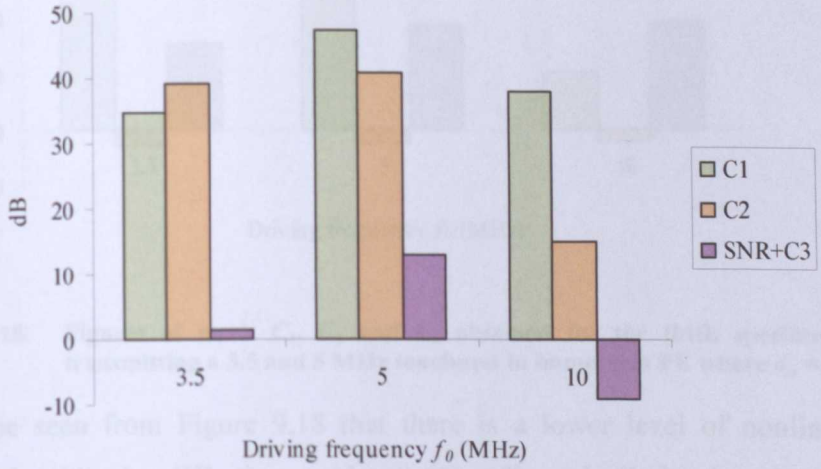

Figure 9.17. Figures of merit C_1, C_2 and C_3 obtained for the thin specimen in contact PE at 3.5, 5 and 10 MHz driving frequencies

It was found that in contact PE, the best performing driving frequency to detect nonlinearities due to a KB in the thin specimen was 5 MHz where all three figures of merit were above acceptance level as well as optimised (Figure 9.17). This might be due to the fact that when the driving frequency is close to the resonant frequency of the joint (about 4.5 MHz), nonlinearities generated by the KB are enhanced in contact PE.

9.7 Pulse-echo in immersion

Pulse-echo in immersion is the configuration of most importance for easy industrial application as it enables not only single-sided measurements but also scanning to be performed more easily than in through-transmission.

Pulse-echo was carried out in immersion for the thick specimen at 3.5, 5 and 10 MHz driving frequencies. The figures of merit are compared in Figure 9.18.

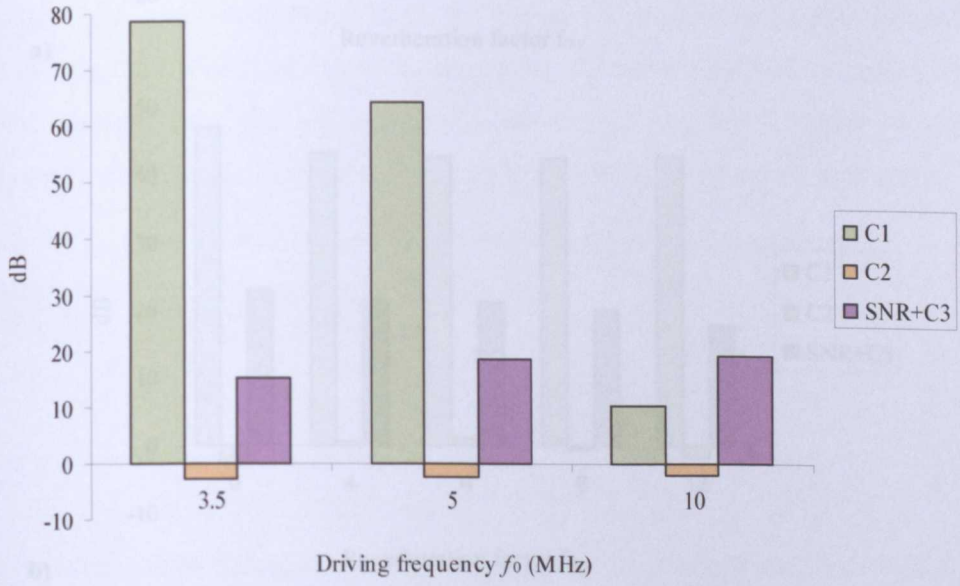

Figure 9.18. Figures of merit C_1, C_2 and C_3 obtained for the thick specimen when transmitting a 3.5 and 5 MHz toneburst in immersion PE where d_w = 10 mm

It can be seen from Figure 9.18 that there is a lower level of nonlinearities measured with the KB than without ($C_2 < 0$) and C_2 is therefore below acceptance level for all driving frequencies. This means that when the thick specimen is immersed in 10 mm of water, no difference between the cases with and without KB can be seen in PE.

For the thin specimen where the reflected signal could not be resolved, figures of merit were calculated for the output PE signal cut after the 4th, 6th, 8 and 12th multiple reverberations of side 1, and for the three driving frequencies 3.5, 5 and 10 MHz (Figure 9.19).

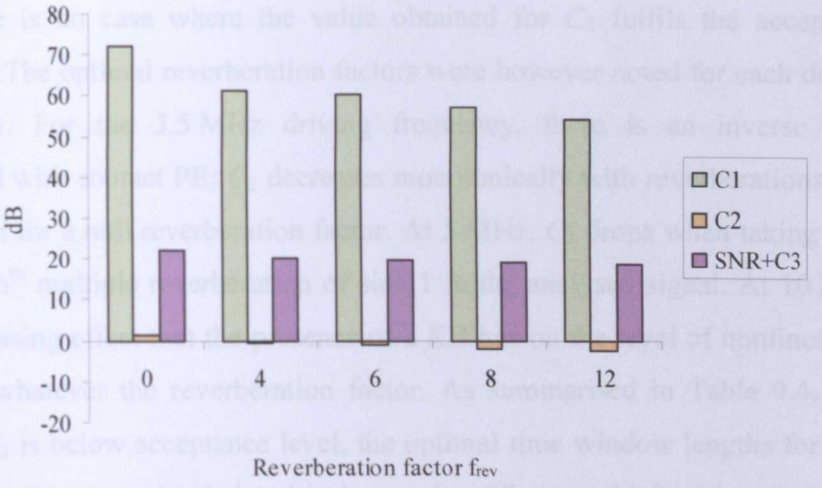

a)

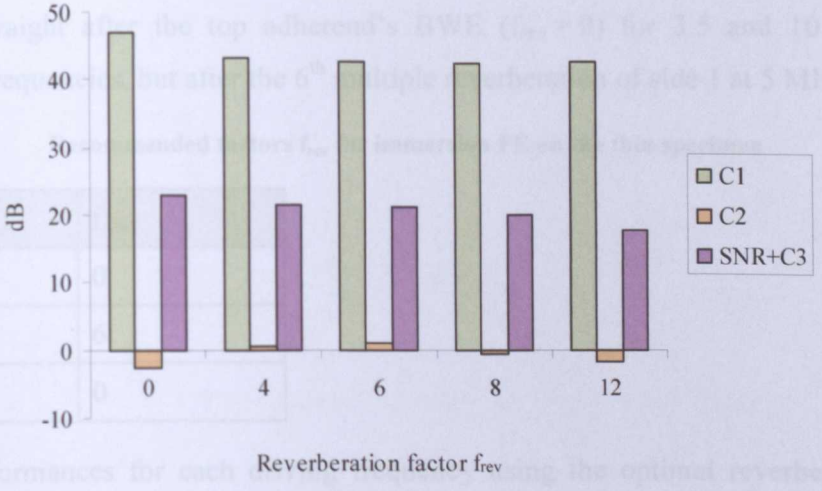

b)

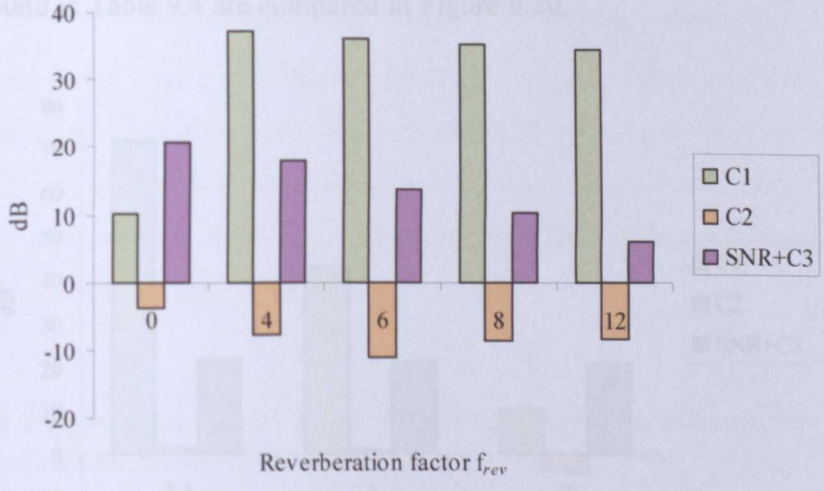

c)

Figure 9.19. Figures of merit C_1, C_2 and C_3 obtained for different time window lengths at 3.5, 5 and 10 MHz driving frequencies — a), b) and c) respectively — when testing the thin specimen in immersion PE where SNR = 46 dB

It should be noted that a null reverberation factor corresponds to taking for analysis the back wall echo (BWE) of side 1 only. It can be seen in Figure 9.19

that there is no case where the value obtained for C_2 fulfils the acceptance criterion. The optimal reverberation factors were however noted for each driving frequency. For the 3.5 MHz driving frequency, there is an inverse trend compared with contact PE: C_2 decreases monotonically with reverberations so is maximum for a null reverberation factor. At 5 MHz, C_2 drops when taking more than the 6th multiple reverberation of side 1 in the analysed signal. At 10 MHz, the decreasing effect that the presence of a KB has on the level of nonlinearities prevails whatever the reverberation factor. As summarised in Table 9.4, even though C_2 is below acceptance level, the optimal time window lengths for post-processing the transmitted signal in immersion PE were obtained by cutting the signal straight after the top adherend's BWE ($f_{rev} = 0$) for 3.5 and 10 MHz driving frequencies, but after the 6th multiple reverberation of side 1 at 5 MHz.

Table 9.4. Recommended factors f_{rev} for immersion PE on the thin specimen

f_0 (MHz)	f_{rev}
3.5	0
5	6
10	0

The performances for each driving frequency using the optimal reverberation factors found in Table 9.4 are compared in Figure 9.20.

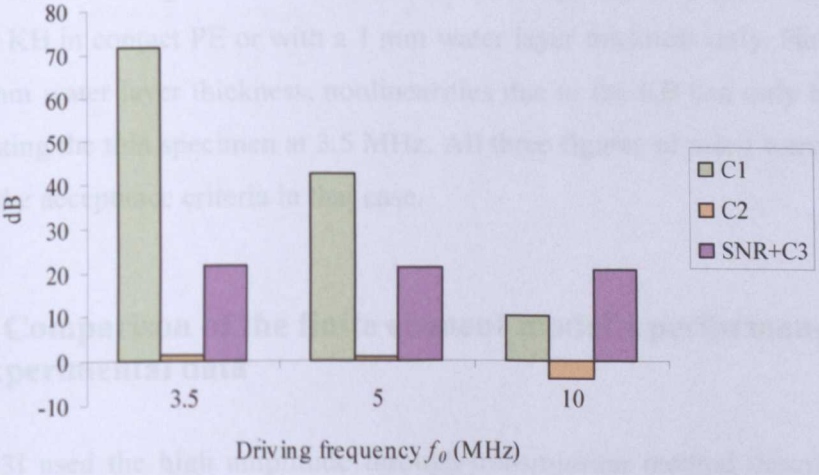

Figure 9.20. Figures of merit C_1, C_2 and C_3 obtained for the thin specimen in immersion PE at 3.5, 5 and 10 MHz driving frequencies

It was found that in immersion PE, the best performing driving frequency to detect nonlinearities due to a KB in the thin specimen was 3.5 MHz (C_2 maximum). However, the difference between the cases with and without KB would not be seen with a 10 mm water thickness ($C_2 < 6$dB). The program was therefore run again for the three driving frequencies but reducing the water layer thickness to see whether any nonlinearity due to the KB could be detected then (Figure 9.21).

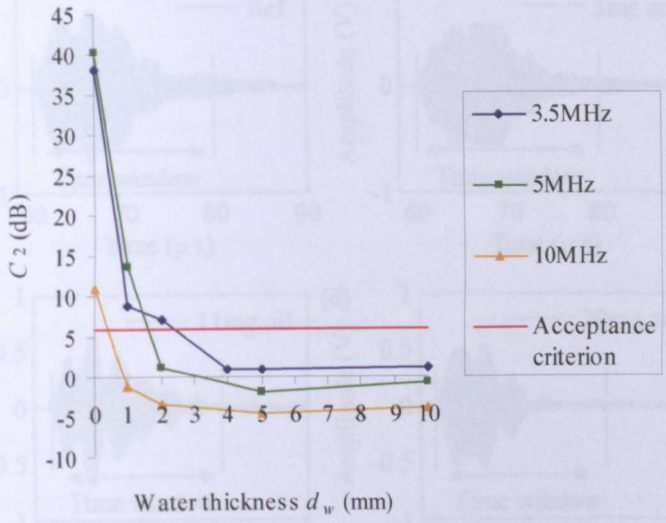

Figure 9.21. Figure of merit C_2 obtained for the thin specimen in immersion PE at 3.5, 5 and 10 MHz as a function of water layer thickness d_w

It can be seen from Figure 9.21 that the 5 MHz driving frequency performs better to detect KB in contact PE or with a 1 mm water layer thickness only. However, for a 2 mm water layer thickness, nonlinearities due to the KB can only be seen when testing the thin specimen at 3.5 MHz. All three figures of merit were found to fulfil the acceptance criteria in that case.

9.8 Comparison of the finite element model's performance with experimental data

Yan [153] used the high amplitude through-transmission method described in section 4.4 to test thin aluminium adhesive joints where oil was used to contaminate the bond area and create a region of poor bonding. This region of contamination is referred to as a liquid layer kissing bond. These sandwich

specimens consisted in layers of aluminium, epoxy and aluminium of 4, 0.2 and 2 mm respectively. Reference specimens were manufactured without contamination and the liquid layer specimens were contaminated with varying levels of lubrication oil — 3, 11 and 30 mg which corresponded to 3.7, 13.6 and 37 μm average contaminant thicknesses respectively. The time and frequency domain signals obtained for the pristine and contaminated specimens are plotted in Figure 9.22 and Figure 9.23 respectively.

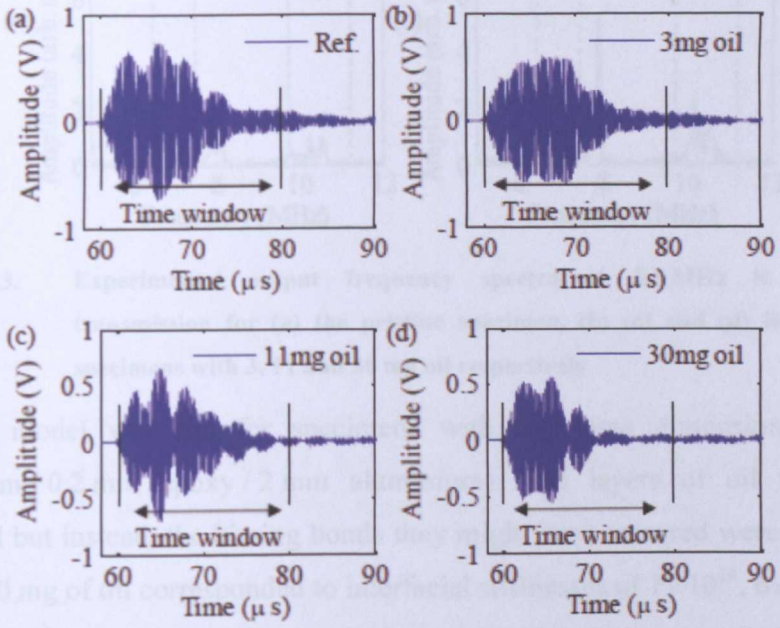

Figure 9.22. **Experimental output signal at 3.5 MHz in through-transmission for (a) the pristine specimen, (b) (c) and (d) liquid layer specimens with 3, 11 and 30 mg oil respectively**

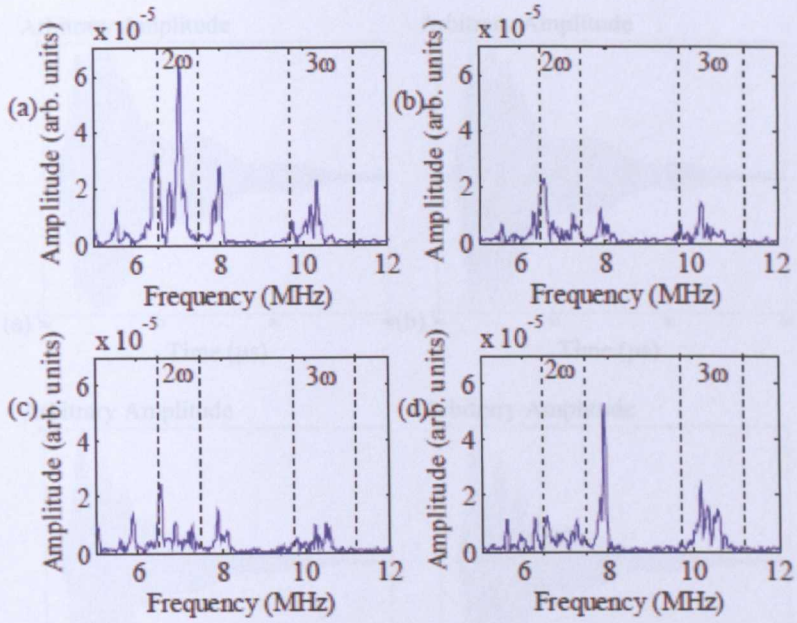

Figure 9.23. **Experimental output frequency spectra at 3.5 MHz in through-transmission for (a) the pristine specimen, (b) (c) and (d) liquid layer specimens with 3, 11 and 30 mg oil respectively**

The FE model was run for specimens with the same dimensions (4 mm aluminium / 0.2 mm epoxy / 2 mm aluminium). The layers of oil were not modelled but instead, the kissing bonds they might have incurred were where 3, 11 and 30 mg of oil corresponded to interfacial stiffnesses of 1×10^{14}, 6×10^{13} and 3×10^{13} N/m^3 respectively. The level of nonlinearities from external sources as well as noise were included in the simulation by setting A_{NL} at 1.5×10^{4} and by adding to the input signal a random signal with 0.01 standard deviation (see Chapter 8). In a similar way the signal of amplitude A_{NL} at twice the driving frequency was added to the input signal, another signal at three times the driving frequency of amplitude 5×10^{2} was also added in order to match Yan's results for the pristine specimen. The time and frequency domain signals obtained are plotted in Figure 9.24 and Figure 9.25 respectively.

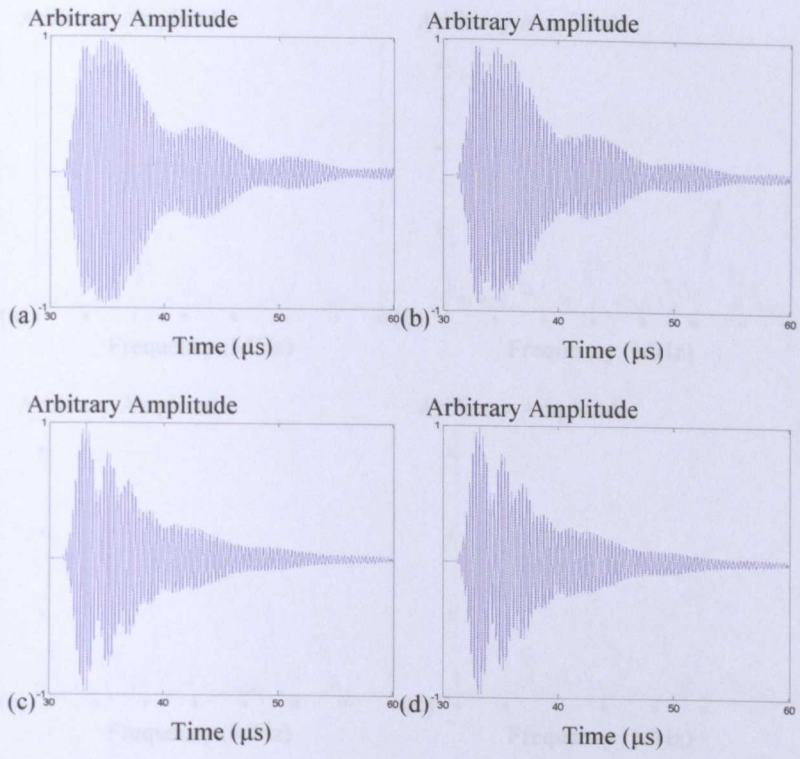

Figure 9.24. **Simulated output signal at 3.5 MHz in through-transmission for (a) the pristine specimen, (b) (c) and (d) kissing bond specimens with 1×10^{14}, 6×10^{13} and 3×10^{13} N/m^3 interfacial stiffnesses respectively**

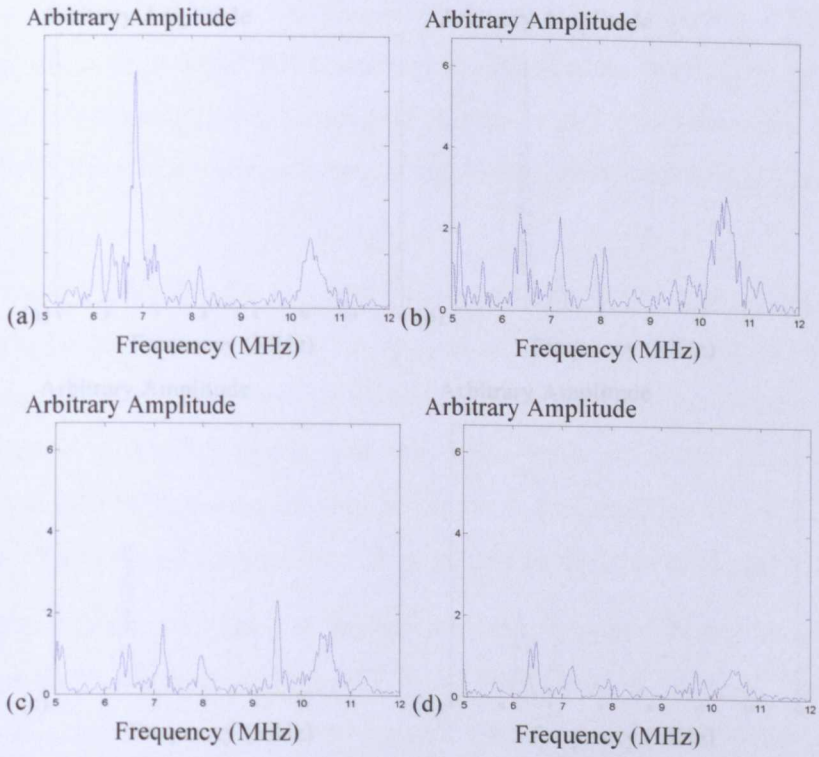

Figure 9.25. Simulated output frequency spectra at 3.5 MHz in through-transmission for (a) the pristine specimen, (b) (c) and (d) contaminated specimens with 1×10^{14}, 6×10^{13} and 3×10^{13} N/m^3 interfacial stiffnesses respectively — including noise

When comparing measured and simulated time domain signals from Figure 9.22 and Figure 9.24, the differences in envelope shape is probably due to the increasing amount of oil that was not included in the simulation but also to a varying adhesive layer thickness in the experiment [153].

The frequency spectra of these signals seen in Figure 9.23 and Figure 9.25 have peaks around the same frequencies: the pristine specimen shows a higher peak at the second harmonic with also higher amplitudes around 6.7, 8 and 10.5 MHz. The peak around 6.7 MHz corresponds to the resonance frequency of the bond which is very close to the second harmonic. It can be seen that the energy of the second harmonic transfers to the resonant frequency resulting in an increasing amplitude at the resonance frequency with increasing contamination level at the interface. To better understand frequency component behaviour with increasing contamination and therefore decreasing interfacial stiffness, the model was run without simulating noise. The results are plotted in Figure 9.26.

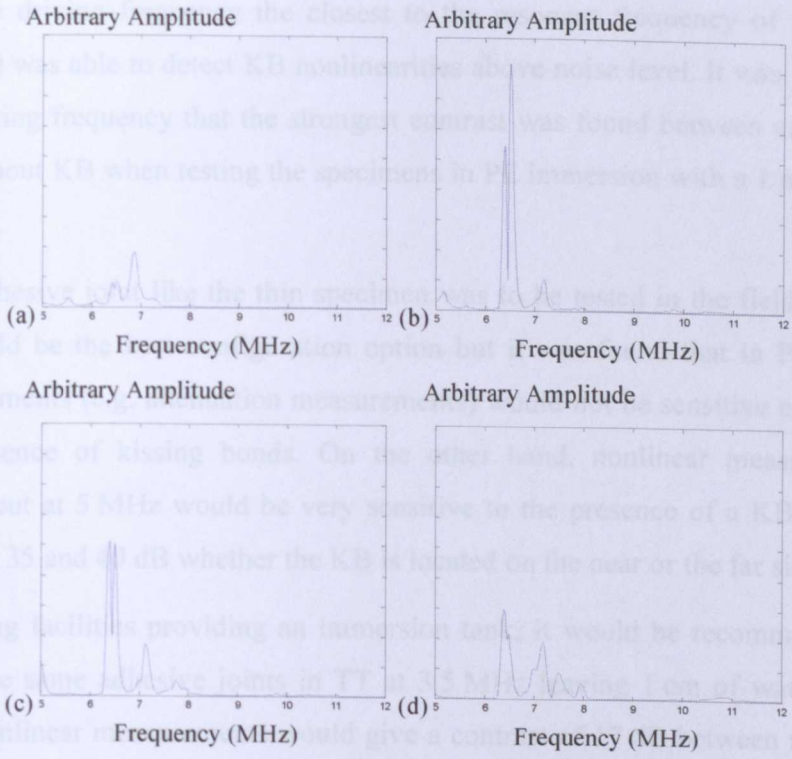

Figure 9.26. Simulated output frequency spectra at 3.5 MHz in through-transmission for (a) the pristine specimen, (b) (c) and (d) contaminated specimens with 1×10^{14}, 6×10^{13} and 3×10^{13} N/m^3 interfacial stiffnesses respectively — without noise

It can be seen in Figure 9.26 that for a 1×10^{14} interfacial stiffness, the resonance frequency peak is maximum and the second harmonic amplitude has decreased compared with the pristine specimen. Also, amounts of energy around 8 and 10.5 MHz are increasing with decreasing interfacial stiffness which confirms the trend seen in the experimental data. It should however be noted that the algorithm developed for this FE model approximates nonlinear wave propagation up to the second order only and would therefore require additional terms in the calculations in order to model the effects at the third harmonic.

9.9 Summary and prospects for development into an inspection technique

When carrying out the case study here above, it was found that in TT a lower driving frequency (3.5 MHz) was better at detecting KB, mainly because KB detection could be achieved with lower SNR. In contact PE on the other hand,

only the driving frequency the closest to the resonant frequency of the bond (5 MHz) was able to detect KB nonlinearities above noise level. It was also with this driving frequency that the strongest contrast was found between cases with and without KB when testing the specimens in PE immersion with a 1 mm water distance.

If an adhesive joint like the thin specimen was to be tested in the field, contact PE would be the best configuration option but it was found that in PE, linear measurements (e.g. attenuation measurements) would not be sensitive enough to the presence of kissing bonds. On the other hand, nonlinear measurements carried out at 5 MHz would be very sensitive to the presence of a KB with C_2 between 35 and 40 dB whether the KB is located on the near or the far side.

At testing facilities providing an immersion tank, it would be recommended to test these same adhesive joints in TT at 3.5 MHz leaving 1 cm of water either side. Nonlinear measurements would give a contrast of 17 dB between the cases with and without a KB whereas less than 1 dB difference in amplitude would be found with linear measurements.

When looking at both the case study results and Yan's experimental data [153], what came to light is the complexity of the results compared to linear non-destructive testing (NDT). There is a vast parameter space of possible configurations, driving frequency, etc. of which only a relatively small number of points were, quite reasonably, probed here. The unpredictability of what happens at these points means that it is very hard if not impossible to guess what happens in-between. There is therefore at present insufficient data to form generic rules and the model remains an essential tool for trying out specific configurations to see what happens.

Using the FE model for optimisation could therefore enable engineers to carefully choose the parameters such as input voltage and driving frequency as well as the appropriate post-processing method to increase the chances of detecting defects exhibiting nonlinear behaviour. The way the FE model developed by the author could be used in industry would be by either incorporating it into an existing software such as ANDSCAN® that provides simulation capabilities, or by developing it into its own stand-alone software. A

metric such as change in attenuation would always be calculated alongside the nonlinear figures of merit in order to compare the performance of linear against nonlinear ultrasonic measurements.

Chapter 10

Conclusions

10.1 Introduction

The work in this thesis involved finding a Non-Destructive Evaluation (NDE) technique that can detect kissing bonds (KB) in adhesive joints. The focus was on nonlinear ultrasonic inspection. A new prediction tool was developed to assess the detection capability of nonlinear ultrasonic inspection for KB.

10.2 Review of thesis

First, a literature review of existing NDE techniques for testing adhesive joints at the bond line was carried out. These included radiography, nuclear magnetic resonance imaging (NMRI), thermography, holography, shearography, acoustic and ultrasonic methods. It was found that ultrasonic methods remain the most common inspection methods for adhesive joints and can be divided into linear and nonlinear methods.

Linear ultrasonic inspection techniques were carried out on lap-joint bond specimens for Sandia National Laboratories. The specimens had been prepared using specific methods proven to produce various levels of weak bonds such as the use of contaminants and the reduction of bond areas. Their estimated bond strengths were determined by multiple strength tests on similar specimens so that the various NDE measurements could be compared in terms of their relation to the actual structural integrity of the joint.

The only linear technique amongst double through-transmission (DTT), pulse-echo (PE), ultrasonic spectroscopy, shear wave resonance and oblique incidence that showed significant correlation between measured output signal amplitudes and bond strength was DTT. It was however noted that for adhesive failure

specimens, the decrease in amplitude could be due to increasing contaminant thickness rather than the presence of kissing bonds.

The harmonics generation technique, which is based on nonlinear ultrasonics, was therefore investigated to see whether additional information could be obtained at the bond line. When carrying out this nonlinear ultrasonic technique on the same sets of contaminated adhesive joints, a slightly stronger linear correlation was found between nonlinear ratio and bond strength for the specimens providing for adhesive failure. This suggested that nonlinear ultrasonics have the potential to detect kissing bonds.

In order to establish the prospects of this nonlinear technique in the context of adhesive joints, it was necessary to simulate the response of nonlinear multilayer structures to ultrasound. A one-dimensional (1-D) finite element (FE) model was developed from a mathematical discretisation of the elastic continuum to simulate nonlinear ultrasonic wave propagation. It could be visualised as a load of oscillating masses connected by elastic springs. This FE model was verified and validated for linear wave propagation against an input impedance model and experimental data respectively. For nonlinear wave propagation, the model was verified by extracting the correct nonlinear parameter value for material inherent nonlinearity following the same process as used experimentally.

Carefully controlled experiments were carried out to properly identify and quantify nonlinearities generated by external sources which were then incorporated into the model. With an immersed through-transmission (TT) configuration for example, these nonlinearities can be generated by the electronic equipment (waveform generator, power amplifier, pre-amplifier), the transducers (both transmitter and receiver), the cables and water.

Finally, the model was used as a prediction tool giving insights into the measurement scenario from which optimum measurement methodologies and appropriate signal processing procedures could be derived and combined to produce a tractable technique for quantitative measurement of kissing bonds. It was also possible to compare the FE model output against experimental data.

10.3 Summary of findings

The general experimental procedure was (1) to use one transducer to excite ultrasonic waves in the adhesive joint of interest over a limited frequency bandwidth, (2) measure the response of the joint using either the same or a second transducer, (3) analyse the frequency content of the received signal by calculating the nonlinear ratio $\Phi = A_2/A_1^2$ where A_1 and A_2 are the fundamental frequency and second harmonic amplitudes respectively. Cases considered included TT in a single layer of material as well as contact and immersion TT and PE in multi-layered structures (sandwich specimens made from aluminium and epoxy). All measurements were normal incidence unfocused ultrasonic measurements. Only single excitation was considered as opposed to non-collinear and other methods that involve mixing between signals [155]. The adhesive joints were modelled as 1-D planar systems.

10.3.1 Input signal requirements

To optimise the chances of defect induced nonlinearities to be seen in the output frequency spectrum, a continuous sinusoidal wave would in theory be the ideal input signal as its frequency spectrum has precisely zero amplitude at all frequencies other than the fundamental. However, such an ideal signal cannot be used in PE mode as this would mean receiving at the same time as transmitting, nor can it be used in practice at the voltage levels required (about 100 Volts) without damaging the equipment. These considerations required therefore for the input signal to be limited in time which can be achieved by simply cutting it. To minimise the side lobes in the frequency spectrum that will be generated as a result of the cutting, a window function should be applied. It was found that the Hanning window was the most efficient at reducing the level of side lobes. Also, the integral of the resulting input toneburst should be null to avoid any shifting in the signal.

10.3.2 How to recover the nonlinear parameter β

It was found that the absolute nonlinear parameter value β characterising inherent material nonlinearity can only be recovered in TT, when extracting the transmitted toneburst with a rectangular window over several propagation distances, and by performing a series of scalings.

The formula generally found in literature to calculate β is only valid when sending a continuous sine wave in an undamped material where no other nonlinearities than those generated by the material are taken into account. As this is rarely the case, the value for nonlinear ratio Φ over propagated distance x should in fact be calculated as the gradient of nonlinear ratios over distances. β should also be multiplied by scaling factors to account for the windowed input signal, the damping and any scaling applied by the particular FFT implementation used.

The correct absolute value for β can therefore be calculated for an input toneburst of finite length and a slightly damped material using the gradient of nonlinear ratio against propagation distance Φ/x as follows:

$$\beta = \frac{r_w r_d}{r_s} \frac{8}{k^2} \frac{\Phi}{x} \tag{6-12}$$

where r_w is the window ratio, r_d is the damping factor, r_s is the FFT scaling factor and k is the wavenumber.

10.3.3 Model optimisation

The FE model that was developed by the author was coded in Matlab and provides not only a better understanding of nonlinear wave propagation in multilayer structures but also a tangible resource useful to research engineers.

When running the FE model, it was found that convergence was achieved from 30 points per wavelength with a time step Δt equals to $\sqrt{2}/2\ \Delta x$ the element size.

It was also found that a minimum of 8192 points in the frequency domain enabled the frequency step to be small enough and hence the values taken for A_1

and A_2 to have abscissa values close enough to the fundamental frequency f_0 and the second harmonic $2f_0$.

An input toneburst with 20 cycles was found acceptable and the input acoustic pressure was found to be optimal at 1×10^{-5} K_2 where K_2 is the bulk modulus of the material under inspection.

With the parameters mentioned here above, the solution to the algorithm (model output) did not converge any faster using the fifth-order polynomial fit (five point method) when calculating the gradient of the displacement u with respect to spatial position x. It was therefore recommended to use the three point method for a faster running time.

Finally, it was found that the post-processing technique had an impact on the resulting nonlinear ratios calculated. The extraction window type that most reduced the generation of side lobes was the Hanning window. The optimal extraction time window length depends on the layer thicknesses and driving frequency.

10.3.4 Optimal experimental configuration

To detect a KB in a thin metallic sandwich specimen in TT, it was recommended to use a lower driving frequency (3.5 MHz) as well as maximising the post-processing time window length of the output signal. In contact PE or immersion PE with only 1 mm of water, the driving frequency the closest to the resonant frequency of the joint was recommended. However, in immersion PE with a 2 mm water layer, higher contrast between the cases with and without a KB was achieved at the lower frequency (3.5 MHz).

10.4 Future work

When assessing the integrity of adhesive joints in industry, the focus should be on one-sided ultrasonic techniques. Pulse-echo and pitch-catch modes would be good configurations to send longitudinal and shear waves into the structure. The received signals would then be analysed linearly in both time and frequency domains. To complement these linear measurements, nonlinear measurements in

the frequency domain would provide additional information if defects with nonlinear behaviour such as kissing bonds were present. These measurements require higher input voltage and nonlinearities generated by external sources would need to be carefully controlled in order to discriminate them from defect induced nonlinearities. This can be difficult to achieve experimentally and the FE model should be an efficient tool to make sure the optimum parameters are chosen. Small variations in couplant thickness might also occur and can be overcome by either fixing the transducer(s) or by taking the average of several measurements.

For shear wave propagation to be simulated as well, the FE model could be developed into a two-dimensional model (2-D). The work that was carried out here would be easily transferable and could possibly be performed in suitable commercial FE packages. In effect, with this new 1-D FE model, the rigour on relating measurements back to material properties was developed by identifying all the subtleties for qualitative measurements such as the use of scaling factors.

However, the complexity of the results found from the 1-D model when carrying out the case study in Chapter 9 showed how the huge parameter space of possible 1-D configurations has only just been touched on and the situation is by no means fully understood. There is therefore a lot more that could and should be done with just the 1-D model to gain more understanding of nonlinear ultrasonic wave propagation and its interaction with KB before developing the 2-D version.

The FE model could be used on other types of material such as composites which are increasingly being used in the aerospace industry. This new prediction tool would enable engineers to determine the optimal driving frequency as well as input voltage when testing such attenuative materials.

The FE model could also be expanded to include other types of defect that might be present in the adhesive joint. Their effect on nonlinear measurements could then be assessed. Porosity in the adhesive could be modelled by changes in its stiffness and density properties. Corrosion on the outer surface of the specimen could be simulated by setting the first element of the adherend layer to a lower density.

By following the recommendations given by the model, further experimental work could be carried out to enhance the existing nonlinear measurement technique. As the nonlinear high frequency transmission technique currently consists in gluing a piezoelectric disc either side of the specimen for contact TT [7], the signal could be transmitted by a conventional commercial transducer. Pulse-echo mode could be used, as well as immersion testing for scanning. All of these would be done by minimising nonlinearities due to external sources. For these experimental measurements, work would also be required to produce reliable and repeatable KB in adhesive joints [156].

There are also other existing nonlinear set-ups and input signals to consider. For example, a signal with two different frequency tonebursts superposed could be used (possibly excited with two different transducers, one on either side of the specimen) and the mixing between them would be looked for – in this way, one frequency could always be tuned to match a resonance in the adhesive and the sensitivity would be maximised as a result.

Other input signals to consider include chirps, Golay codes, random signals (e.g. Gaussian white noise) and chaotic signals.

In effect, improvement of the time reversal (TR) nonlinear elastic wave spectroscopy (NEWS) method [98] was achieved when using chirp-coded excitation [157] in the 400-600 kHz range. Signal-to-noise ratio (SNR) was increased and the extraction of the nonlinear signature derived from the scatterers was improved with the ability to separate second order harmonic components regardless of the transmitted bandwidth.

Complementary sequences introduced by Golay [158] belong to a family of signals which consist of two binary sequences of the same length n whose auto-correlation functions have side lobes equal in magnitude but opposite in sign. The sum of these auto-correlation functions gives a single auto-correlation function with the peak of $2n$ and zero elsewhere. Golay-coded excitation allows therefore the amplitude of side lobes to be suppressed to zero [159] as well as SNR to be increased [160][161].

If a Gaussian signal operates on a linear system, the resulting output will be Gaussian. Conversely, if the system is nonlinear, the output will result as non-

Gaussian. Since all the spectra of order higher than two are equal to zero for a Gaussian process, bispectral analysis can extract information regarding deviations from gaussianity, i.e. deviations from linearity of the system [162].

Finally, to be better able to characterise the nature of a particular nonlinearity and obtain more information about the defect, ideas from the nonlinear dynamics field could be applied to the development of a novel approach to nonlinear NDE. One important idea is that, where there is nonlinearity, there may be chaos, and techniques for characterising chaotic systems are well developed in other fields such as dynamics. The mathematical concept is that a chaotic system is one which is highly sensitive to the initial conditions, the classic example being weather patterns. This concept could be applied to the NDE of engineering structures and a powerful new approach developed.

The use of chaotic signals in radar and sonar was taken up by QinetiQ in 2001, looking specifically at the potential for enhancing detection (this is an analogous problem to that encountered in detecting defects using ultrasonic NDE). In 2002, QinetiQ proposed novel processing architectures for detecting chaotic signals. Two solutions were offered – detection by comparing the observed data with bifurcation diagrams (these describe the nature of the nonlinearity of a system) using target range as a parameter, and range estimation using "anticipating synchronisation". Later investigation concluded that they had limited usefulness in radar and sonar. NDE systems work on similar principles, but offer greater scope for the use of nonlinear dynamics both because of the more controlled environment, and the existence of nonlinear behaviour in practically important cases. Furthermore, chaotic signals are already being used in Structural Health Monitoring (SHM) where output between pristine and damaged structures are compared [163][164].

References

[1] L. Dorn, *Adhesive Bonding - Terms and Definitions*. Berlin, Technische Universität, 1994.

[2] F. C. Campbell, *Manufacturing Processes for Advanced Composites*. Elsevier, 2004.

[3] P. B. Nagy, "Ultrasonic detection of kissing bonds at adhesive interfaces", *J. Adhesion Sci. and Technology*, vol. 5, no. 8, pp. 619-630, 1991.

[4] P. B. Nagy, "Ultrasonic classification of imperfect interfaces", *J. Nondestructive Evaluation*, vol. 11, no. 3-4, pp. 127-139, 1992.

[5] O. Buck, W. L. Morris, and J. N. Richardson, "Acoustic harmonic-generation at unbonded interfaces and fatigue cracks", *Appl. Physics Lett.*, vol. 33, no. 5, pp. 371-373, 1978.

[6] S. Biwa, S. Nakajima, et al., "On the acoustic nonlinearity of solid-solid contact with pressure-dependent interface stiffness", *J. Appl. Mechanics*, vol. 71, no. 4, pp. 508-515, 2004.

[7] D. Yan, S. A. Neild and B. W. Drinkwater, "Modelling and measurement of the nonlinear behaviour of kissing bonds in adhesive joints", *NDT&E Int.*, vol. 47, pp. 18-25, 2012.

[8] D. Yan, B. W. Drinkwater, et al., "Measurement of the ultrasonic nonlinearity of kissing bonds in adhesive joints", *NDT&E Int.*, vol. 42, no. 5, pp. 459-466, 2009.

[9] S. Biwa, S. Hiraiwa, et al., "Evaluation of linear and nonlinear ultrasonic response of contacting surfaces", in *The Mechanical Behaviour of Materials X Part 1: 10th Int. Conf. Mechanical Behaviour of Materials*, Busan, Corea, 2007, pp. 1315-1318.

[10] C. J. Brotherhood, B. W. Drinkwater, et al., "The detectability of kissing bonds in adhesive joints using ultrasonic techniques", *Ultrasonics*, vol. 41, no. 7, pp. 521-529, 2003.

[11] S. Hirsekorn, U. Rabe and W. Arnold, "Characterization and Evaluation of Composite Laminates by Nonlinear Ultrasonic Transmission Measurements", in *ECNDT Conf. Proc.*, Berlin, Germany, 2006.

[12] K. Van Den Abeele, T. Kathowski, and C. Mattei, "Nonlinear acoustic and ultrasonic NDT of aeronautical components" in *Proc. Innovations in Nonlinear Acoust.: 17th Int. Symp. on Nonlinear Acoust.*, State Coll., PA, (18–22 July 2005), pp. 75–78.

[13] M. Meo, U. Polimeno, et al., "Detecting damage in composite material using nonlinear elastic wave spectroscopy methods", *Appl. Composite Materials*, vol. 15, no. 3, pp. 115-126, 2008.

[14] J. Ha and K. Y. Jhang, "Nonlinear ultrasonic method to detect micro-delamination in electronic packaging", *Key Eng. Materials*, vol. 297-300 II, pp. 813-818, 2005.

[15] I. E. Dekalo, V. V. Palachev, et al., "Effect of microcracks on the linear and non-linear acoustic properties of a bismuth based high temperature superconductor", *Russian Ultrasonics*, vol. 23, no. 6, pp. 333-336, 1993.

[16] S. U. Faßbender and W. Arnold, "Measurement of adhesion strength of bonds using nonlinear acoustics", *Rev. Progr. QNDE 1995*, Plenum Press, New York, vol. 15, pp. 1321-1328, 1996.

[17] C. Bockenheimer, D. Fata, W. Possart, M. Rothenfußer, U. Netzelmann and H. Schäfer, "The method of non-linear ultrasound as a tool for the non-destructive inspection of structural epoxy-metal bonds - A resume", *Int. J. Adhesion & Adhesives*, vol. 22, pp. 227–233, 2002.

[18] S. Hirsekorn, A. Koka, A. Wegner and W. Arnold, "Quality assessment of bond interfaces by nonlinear ultrasonic transmission", *Rev. Progr. QNDE 1999*, Plenum Press, New York, vol. 19B, pp. 1367-1374, 2000.

[19] S. Hirsekorn, "Nonlinear transfer of ultrasound by adhesive joints - a theoretical description", *Ultrasonics*, vol. 39, pp. 57–68, 2001.

[20] S. Hirsekorn, A. Koka, S. Kurzenhäuser and W. Arnold, "Calibration and Evaluation of Nonlinear Ultrasonic Transmission Measurements on Thin Bonded Interfaces", *Adhesion – Current Research and Applicat.*, Wulff Possart Ed., WILEY-VCH, Weinheim, Berlin, pp. 403-419, 2005.

[21] P. P. Delsanto, S. Hirsekorn, et al., "Modeling the propagation of ultrasonic waves in the interface region between two bonded elements", *Ultrasonics*, vol. 40, pp. 605-610, 2002.

[22] J. D. Achenbach and O. K. Parikh, "Ultrasonic analysis of nonlinear response and strength of adhesive bonds", *J. Adhesion Sci. and Technology*, vol. 5, no. 8, pp. 601-618, 1991.

[23] W. Arnold, "Non-linear acoustics and adhesion measurements of interfaces: Techniques for the inspection of bonded structures", in *Proc. 1997 IEE Colloq. Techniques for the Inspection of Bonded Structures*, no. 8, pp. 4/1-4/4, 1997.

[24] Y. Dun, X. Shi, et al., "Nondestructive evaluation of adhesive interfaces in MMCS using nonlinear ultrasonic method", *China Mech. Eng.*, vol. 19, no. 19, pp. 2351-2354, 2008.

[25] Y. Dun, X.-H. Shi, et al., "Ultrasonic nondestructive evaluation on bond quality of SRM interface based on second harmonic technique", *J. Solid Rocket Technology*, vol. 31, no. 2, pp. 198-200, 2008.

[26] K. Kawashima, M. Murase, et al., "Nonlinear ultrasonic imaging of imperfectly bonded interfaces", *Ultrasonics*, vol. 44, pp. 1329-1333, 2006.

[27] B. O'Neill, R. G. Maev, et al., "Application of theoretical models of nonlinear boundaries to the investigation of adhesive bonding conditions", in *Proc. IEEE Ultrasonics Symp.*, vol. 1, pp. 701-708, 2001.

[28] B. E. O'Neill and R. G. Maev, "Application of a nonlinear boundary condition model to adhesion interphase damage and failure", *J. Acoustical Soc. of America*, vol. 120, no. 6, pp. 3509-3517, 2006.

[29] M. Rothenfusser, M. Mayr, et al., "Acoustic nonlinearities in adhesive joints", *Ultrasonics*, vol. 38, pp. 322-326, 2000.

[30] S. I. Rokhlin, L. Wang, et al., "Frequency modulated dual angle ultrasonic spectroscopy of adhesive bonds", in *Proc. Forum Acoust. Budapest 2005: 4th European Congr. Acoust.*, 2005, pp. 1363-1368.

[31] J. L. Rose and P. A. Meyer, "Ultrasonic procedures for predicting adhesive bond strength", *Materials Evaluation*, vol. 31, no. 6, pp. 109-114, 1973.

[32] Z. Tang, A. Cheng, et al., "Ultrasonic evaluation of adhesive bond degradation by detection of the onset of nonlinear behavior", *J. Adhesion Sci. and Technology*, vol. 13, no. 7, pp. 837-854, 1999.

[33] S. I. Rokhlin and M. Rosen, "An ultrasonic method for the evaluation of interface elastic properties", *Thin Solid Films*, vol. 89, no.2, pp. 143-148, Mars 1981.

[34] S. I. Rokhlin, L. Wang, , et al., "Modulated angle beam ultrasonic spectroscopy for evaluation of imperfect interfaces and adhesive bonds", *Ultrasonics*, vol. 42, no. 1-9, pp. 1037-1047, April 2004.

[35] K. Van Den Abeele, K. Van De Velde and J. Carmeliet, "Inferring the degradation of pultruded composites from dynamic nonlinear resonance measurements", *Polymer Composites*, vol. 22, no. 4, pp. 555-567, 2001.

[36] F. H. Chang, P. L. Flynn, et al., "Principles and application of ultrasonic spectroscopy in NDE of adhesive bonds", in *IEEE Trans. Sonics and Ultrasonics*, vol. SU-23, no. 5, pp. 334-338, 1976.

[37] A. O. K. Nieminen and J. L. Koenig, "NMR imaging of the interfaces of epoxy adhesive joints", *J. Adhesion*, vol. 30, no. 1-4, pp. 47-56, 1989.

[38] R. D. Adams and P. Cawley, "Review of defect types and nondestructive testing techniques for composites and bonded joints", *NDT Int.*, vol. 21, no. 4, pp. 208-222, 1988.

[39] R. D. Adams and B. W. Drinkwater, "Non-destructive testing of adhesively-bonded joints", *Int. J. Materials & Product Technology*, vol. 14. no. 5-6, pp. 385-398, 1999.

[40] P. Cawley and R. D. Adams, "Defect types and non-destructive testing techniques for composites and bonded joints", *Materials Sci. and Technology*, vol. 5, no. 5, pp. 413-425, 1989.

[41] P. Cawley, "Low frequency NDT techniques for the detection of disbonds and delaminations", *British J. Non-Destructive Testing*, vol. 32, no. 9, pp. 454-461, 1990.

[42] P. Cawley, "Ultrasonic measurements for the quantitative NDE of adhesive joints - Potential and challenges", in *Proc. Ultrasonics Symp.*, 1992, vol. 2, pp.767-772.

[43] P. Cawley and T. Pialucha, "Detection of a weak adhesive/adherend interface in bonded joints", in *Proc. Ultrasonics Int. Conf.*, Vienna, Austria, 1993, pp. 261-264.

[44] P. Cawley, "NDT of adhesive joints-current capabilities and future needs", in *IEE Colloq. Techniques for the Inspection of Bonded Structures*, London, UK, 1997, pp. 1.

[45] A. Cuc and V. Giurgiutiu, "Disbond detection in adhesively bonded structures using piezoelectric wafer active sensors", USA, SPIE-Int. Soc. Opt. Eng, 2004.

[46] D. J. Hagemaier, "Automated ultrasonic inspection of adhesive bonded structure", *Materials Evaluation*, vol. 40, no. 5, pp. 572-578, 1982.

[47] E. Y. Maeva, I. A. Severina, et al., in *Proc. IEEE Ultrasonics Symp.*, Honolulu, HI, 2003, vol. 2, pp. 2037-2040.

[48] R. J. Schliekelmann, "Non-destructive testing of adhesive bonded metal-to-metal joints. II", *Non-Destructive Testing*, vol. 5, no. 3, pp. 144-153, 1972.

[49] M. J. Davis, Bond D. A., "The Importance of Failure Mode Identification in Adhesive Bonded Aircraft Structures and Repairs", in *Proc. Int. Conf. Composite Materials 12*, Paris, France, 1999.

[50] R. E. Challis, R. J. Freemantle, J. D. H. White and G. P. Wilkinson, "Ultrasonic compression wave NDT of adhered metal lap joints of uncertain dimensions", *Insight*, vol. 37, no. 12, pp. 954-963, 1995.

[51] G. A. Alers, P. L. Flynn, et al., "Ultrasonic techniques for measuring the strength of adhesive bonds", *Materials Evaluation*, vol. 35, no. 4, pp. 77-84, 1977.

[52] G. J. Curtis, "Acoustic emission energy relates to bond strength", *Non-Destructive Testing*, vol. 8, no. 5, pp. 249-257, 1975.

[53] M. A. Drewry, "Assignment for the radiography course", University of Bristol, UK, April 2010.

[54] M. A. Drewry, "Thermographic inspection techniques for adhesive joints", University of Bristol, UK, July 2009.

[55] C. Thiemann, M. F. Zaeh, C. Srajbr and S. Boehm, "Automated defect detection in large-scale bonded parts by active thermography", in *10th Int. Conf. Quantitative InfraRed Thermography*, Québec, Canada, July 27-30, 2010.

[56] C. Meola, G. M. Carlomagno, et al., "The use of infrared thermography for nondestructive evaluation of joints", *Infrared Physics and Technology*, vol. 46, no. 1-2 spec. iss., pp. 93-99, 2004.

[57] J. A. Schroeder, T. Ahmed, et al., "Non-destructive testing of structural composites and adhesively bonded composite joints: Pulsed thermography", *Composites Part A: Appl. Sci. and Manufacturing*, vol. 33, no. 11, pp. 1511-1517, 2002.

[58] W. N. Reynolds, "Inspection of laminates and adhesive bonds by pulse-video thermography", *NDT Int.*, vol. 21, no. 4, pp. 229-232, 1988.

[59] J. Rantala, D. Wu, et al., "Amplitude-modulated lock-in vibrothermography for NDE of polymers and composites", *Research in Nondestructive Evaluation*, vol. 7, no. 4, pp. 215-228, 1996.

[60] L. D. Favro, H. Xiaoyan, et al., "Infrared imaging of defects heated by a sonic pulse", *Review of Scientific Instruments*, vol. 71, no. 6, pp. 2418-21, 2000.

[61] C. M. Vest, "Status and future of holographic non-destructive evaluation", SPIE 349, pp. 186-198, 1982.

[62] M. J. Marehaut, "Holographic interferometry for CFRP honeycomb panels", RAE-TR-73192, 1973.

[63] N. P. Enderherg, et al., "Establishment of non-destructive inspection techniques for honeycomb sandwich with carbon fibre composite face sheets by means of holographic methods", ESTEC Contract 1957/73, 1978.

[64] R. J. Querido, "New applications of holographic non-destructive testing of advanced composite materials in aerospace construction", in *11th World Conf. NDT*, 3-8 November 1985, pp 461-468.

[65] M. V. Rao, R. Samuel, et al., "Dual vacuum stressing technique for holographic nondestructive testing of honeycomb sandwich panels", *NDT Int.*, vol. 23, no. 5, pp. 267-270, 1990.

[66] Y. Y. Hung, W. D. Luo, et al., "Evaluating the soundness of bonding using shearography", *Composite Structures*, vol. 50, no.4, pp.353-362, 2000.

[67] P. Cawley and C. Theodorakopoulos, "The membrane resonance method of non-destructive testing", *J. Sound and Vibration*, vol. 130, no. 2, pp. 299-311, 1989.

[68] P. Cawley, "The sensitivity of the mechanical impedance method of nondestructive testing", *NDT Int.*, vol. 20, no. 4, pp. 209-215, 1987.

[69] R. A. Smith, V. L. Weise and R. P. Dalton, "Potential Advanced Ultrasonic Methods for Detection of Weak Adhesion", in *Proc. NDT2003, 42nd Annual Conf. of the British Institute of NDT*, 2003.

[70] S. A. Titov, R. G. Maev, et al., "Pulse-echo NDT of adhesively bonded joints in automotive assemblies", *Ultrasonics*, vol. 48, no. 6-7, pp. 537-546, 2008..

[71] A. Pilarski, "Coefficient of reflection of ultrasonic waves from adhesive bond interface", *Archives of Acoust.*, vol. 8, no. 1, pp. 41-53, 1983.

[72] J. K. Chambers and J. R.Tucker, "Bond line analysis using swept-frequency ultrasonic spectroscopy", *Insight – J. British Inst. NDT*, vol. 41, pp 151-155, 1999.

[73] V. L.Weise, J. R. Tucker, D. A. Bruce and R. A. Smith, "An initial investigation into the relationship between the material properties of adhesive joints and their ultrasonic properties", in *28th Review of Progress in Quantitative Nondestructive Evaluation*, D. O. Thompson and D. E. Chimenti, Eds. Melville, NY: American Institute of Physics, vol. 20B, pp. 1096-1102, 2001.

[74] J. Tucker, "Ultrasonic spectroscopy for corrosion detection and multiple layer bond inspection", in *Proc. 1st Joint DoD/FAA/NASA Aging Aircraft Conf.*, pp. 1537-1550, 1998.

[75] R. J. Schliekelmann, "Non-destructive testing of bonded joints: Recent developments in testing systems", *Non-Destructive Testing*, vol. 8, no. 2, pp. 100-103, 1975.

[76] D. C. Price and B. J.Martin, "Ultrasonic inspection of bonded metal plates using pulse-echo spectroscopy", *Non-Destructive Testing – Australia*, vol. 30, no. 5, Sep-Oct 1993.

[77] J. Krautkrämer and H. Krautkrämer, *Ultrasonic testing of materials*, London, Springer-Verlag, 1990.

[78] A. Pilarski and J. L. Rose, "Ultrasonic oblique incidence for improved sensitivity in interface weakness determination", *NDT Int.*, vol. 21, no. 4, pp. 241-246, 1988.

[79] N. J. Burton and D. M. Thaker, "Practical applications of acoustic microscopy in failure analysis", in *Proc. Int. Symp. Testing and Failure Analysis*, Torrance, CA, USA, 1985, pp. 187-192.

[80] Z. Yang, W. Zhang, Y. Tian, Z. Li, H. Zong, "Testing Application of Scanning Acoustic Microscope for Adhesive Characteristics of Explosive/Aluminum-Alloy Interface", in *Proc. 17th World Conf. Nondestructive Testing*, Shanghai, China, 2008.

[81] P. Zinin and W. Weise, "Theory and applications of acoustic microscopy", *Ultrasonic Nondestructive Evaluation: Eng. and Biological Material Characterization*, ch. 11, pp. 654-724, 2003.

[82] R. O. Claus and R. A. Kline, "Adhesive bond line interrogation using Stoneley wave methods", *J. Appl. Physics*, vol. 50, no. 12, pp. 8066-8069, 1979.

[83] A. K. Mal, P.-C. Xu, et al., "Leaky Lamb waves for the ultrasonic nondestructive evaluation of adhesive bonds", *J. Eng. Materials and Technology, Trans. ASME*, vol. 112, no. 3, pp. 255-259, 1990.

[84] M. A. Drewry, R. A. Smith, et al., "Ultrasonic Techniques for Detection of Weak Adhesion", *Materials Evaluation*, vol. 67, no. 9, pp.1048-1058, 2009.

[85] J. H. Cantrell and W. T. Yost, "Nonlinear ultrasonic characterization of fatigue microstructures", *Int. J. Fatigue*, vol. 23, suppl.issue, 2001.

[86] M. A. Breazeale and D. O. Thompson, "Finite-amplitude ultrasonic waves in aluminum", *Appl. Physics Lett.*, vol. 3, pp. 77-78, 1963.

[87] M. A. Breazeale and J. Philip, "Determination of third-order elastic constants from ultrasonic harmonic generation measurements", *Physical Acoust.*, vol. XVII, Eds. New York Academic Press: W. P. Mason and R. N. Thurston, 1984, ch.1, pp. 1-60.

[88] L. Adler, "Second order acoustic nonlinearities and their role in material characterization", *Nondestructive Testing and Evaluation*, vol. 7, no 1-6, pp. 273-80, 1992.

[89] L. E. Hargrove and K. Achyuthan, "Use of light diffraction in measuring the parameter of nonlinearity of liquids and the photoelastic constant of solids." in *Physical Acoust.*, vol. 2. Part B, Ed. New York Academic Press: W. P. Mason, 1965, pp. 333-369.

[90] R. A. Guyer and P. A. Johnson, "Hysteresis, energy landscapes and slow dynamics: A survey of the elastic properties of rocks", *J. Materials Processing and Manufacturing Sci.*, vol. 9, no. 1, pp. 14-26, 2001.

[91] F. Van der Meulen and L. Haumesser, "Towards a simple acoustic method to evaluate the nonlinear parameter B/A of fluids", in *2008 IEEE Int. Ultrasonics Symp.*, Piscataway, NJ, USA.

[92] S. Casciaro, C. Demitri, et al., "Experimental investigation and theoretical modelling of the nonlinear acoustical behaviour of a liver tissue and comparison with a tissue mimicking hydrogel", *J. Materials Sci.: Materials in Medicine*, vol. 19, no. 2, pp. 899-906, 2008.

[93] B. Ward, A. C. Baker, et al., "Nonlinear propagation applied to the improvement of resolution in diagnostic medical ultrasound", *J. Acoustical Society of America*, vol. 101, no. 1, pp. 143-154, 1997.

[94] M. J. Hsu, M. Eghtedari, et al., "Characterization of individual ultrasound microbubble dynamics with a light-scattering system", *J. Biomedical Optics*, vol. 16, no. 6, 2011.

[95] L. Germain and J. D. N. Cheeke, "Characterization of nonlinear harmonic generation at the focus of an acoustic microscope", in *IEEE 1987 Ultrasonics Symp. Proc.*, New York, NY, USA.

[96] D. Zhang, J. Chen, et al., "An evaluation method of bonding strength at a bonded solid-solid interface by contact acoustic nonlinearity", in *2005 IEEE Ultrasonics Symp. Proc.*, vol. 1, pp. 285-288.

[97] Y. Zheng, R. G. Maev, et al., "Nonlinear acoustic applications for material characterization: a review", *Canadian J. Physics*, vol. 77, no. 12, pp. 927-967, 1999.

[98] T. Goursolle, T., S. Calle, et al., "A two-dimensional pseudospectral model for time reversal and nonlinear elastic wave spectroscopy", *J. Acoustical Soc. of America*, vol. 122, no. 6, pp. 3220-3229, 2007.

[99] G. Shui, J.-Y. Kim, et al., "A new technique for measuring the acoustic nonlinearity of materials using Rayleigh waves", *NDT&E Int.*, vol. 41, no. 5, pp. 326-329, 2008.

[100] D. C. Price and D. A. Scott, "Theoretical aspects of linear and non-linear wave propagation in rolled aluminum sheets", in *AIP Conf. Proc.*, vol. 657B, pp. 1567-1574, 2003.

[101] S. Hirsekorn and P.P. Delsanto, "On the universality of nonclassical nonlinear phenomena and their classification", *Appl. Physics Lett.*, vol. 84, pp. 1413-1415, 2004.

[102] T. Meurer, J. Qu, et al., "Wave propagation in nonlinear and hysteretic media - a numerical study", *Int. J. Solids and Structures*, vol. 39, no. 39, pp.5585-5614, 2002.

[103] M. Scalerandi, E. Ruffino, et al., "Non-linear techniques for ultrasonic micro-damage diagnostics: a simulation approach", in *AIP Conf. Proc.*, USA, 2000, pp.1393-1399.

[104] K. van den Abeele and M. A. Breazeale, "Theoretical model to describe dispersive nonlinear properties of lead zirconate-titanate ceramics", *J. Acoustical Society of America*, vol. 99, no. 3, pp. 1430-1437, 1996.

[105] A. S. Gliozzi, M. Nobili, et al., "Modelling localized nonlinear damage and analysis of its influence on resonance frequencies", *J. Physics D - Appl. Physics*, vol. 39, no.17, pp. 3895-3903, 2006.

[106] A. A. Shah and Y. Ribakov, "Non-destructive evaluation of concrete in damaged and undamaged states", *Materials & Design*, vol. 30, no. 9, pp. 3504-3511, 2009.

[107] K. Van Den Abeele, P. A. Johnson and A. M. Sutin, "Nonlinear elastic wave spectroscopy (NEWS) techniques to discern material damage, part I: Nonlinear wave modulation spectroscopy (NWMS)", *Research in Nondestructive Evaluation*, vol. 12, no. 1, pp. 17-30, 2000.

[108] K. Van Den Abeele, J. Carmeliet, J. A. TenCate and P. A. Johnson, "Nonlinear Elastic Wave Spectroscopy (NEWS) techniques to discern material damage. Part II: Single Mode Nonlinear Resonant Acoustic Spectroscopy (SIMONRAS)", *Research in Nondestructive Evaluation*, vol. 12, no. 1, pp. 31-42, 2000.

[109] P.P. Delsanto and S. Hirsekorn, "A unified treatment of nonclassical nonlinear effects in the propagation of ultrasound in heterogeneous media", *Ultrasonics*, vol. 42, pp. 1005-1010, 2004.

[110] D. C. Hurley, D. Balzar, et al., "Nonlinear ultrasonic parameter in quenched martensitic steels", *J. Appl. Physics*, vol. 83, no. 9, pp. 4584-4588, 1998.

[111] D. C. Hurley, D. Balzar, et al., "Nonlinear ultrasonic parameter in precipitate-hardened steels", in *Nondestructive Methods for Materials Characterization - Materials Research Soc. Symp. Proc.*, vol. 591, Warrendale, PA, USA, 2000.

[112] V. Rao, E. Kannan, et al., "Observation of two stage dislocation dynamics from nonlinear ultrasonic response during the plastic deformation of AA7175-T7351 aluminum alloy", *Materials Sci. and Engineering*, vol. 512, no. 1-2, pp. 92-99, 2009.

[113] K.-Y. Jhang, "Applications of nonlinear ultrasonics to the NDE of material degradation", *Ultrasonics, Ferroelectrics and Frequency Control*, vol. 47, no. 3, pp. 540-548, 2000.

[114] A. Metya, N. Parida, et al., "Assessment of localized plastic deformation during fatigue in polycrystalline copper by nonlinear ultrasonic", *Metallurgical and Materials Trans. A: Physical Metallurgy and Materials Sci.*, vol. 38 A, no. 12, pp. 3087-3092, 2007.

[115] M. Deng and J. Pei, "Nondestructive evaluation of fatigue damage in solid plates using nonlinear ultrasonic Lamb wave method", *Shengxue Xuebao/Acta Acustica*, vol. 33, no. 4, pp. 360-369, 2008.

[116] T. E. Matikas, A. Paipetis, et al., "Real-time monitoring of damage evolution in aerospace materials using nonlinear acoustics", in *AIP Conf. Proc.*, vol. 1022, pp. 549-552, 2008.

[117] L. Straka, Y. Yagodzinskyy, et al., "Detection of structural damage of aluminum alloy 6082 using elastic wave modulation spectroscopy", *NDT&E Int.*, vol. 41, no. 7, pp. 554-563, 2008.

[118] A. J. Hillis, S. A. Neild, et al., "Global crack detection using bispectral analysis", in *Proc. Roy. Soc. of London, Series A (Math., Physics and Eng. Sci.)*, vol. 462, no. 2069, pp. 1515-1530, 2006.

[119] K. Kawashima, M. Murase, et al., "Backscattered transverse wave imaging of cracked-faces with linear and nonlinear ultrasonics", *Materials Trans.*, vol. 48, no. 6, pp. 1202-1207, 2007.

[120] A. M. Sutin and P. A. Johnson, "Nonlinear elastic wave NDE II. Nonlinear wave modulation spectroscopy and nonlinear time reversed acoustics", in *Proc. AIP Conf. 31st Annu. Review of Progress in Quantitative Nondestructive Evaluation,* Golden, CO, USA, 2005, vol. 760, pp. 385-392.

[121] K. Sheppard, A. Zagrai, et al., "A non-linear acoustic, vibro-modulation technique for the detection and monitoring of contact-type defects, including those associated with corrosion", *Corrosion Reviews*, vol. 25, no. 1-2, pp. 81-96, 2007.

[122] R. Ellwood, T. Stratoudaki, et al., "Investigation of the fatigue process using nonlinear ultrasound", *J. Phys.: Conf. Series*, vol. 278, no. 1, 2011.

[123] J. P. Jiao, B. W. Drinkwater, S. A. Neild and P. D. Wilcox, "Low-frequency vibration modulation of guided waves to image nonlinear scatterers for structural health monitoring", *Smart Materials and Structures*, vol. 18, no. 6, 2009.

[124] P. A. Johnson and A. Sutin, "Nonlinear elastic wave NDE I. Nonlinear resonant ultrasound spectroscopy and slow dynamics diagnostics", in *Proc. AIP Conf. 31st Annu. Review of Progress in Quantitative Nondestructive Evaluation,* Golden, CO, USA, 2005, vol. 760, pp. 377.

[125] G. Zumpano, and M. Meo, "Damage detection in an aircraft foam sandwich panel using nonlinear elastic wave spectroscopy", *Computers and Structures*, vol. 86, no. 3-5, pp. 483-490, 2008.

[126] G. Shkerdin and C. Glorieux, "Nonlinear modulation of Lamb modes by clapping delamination", *J. Acoustical Society of America*, vol. 124, no. 6, pp. 3397-3409, 2008.

[127] S. C. Gustafson, "Ultrasonic transmission through a nonlinear layer in a linear medium", in *1977 Ultrasonics Symp. Proc., IEEE*, New York, NY, USA.

[128] V. L. Weise, C. S. Scruby, E. A. Birt and L. D. Jones, "Report on 'Kissing' Bond and Environmental Degradation Detection using Nonlinear Ultrasonics", QinetiQ, Farnborough, UK, 2002.

[129] J. M. Richardson, "Harmonic generation at an unbonded interface--I. Planar interface between semi-infinite elastic media", *Int. J. Eng. Sci.*, vol. 17, no. 1, pp. 73-85, 1979.

[130] D. J. Barnard, G. E. Dace, et al., "Acoustic harmonic generation at diffusion bonds", *J. Nondestructive Evaluation*, vol. 16, no. 2, pp. 77-89, 1997.

[131] I. Y. Solodov, "Ultrasonics of non-linear contacts: propagation, reflection and NDE-applications", *Ultrasonics (Netherlands)*, vol. 36, pp. 383-390, 1998.

[132] M. Rothenfußer, M. Mayr and J. Baumann, "Acoustic nonlinearities in adhesive joints", *Ultrasonics*, vol. 38, pp. 322-326, 2000.

[133] R. J. Rummel, *Understanding Correlation*, Department of Political Science, University of Hawaii, Honolulu, 1976.

[134] J. Hoffelner, H. Landes, et al., "Finite Element Simulation of Nonlinear Wave Propagation in Thermoviscous Fluids Including Dissipation", *IEEE Trans. Ultrasonics, Ferroelectrics and Frequency Control*, vol. 48, no. 3, pp. 779-786, 2001.

[135] C. Vanhille, C. Conde, et al., "Finite-difference and finite-volume methods for nonlinear standing ultrasonic waves in fluid media", *Ultrasonics*, vol. 42, pp. 315-318, 2004.

[136] M. Hamilton and T. David, "On the coefficient of nonlinearity beta in nonlinear acoustics", *J. Acoustical Society of America*, vol. 83, pp. 74-78, 1987.

[137] D. C. Hurley and C. M. Fortunko, "Determination of the nonlinear ultrasonic parameter ß using a Michelson interferometer", *Measurement Sci. and Technology*, vol. 8, pp. 634–642, 1997.

[138] Z. Hashin, "The elastic moduli of heterogeneous materials", *J. Appl. Mechanics*, vol. 29, no. 3, pp. 143-150, 1962.

[139] R. A. Smith, B. Zeqiri, L. D. Jones and M. Hodnett, "Nonlinear propagation in water and its effect on ultrasonic C-scanning", *Insight – J. British Inst. NDT*, vol. 40, no. 1, pp. 12-19, 1998.

[140] R. F. Anastasi and M. J. Roberts, "Acoustic wave propagation in an adhesive bond model with degrading interfacial layers", U.S. Army Materials Technology Laboratory, Watertown, MA, MTR TR 92-63, September 1992.

[141] P. D. Wilcox, R. S. C. Monkhouse, P. Cawley, M. J. S. Lowe and B. A. Auld, "Development of a computer model for an ultrasonic polymer film transducer system", *NDT&E Int.*, vol. 31, pp. 51-64, 1998.

[142] W. E. Thomson, "Transmission of elastic waves through a stratified medium", *J. Appl. Physics*, vol. 41, pp. 89-93, 1950.

[143] N. A. Haskell, "The dispersion of surface waves in multilayered media", *Bulletin of the Seismological Soc. of America*, vol. 54, pp. 17-35, 1952.

[144] T. M. Pialucha, "The reflection coefficient from interface layers in NDT of adhesive joints", Ph.D. thesis, Dept. Mechanical Engineering, Imperial College of Science, Technology and Medicine, London, 1992.

[145] M. J. Mienczakowski, A. K. Holmes and R. E. Challis, "Modeling of Ultrasonic Wave Propagation in Composite Airframe Components", in *34th Review of Progress in Quantitative Nondestructive Evaluation*, D. O. Thompson and D. E. Chimenti, Eds. Melville, NY: American Institute of Physics, vol. 75, pp. 995-1001, 2007.

[146] G. Sewell, *The Numerical Solution of Ordinary and Partial Differential Equations*, 2nd Edition, John Wiley and Sons Inc., 2005.

[147] S. Liu, S. Best, et al., "Measuring bulk material nonlinearity using harmonic generation", *NDT&E Int.*, vol. 48, pp. 46-53, June 2012.

[148] M. Pasovic, "Second harmonic inversion for ultrasound contrast harmonic imaging", *Physics in Medicine and Biology*, vol. 56, no. 11, pp. 3163-3180, June 2011.

[149] A. N. Kalashnikov and R. E. Challis, "Errors and uncertainties in the measurement of ultrasonic wave attenuation and phase velocity", *IEEE Trans. on Ultrasonics, Ferroelectrics and Frequency Control*, vol. 52, no. 10, pp. 1754-68, 2005.

[150] O. Bou Matar, M. Vila, F. Van der Meulen, L. Haumesser, J. Fortineau et al., "Nonlinear Parameter Measurement for Nondestructive Evaluation of Solids : Calibrated Phase Modulation Method", in *Innovations in Nonlinear Acoustics: ISNA17 - 17th Int. Symp. on Nonlinear Acoust.*, Pennsylvania, USA, 18-22 July 2005, pp. 73-82.

[151] B. W. Drinkwater, R. S. Dwyer-Joyce, et al., "A study of the interaction between ultrasound and a partially contacting solid-solid interface", in *Proc. Roy. Soc. of London, Series A (Math., Physical and Eng. Sci.)*, vol. 452, no. 1955, pp. 2613-2628, 1996.

[152] T. Kundu, A. Maji, et al., "Detection of kissing bonds by Lamb waves", *Ultrasonics*, vol. 35, no. 8, pp. 573-580, 1998.

[153] D. Yan, "The detectability of kissing bonds in adhesive joints using non-linear ultrasonic techniques", Ph.D. thesis, Dept. Mechanical Engineering, University of Bristol, Bristol, UK, July 2010.

[154] S. Yoshifuku, S. Chen, et al., "Parametric harmonic-to-fundamental ratio contrast echocardiography: A novel approach to identification and accurate measurement of left ventricular area under variable levels of ultrasound signal attenuation", *Ultrasonics*, vol. 46, no. 2, pp. 109-118, 2007.

[155] A. J. Croxford, P. D. Wilcox and B. W. Drinkwater, "Non-linear material characterisation using the non-collinear method", *Proc. SPIE – The Int. Soc. for Optical Eng.*, San Diego, CA, USA, 8-11 March 2010, vol. 7649.

[156] C. Jeenjitkaew, "Kissing bonds in adhesive joints: a holistic approach for surface chemistry and joint mechanics", Ph.D. thesis, School of Engineering and Materials Science, Queen Mary, University of London, UK, May 2011.

[157] S. Amami, S. Dos Santos, A. Savin, et al., "Acousto-ultrasonics for non-destructive evaluation of epoxy adhesive joint integrity in complex structures", in *Proc. 10th French Congr. Acoust.*, Lyon, France, 12-16 April 2010.

[158] M. J. E. Golay, "Complementary series", *IRE Trans. Inform. Theory*, vol. IT-7, pp. 82-87, April 1961.

[159] I. Trots, A. Nowicki, W. Secomski and J. Litniewski, "Golay sequences - Side-lobe - Cancelling codes for ultrasonography", *Archives of Acoust.*, vol. 29, no. 1, pp. 87-97, 2004.

[160] Z. X. Ding and P. A. Payne, "New Golay code system for ultrasonic pulse echo measurements", *Measurement Sci. and Technology*, vol. 1, no. 2, pp. 158-165, 1990.

[161] P. Jeong, R. B. Thompson, Y. H. Kim, "Performance evaluation of the Golay code pulse compression technique", *Research in Nondestructive Evaluation*, vol. 8, no. 3, pp. 125-147, 1996.

[162] A. Rivola and P. R. White, "Bispectral analysis of the bilinear oscillator with application to the detection of fatigue cracks", *J. Sound and Vibration*, vol. 216, no. 5, pp. 889-910, 8 Oct 1998.

[163] M. A. Drewry, "Use of chaos in SHM – A literature review", QinetiQ, Farnborough, February 2008.

[164] B. I. Epureanu, "Nonlinear and chaotic vibration-based damage detection", *Proc. American Soc. Mech. Engineers Appl. Mechanics Division*, vol. 254, pp. 163-170, 2003.

Appendices

A One-Dimensional Input Impedance Model

Ultrasonic waves are reflected at boundaries where there is a difference in acoustic impedances of the materials on each side of the boundary. The reflection coefficient, *r*, for a wave travelling from material 2 to material 1 is given by:

$$r = \frac{Z_2 - Z_1}{Z_1 + Z_2} \tag{A-1}$$

where Z_1 and Z_2 are the impedances of material 1 (reflecting medium) and material 2 respectively.

The one-dimensional nonlinear ultrasonic wave equation for damped media was derived in Chapter 4. When considering the linear case where the wave equation is derived from Hooke's Law (4-3), the following linear wave equation is obtained:

$$\rho \frac{\partial^2 u}{\partial t^2} = K_2 \frac{\partial^2 u}{\partial x^2} + \delta \frac{\partial}{\partial t}\left(\frac{\partial^2 u}{\partial x^2}\right) - F_{ext}(x,t) \tag{A-2}$$

where u is the particle displacement, ρ, K_2 and δ are the material's density, bulk modulus and sound attenuation respectively, and F_{ext} is the external applied force.

The harmonic solution to the one-dimensional linear wave equation (A-2) is:

$$u(x,t) = \left(Ae^{ikx} + Be^{-ikx}\right)e^{-i\omega t} \tag{A-3}$$

where A and B are constants, k is the wavenumber, $\omega = 2\pi f_0$ is the circular frequency and f_0 is the fundamental frequency.

With the expression for particle displacement u found in (A-3), the acoustic pressure P and the particle velocity v can be expressed as functions of A and B:

$$P(x,t) = -K_2 \frac{du}{dx} = -ikK_2\left(Ae^{ikx} - Be^{-ikx}\right)e^{-i\omega t} \tag{A-4}$$

$$v(x,t) = \frac{du}{dt} = -i\omega\left(Ae^{ikx} + Be^{-ikx}\right)e^{-i\omega t} \tag{A-5}$$

Equations (A-4) and (A-5) can be expressed in matrix format:

$$\begin{bmatrix} P \\ v \end{bmatrix} = \begin{bmatrix} -ikK_2 e^{-i\omega t}e^{ikx} & ikK_2 e^{-i\omega t}e^{-ikx} \\ -i\omega e^{-i\omega t}e^{ikx} & -i\omega K_2 e^{-i\omega t}e^{-ikx} \end{bmatrix}\begin{bmatrix} A \\ B \end{bmatrix}$$

$$= -i\omega e^{-i\omega t}\begin{bmatrix} \frac{kK_2}{\omega}e^{ikx} & -\frac{kK_2}{\omega}e^{-ikx} \\ e^{ikx} & e^{-ikx} \end{bmatrix}\begin{bmatrix} A \\ B \end{bmatrix} \tag{A-6}$$

But as the wavenumber is $k = \omega/c$ where c is the sound velocity and the bulk modulus is $K_2 = \rho c^2$, we have $\frac{kK_2}{\omega} = \frac{\omega\rho c^2}{c\omega} = \rho c = Z$ the impedance. Hence,

$$\begin{bmatrix} P \\ v \end{bmatrix} = -i\omega e^{-i\omega t}\begin{bmatrix} Ze^{ikx} & -Ze^{-ikx} \\ e^{ikx} & e^{-ikx} \end{bmatrix}\begin{bmatrix} A \\ B \end{bmatrix} \tag{A-7}$$

which is equivalent to

$$\begin{bmatrix} A \\ B \end{bmatrix} = \frac{1}{-i\omega e^{-i\omega t}}\begin{bmatrix} Ze^{ikx} & -Ze^{-ikx} \\ e^{ikx} & e^{-ikx} \end{bmatrix}^{-1}\begin{bmatrix} P \\ v \end{bmatrix}$$

$$= \frac{1}{-i\omega e^{-i\omega t}}\frac{1}{2Z}\begin{bmatrix} e^{-ikx} & Ze^{-ikx} \\ -e^{ikx} & Ze^{ikx} \end{bmatrix}\begin{bmatrix} P \\ v \end{bmatrix} \tag{A-8}$$

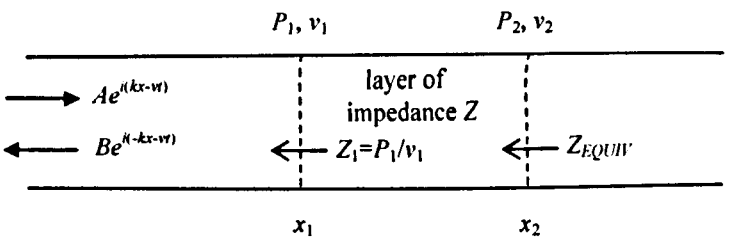

Figure A.1. Model of a multilayer structure

Between positions 1 and 2 in a multilayer structure as sketched in Figure A.1, there is continuity of displacement. Applying equation (A-7) to position 2 and (A-8) to position 1 then combining both to remove A and B, gives:

$$\begin{bmatrix} P_2 \\ v_2 \end{bmatrix} = \frac{1}{2Z}\begin{bmatrix} Ze^{ikx_2} & -Ze^{-ikx_2} \\ e^{ikx_2} & e^{-ikx_2} \end{bmatrix}\begin{bmatrix} e^{-ikx_1} & Ze^{-ikx_1} \\ -e^{ikx_1} & Ze^{ikx_1} \end{bmatrix}\begin{bmatrix} P_1 \\ v_1 \end{bmatrix}$$

$$= \frac{1}{2Z}\begin{bmatrix} Ze^{ikd} + Ze^{-ikd} & Z^2e^{ikd} - Z^2e^{-ikd} \\ e^{ikd} - e^{-ikd} & Ze^{ikd} + Ze^{-ikd} \end{bmatrix}\begin{bmatrix} P_1 \\ v_1 \end{bmatrix}$$

$$= \begin{bmatrix} \cos kd & iZ\sin kd \\ \frac{i}{Z}\sin kd & \cos kd \end{bmatrix}\begin{bmatrix} P_1 \\ v_1 \end{bmatrix} \qquad \text{(A-9)}$$

where d is the distance between positions 1 and 2.

The equivalent impedance looking into the structure from position 1 is given by:

$$Z_{EQUIV} = \frac{P_2}{v_2} = \frac{P_1\cos kd + iZv_1\sin kd}{i\frac{P_1}{Z}\sin kd + v_1\cos kd} \qquad \text{(A-10)}$$

Multiplying the numerator and denominator by $\frac{Z}{v_1\cos kd}$,

$$Z_{EQUIV} = \frac{Z_1 + iZ\tan kd}{Z + iZ_1\tan kd}Z \qquad \text{(A-11)}$$

For a multi-layered media, the impedance is calculated recursively looking into successive layers, working back from the final interface towards the transducer. This leads to the general equations for calculating the input impedance and reflection coefficient that can then be used successively for modelling multi-layered systems.

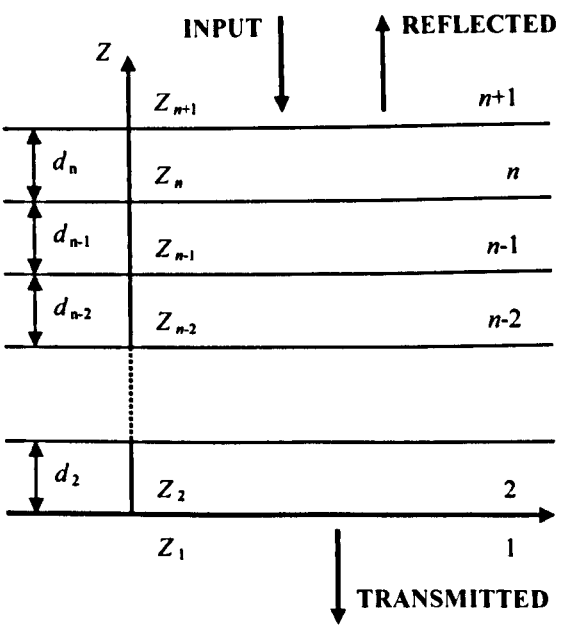

Figure A.2. Multi-layered structure model used for calculation of reflection coefficient

The geometry for plane wave propagation in multi-layered systems is illustrated in Figure A.2 where normal incidence is assumed. Both the top and bottom media are semi-infinite in length with an acoustic plane wave incident on the top boundary. The top medium is numbered $n+1$, the bottom medium is number 1, and there are n-1 intermediate layers numbered 2, 3, 4, ..., n.

Applying equation (A-11) successively, the input impedance for the n^{th} layer is:

$$Z_{in}^{(n)} = \left(\frac{Z_{in}^{(n-1)} + iZ_n \tan \phi_n}{Z_n + iZ_{in}^{(n-1)} \tan \phi_n} \right) Z_n \qquad \text{(A-12)}$$

where for normal incidence $\phi_n = k_n d_n$ and Z_{in} is defined as the impedance of the reflecting medium.

The wavenumber is proportional to the frequency so that:

$$k_n = \frac{\omega}{c_n} \left(1 - \frac{1}{2} \tan \tau \right) \qquad \text{(A-13)}$$

where tan τ is the mechanical loss tangent.

The mechanical loss tangent is a measure of loss-rate of energy of the mechanical oscillation in the attenuative material:

$$\tan \tau = c_n \alpha_n d_n / \pi \qquad \text{(A-14)}$$

where α_n is the attenuation coefficient.

The characteristic acoustic impedance of the material is given by:

$$Z_n = \rho_n c_n \left(1 + i \frac{1}{2} \tan \tau \right) \qquad \text{(A-15)}$$

B Nonlinear ratio and signal amplitudes

As attenuation of ultrasound increases with frequency according to a power law, harmonics experience greater attenuation than the fundamental. A schematic of this process is shown in Figure B.1.

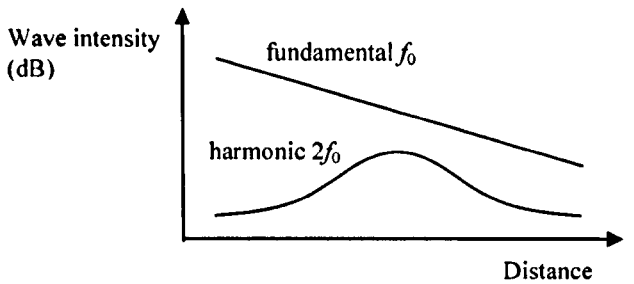

Figure B.1. Schematic of the relative intensity of the fundamental and harmonic components as they propagate through the material

As the signal propagates towards the receiver, it is attenuated. Beam spreading causes a reduction in amplitude inversely proportionate to the distance travelled x, and dissipative attenuation of ultrasound follows the exponential law $\exp[-\alpha(f)x]$ where $\alpha(f)$ is the frequency-dependent attenuation coefficient. However, compared to the harmonic signal amplitude, the nonlinear ratio $\Phi = A_2/A_1^2$ typically utilised in nonlinear ultrasonic analysis has no dependency on both incident ultrasound pressure A_{ap} and attenuation.

In effect, if A_1 is assumed to be proportional to the incident acoustic pressure A_{ap} ($A_1 = a_1 A_{ap}$ where a_1 is a constant), the second order nonlinear response A_2 is proportional to A_{ap}^2 ($A_2 = a_2 A^2_{ap}$ where a_2 is a constant). The combined effect of beam spreading and dissipative attenuation can be approximated by one piece-wise exponential reduction only such that the total attenuation can be written as $\exp\left[-\sum \alpha_i(f)x_i\right]$ where the distances x_i are small enough and the attenuation coefficient constant within each x_i [154]. Therefore, the received signal has a fundamental component of:

$$A_1 = a_1 A_{ap} \exp\left[-\sum \alpha_i(f_0)x_i\right] \tag{B-1}$$

and a harmonic component of:

$$A_2 = a_2 A_{ap}^2 \exp\left[-\sum \alpha_i(2f_0)d_i\right] \tag{B-2}$$

When calculating the nonlinear ratio Φ, the fundamental component is used to normalize the harmonic component in the received signal as follows:

$$\Phi = \frac{A_2}{A_1^2} = \frac{a_2 A_{ap}^2 \exp\left[-\sum \alpha_i (2f_0) d_i\right]}{a_1^2 A_{ap}^2 \exp^2\left[-\sum \alpha_i (f_0) d_i\right]} \tag{B-3}$$

But under the assumption that attenuation coefficients increase linearly with the frequency:

$$\alpha_i(2f_0) = 2\alpha_i(f_0) \tag{B-4}$$

and therefore equation (B-3) becomes:

$$\Phi = \frac{A_2}{A_1^2} = \frac{a_2 A_{ap}^2 \exp^2\left[-\sum \alpha_i (f_0) x_i\right]}{a_1^2 A_{ap}^2 \exp^2\left[-\sum \alpha_i (f_0) x_i\right]} = \frac{a_2}{a_1^2} \tag{B-5}$$

Equation (B-5) shows that there are no distance effects when calculating Φ which is a constant.

The total nonlinear signal characterised by the nonlinear ratio Φ at a distance $x_i = d$ is obtained by integrating the nonlinear contributions from $x_i = 0$ to d and gives an expected linear result.